KAUNAS UNIVERSITY OF TECHNOLOGY

AMER SODAH

DEVELOPMENT AND ANALYSIS OF MICROELECTROMECHANICAL SENSORS FOR HUMAN HEALTH CARE MONITORING

Doctoral Dissertation

Technological Sciences, Mechanical Engineering (T 009)

Kaunas, 2020

The dissertation was prepared at Kaunas University of Technology, Faculty of Mechanical Engineering and Design in 2015–2019.

Scientific supervisor:

Prof. Dr. Habil. Arvydas Palevičius (Kaunas University of Technology, Technological Sciences, Mechanical Engineering – T 009

Editor: dr. Armandas Rumšas (Publishing Office “Technologija”)

KAUNO TECHNOLOGIJOS UNIVERSITETAS

AMER SODAH

MIKROELEKTROMECHANINIO JUTIKLIO ŽMOGAUS SVEIKATINIMO MONITORINGUI KŪRIMAS IR TYRIMAS

Daktaro disertacija
Technologijos mokslai, mechanikos inžinerija (T 009)

2020 Kaunas

Disertacija rengta 2015–2019 metais Kauno technologijos universiteto Mechanikos inžinerijos ir dizaino fakultete.

Mokslinis vadovas:

Prof. habil. dr. Arvydas Palevičius (Kauno technologijos universitetas, technologijos mokslai, mechanikos inžinerija – T009.

Interneto svetainės, kurioje skelbiama disertacija, adresas:
http://ktu.edu

Redagavo: Rozita Znamenskaitė (Leidykla „Technologija“)

Table of Contents

CONVENTIONS AND ABBREVIATIONS

AFM – atomic force microscope
CAD – computer aided design
CGH – computer-generated holography
DFT– discrete Fourier transform
DH – digital holography
DOE– diffractive optical elements
DVD – digital versatile disc
E –Young modulus of material
EBL – electron beam lithography
ESPI – electronic speckle pattern interferometry
F – mechanical force
FBMS – fixed beam moving stage
FE – finite element
FFT – fast Fourier transform
FFT^{-1} – inverse Fourier transformation
FT – Fourier transform
GS – Gerchberg-Saxton
IFTA – iterative Fourier transformation algorithm
KTU – Kaunas University of Technology
LDV – laser Doppler vibrometer
MEMS – micro electromechanical systems
MOEMS – micro opto-electromechanical system
Ni – nickel
ODS – operating deflection shape
P2P – plate-to-plate
PC – polycarbonate
PMMA – poly-methyl methacrylate
Q – electrical force
R2P – roll-to-plate
R2R – roll-to-roll
RDE – relative diffraction efficiency
RIE – reactive ion etching
T – temperature
T_g – glass transition temperature
UAT – ultrasonically-assisted tool
UHE – ultrasonic hot embossing
VAPs – Vibro active pads

INTRODUCTION

The daily life of the contemporary population is nowadays inconceivable without products created by using micro and nano technologies which help solving major issues in medicine, mechatronics, energy production, food industry, ecology and in other areas of industry.

Presently, one of the most challenging tasks of engineering is to improve the sensibility, optical and mechanical properties, as well as the surface morphology of active optical elements (two-dimensional periodic microstructures) used in microsystems, and to adjust them to the most relevant medical studies, biochemistry, food and agriculture industries, to the control of fermentation, and to the research of environmental parameters.

The use (operation) of MOEMS and their functional elements for accumulation and processing of real-time information on the human's health state is one of the most significant and interesting applications. The usage of such microsystems aimed to monitor human health allows avoiding unexpected ailments, and enables to start early stage treatment or illness prophylaxis.
It is known that, currently, there exist (or are under development) some visual cryptographic health monitoring systems which are used to diagnose patient vision systems [Petrauskienė94]. This type of visual cryptographic systems includes complex issues, such as the formation of time-averaged interfering bands. The method of dynamic visual cryptography and its algorithmic realization has been proposed by Aleksa in 2009 [125]. Special coding algorithms are used to insert a secret image into a stochastic moiré cell, however, a computer is not required to decode the information – the secret image is seen when the encoded image is being thrilled (vibrated) by a certain defined pattern. Study (works) in the field of dynamic visual cryptography is closely related to the time-averaged implementation (realization) of optical methods. These implementations are exploited (utilized) while designing the experimental optical moiré devices for the realization of dynamic visual cryptography.

However, in order to ensure higher functionality of such systems, it is necessary to develop a new type of optical elements with microstructures which ensure a higher cryptographic level. One of these optical elements, which can replace a rather simple moiré cell, could be an optical structure generated with the principles of coherent optical digital realization. Such digital realization could be based on the digital holography principles, which would allow to form cells according to the assigned level of complexity. The computer-generated digital hologram is transferred to physical media by using certain technologies, and, after appropriate micro lithographic operations, it can be used as a micro-optic element in visual cryptographic monitoring systems. The cost of the element produced in this way as well as the time consumption is high enough, therefore, it would be appropriate to replicate the generated optical structure into a polymeric material. The currently existing microstructure replication technologies do not provide high diffraction efficiency required for their use in visual cryptographic systems, thus it is important to improve the already existing options and to develop new microstructure replication

and forming technologies which would ensure high reproducibility of the structure of micro-reliefs generated by digital holographic methods throughout the area of the element in use. Therefore, technology that enables such a technological task to be achieved (solved) is the main objective of this thesis.

The aim of the dissertation: To create vibration based thermal imprint technology on a polymer type material for manufacturing functional micro optical elements of sensors applied in visual cryptographic human health monitoring systems

The objectives of the dissertation:

1. To perform scientific literature review on the thermal imprint technology of micro periodical structures and their usage in sensors for human health monitoring;
2. To investigate the influence of forced high frequency vibration acting in the normal direction to the imprinted surface on the distribution of plastic deformations on the surface of a thermal imprinted polymer;
3. To design and investigate a sonotrode and to apply it in vibration based thermal imprint technology on a polymer for the manufacturing of optical microstructures in the scale useable for coherent optics;
4. To design and investigate an active-thermal sonotrode for vibration based thermal formation technology of polymer microstructures used in the coherent optics technologies;
5. To manufacture a functional element of sensors applied in a visual cryptographic human health monitoring system.

Research methods

GSolver program package was used for the modeling (simulation) of periodic microstructures, and an atomic force microscope *NANOTOP-206* and a laser diffractometer were used to analyze the quality of the structures.

To test the dynamic properties of the designed sonotrode, a Polytec laser doppler vibrometer was used; it performed the function of the vibration source. Finite element analysis was done by using the *Comsol Multiphysics* package while modeling the designed sonotrode.

Computer-generated holograms used in a visual cryptographic device were generated by using the *Matlab* package, while the physical holograms were produced by using the *Raith e-LiNEplus* electron beam lithographic system.

For the replication of microstructures, a designed thermal imprint device (equipment) was used.

Defended statements

1. Using a vibration based thermal imprint device acting in the normal direction of the formed surface, the polymer plastic deformation field is concentrated on its surface.
2. Vibration based thermal imprint technology using high-frequency oscillations in the normal direction of the composed surface forms polymer microstructures with continuous and high diffraction efficiency throughout its imprint area.

Scientific novelty

1. A mathematical model of polymer behavior during the thermal imprint has been created; it enables us to study the influence of vibration and temperature on the concentration of polymer surface deformations.
2. A mathematical model of a vibration based thermal imprint device – sonotrode – has been created; it enables us to estimate the influence of multifunctional parameters so that to ensure the functionality of this device.
3. Experimental research methods and stands have been developed in order to assess the quality of microstructures thus ensuring the use of the principles of coherent optics in the optical elements being developed.
4. Technological parameters of the thermal imprint process have been determined to ensure a high-quality microstructure replication process in the whole replicated area.
5. A technology has been developed which incorporates synergies of digital holography and visual cryptographic techniques in the use of visual cryptographic human health monitoring systems for optical elements.

Practical significance

The practical significance of this dissertation relates to the vibration based thermal imprint device developed in this work that can be used in standard tension-compression machines, and the area formed under its pressure as well as the relief can be modified by identifying the preliminary imprint characteristics.

Vibration based thermal imprint technology can be used to form not only single optical elements, but also to replicate micro periodic structures, and, due to mass production, to reduce the cost of such optical elements.

The created optical elements based on digital holographic and visual cryptographic principles can be used not only in the health monitoring systems, but also in other cryptographic systems where a high level of data coding security is of top importance.

Scope and structure of the dissertation

The dissertation contains the introduction, 4 chapters, general conclusions, a list of literature including 134 references, and the list of the scientific publications of the author of the thesis. The dissertation is composed of 107 pages, 77 figures (92 figures including Appendix), and 12 tables.

The introduction presents the problem of the dissertation, as well as the aim and objectives of the work; moreover, the scientific novelty, the defended statements and the practical significance of the dissertation are presented.

The first chapter introduces products with micro and nano structure as well as the technology for the development of micro and nano technology. Furthermore, methods for the investigation of the periodic microstructure and the simulation of the replication process have been described. Finally, the application of polymeric micro sensors and actuators in biomedical systems and visual cryptography systems has been outlined.

The second chapter presents microstructure replication by vibrational thermal imprint which was modeled and simulated by using *COMSOL Multiphysics* software in order to reveal better specific properties of the replication process and enable the improvement of the process. Results of the research showed that application of vibration excitation during this process ensures a greater imprint depth in comparison with the samples imprinted at conventional conditions.

The third chapter describes a quality evaluation method of the printed microstructure on the polycarbonate material with various conditions of the experiments and evaluates it by using diffraction efficiency and an optical microscope. Also, the results are compared with and without applying vibratory excitation. Besides, this chapter explains the experimental setup for the mechanical hot imprinting technology with the newly designed sonotrode, the thermal temperature distribution for the front mass, the bump test, and impedance analysis. In addition, the chapter contains numerical simulation of the prestressed sonotrode device in order to define the uniform displacement field throughout the entire operating surface as well as at various points.

In the fourth chapter, the concept of a novel cantilever-type microsystem platform in the field of biomechanics using the optical technique of image encryption and communication scheme based on computer generated holography is presented. An image hiding technique based on computer generated holography and dynamic visual cryptography is employed.

Approbation of the dissertation results

The doctoral research was performed in the laboratories of:

- Institute of Materials Science;
- Institute of Mechatronics;
- Department of Mechanical Engineering.

The results of the dissertation have been obtained in accordance with the project of scientific groups: LMT (Lithuanian National Foundation project) Project "Research and development of innovative functional nano/micro components for micro hydraulic devices in biomedicine" Nr. S-MIP-17-102 (2017–2020).

Dissertation-related topics were presented at 4 scientific conferences:

International conference on advanced technology & sciences: 4th international conference, ICAT'Rome, Rome, Italy, November 23–25, 2016:

Nanostructured materials for the detection of CBRN: [proceedings of the NATO advanced research workshop on nanostructured materials for the detection of CBRN, Kiev, Ukraine, 14–17 August 2017] / edited by J. Bonča and S. Kruchinin. Dordrecht: Springer, 2018. pt. F1, ch. 17, p. 223–232.

Mechanika 2018: proceedings of the 23rd international scientific conference, 18 May 2018,

XV international conference on the perspective technologies and methods in MEMS design (MEMSTECH), Polyana, May 22–26, 2019: proceedings. Piscataway, NJ: IEEE, 2019. p. 28–31.

7 scientific publications related to the problems raised in the doctoral dissertation have been delivered in scientific journals: 3 publications in the ISI *Web of Science* database with impact factor and 4 publications in other international database journals.

1. LITERATURE REVIEW

This chapter introduces the products with the micro and nano structure as well as the technology for the development of micro and nano technology. Furthermore, methods for investigation of the periodic microstructure and simulation of the replication process are described. Finally, the application of the polymeric micro sensor and actuators in biomedical systems and the visual cryptography system are introduced. The aim of this study is to reveal their advantages and disadvantages thus facilitating the selection of the most appropriate process flow.

With the development of advanced technologies, the demand for new microelectromechanical (MEMS) and micro-opto-electromechanical (MOEMS) systems, their structural (integrated) elements and new materials with exceptional features is rapidly increasing. The use of MOEMS sensors for the collection (accumulation) and processing of real-time information about the state of a human's health is one of the most significant and interesting applications. The use of such microsystems to monitor human health allows avoiding unexpected ailments and enables to start early stage treatment or illness prophylaxis. One of the most important elements of the MOEMS sensors is the micro periodic structure, the length of the period which correlates with the wavelength of the laser; therefore, it is possible to apply the principles of coherent optics for diagnostics. The qualitative replication of such micro periodic structures is an important task whose solution requires the development of specific technologies and methods in order to obtain high-quality replicas. Recent studies have focused on the development of new, biocompatible nanocomposite materials and their application in various MEMS sensors and actuators. Currently, one of the most challenging tasks in engineering is the improvement of the sensibility, optical and mechanical properties, and surface morphology of active optical elements (two-dimensional periodic microstructures) used in microsystems, and their adaptation to the most relevant medical research, biochemistry, food and agriculture industries, control of fermentation, and environmental parameters.

1.1. Introduction to microstructure and nano structure

Manufacturing of forms for high-volume creation of parts with smaller scale and nanoscale highlights are vital in the worldwide research and industry endeavors to meet the expanding requirements for gadget scaling down in various areas of application.

Procedures for the replication of surface geometries are promising innovations that are capable of adequately satisfying the need for assembling items requiring little-to-no effort and a high volume of production. Among these advancements, hot embellishing is a procedure which depends on raising the temperature of a sheet of polymer up to its dissolving range and on squeezing a warmed ace plate into the polymer for setting off a nearby progression of the material to fill the cavities to be recreated. This procedure has been extensively considered recently specifically because of the generally straightforward set-up and ease related with its application in contrast with other replication systems.

A few products with a fine surface structure on the micrometre-to-nanometre scale have been created; their use in numerous fields is highly predictable. In the medicinal field, regenerative restorative methods have been proposed with the objective of using tissue platforms with a fine nanostructure [1, 2]. Physiological sensors using surface plasmons have been delivered [3]. Also, in the semiconductor and electronics segment fabricating fields, manufacturing of transistors, memory items, and sensors using miniaturization and carbon nanotubes as wiring for CPUs has been progressing [4]. Newly designed media for high-thickness memory for information stockpiling are additionally being considered [5]. Moreover, nanostructure on the outside of a movie with cutting edge highlights of an electrolyte film has been created for use in the field of vital importance of polymer electrolyte power modules (PEFCs) and direct-methanol energy components (DMFCs) [6, 7]. These products not merely feature microscale and nanoscale surface structures, they likewise offer extra esteem and execution.

Subsequently, products with microstructure or nanostructure are systematically sought for after scaling down and implementing useful improvement(s) of the fine structure. In order to accomplish scaling down, top-down development strategies are essential, which produce the ideal shape by using a handling machine with a form stamper. Likewise, progressively imperative systems are base-up systems using materials' own self-association [8, 9].

1.2. Methods of making micro-nano technology and thermal imprinting

By a long shot, the driving innovation for assembling MEMS devices is Si-micromachining with its different subsidiaries. In any case, numerous utilizations of microsystems have prerequisites on the type of materials, geometry, angle proportion, measurements, shape, precision of microstructures, and the number of parts that cannot be obtained effectively by standard silicon-based micromachining innovations. LIGA, an elective microfabrication process joining profound X-ray lithography, plating-through-mask, and molding, empowers specifically the exact production of high-perspective proportion microstructures with extensive basic stature extending from hundreds to thousands of micrometres of thickness. These tall microstructures can be created in an assortment of materials with thoroughly characterized geometry and measurements, exceptionally straight and smooth sidewalls, and tight resilience. LIGA innovation is likewise appropriate for mass manufacturing of parts, especially of polymer parts. Many microsystems draw advantage from novel attributes and points of interest of the LIGA procedure regarding the product manufacturing. LIGA innovations are thus promptly surveyed. The qualities of the assembling strategy and its principal fields of utilization are stressed with models taken from different groups around the world, particularly in micromechanics and micro optics [10].

Nanoimprint lithography (NIL) technologies have excited incredible interest in both scholarly community and industry because of their high definition, low costs, and high-volume Nano patterning capacity. What is more, as an epoxy tar-based negative enhanced photoresist, SU-8 is a perfect possibility for NIL on account of its low-glass-change temperature, low-volume shrinkage coefficient, and great optical properties. In this context, we highlight significant specialized accomplishments in

NIL on epoxy resin and its applications for bio- and nano-photonic structures. NIL was likewise related with the duplication of imprint templates, initially manufactured by e-beam lithography (EBL) trailed by responsive iron etch (RIE), by using the SU-8/SiO2/PMMA tri-layer method. Also, nanoimprint properties were methodically explored for the sake of optimization. The acquired nanoimprint process for various applications offers promising possibilities in the cutting-edge lithography resolution [11].

For example, the creation of a moment statue was accounted for when using a UV curing material [12]. The key strategy was the utilization of the multiphoton ingestion procedure of a femtosecond laser. Recently, the scaling-down of machining instruments has been progressing, and the small-scale end of several micrometers in width is already being offered. In order to accomplish very precise microfabrication by machining, complete framework improvement including machine tools and their driving device turn out to be essential. Attributable to the size impediment of apparatuses, the base size of the current level is believed to be around a few micrometers. It appears that the progress of the tooling devices results in our ability to handle progressively more and more complex shapes.

Despite the fact that the systems depicted above have benefits as well as negative marks, they are generally actually present in real life. In any case, the possibility of a procedure that produces an object straightforwardly and independently is wasteful as a system for large scale manufacturing. In this way, the procedure of a mother design made by the systems clarified above is basic for the large scale manufacturing of items with small scale and nanostructure. In such conditions, infusion molding and nanoprint/engrave strategies are considered as a replication procedure and are viewed as promising systems appropriate for large scale manufacturing.

Diverse designing procedures have emerged, and some of them have turned out to be built up with the expanding enthusiasm for the properties related to complex organized surfaces made of low-cost polymeric materials. This advancement has required parallel improvement of novel advances and materials which are required for every technique. This trend has opened the door for designing surfaces with highlights with sidelong measurements crossing over the nano-to millimetres. One methodology for creating a complex miniaturized scale and nanopatterns on polymeric surfaces is the propelled photolithography which is employed to exchange an example onto a substrate by methods for an etching procedure. In creating a staggered structure from single opposed layers, various novel methodologies have been developed. They depend on extraordinary veils and projection optics which permit tweaked presentation portions of the opposing film. Another procedure utilizes proximity lithography to present diffraction designs from a regular chrome-on-glass cover by leaving a controlled air hole between the opposing film and the mask [13]. Ordinary technologies, for example, injection molding, injection compression molding, and hot embossing have been broadly utilized at small-scale replication. Hot emblazoning is presently turning into a promising assembling process which is appropriate for

creating dedicated microstructures with high angle proportions and less distortion [14, 15].

Hot embossing [16] is an assembling strategy utilized for a wide number of uses from macro to nanometer scales. Hot embossing is a method of imprinting microstructures on a substrate by using a master mold. It, for the most part, comprises the accompanying advances. To start with, the polymer is warmed above its glass progress temperature (T_g). Furthermore, the polymer is stepped with the ideal imprinting at this temperature (above T_g), where it acts progressively as a liquid. Additionally, the power required to misshape the polymer at this temperature is slightly higher than that required at temperatures below the glass change (T_g) of the polymer. Thirdly, the polymer is cooled below its T_g, and the mold is expelled [17].

Hot embossing can be a cyclic and nonstop procedure [18]. Li, Liu and Peng [19] explored the preparation of smaller scale parts by hot embossing. The obtained outcome was that the replication exactness firmly relied upon the handling conditions: on the preparation temperature and the applied force.

The basic strategy is to break down diverse parameters related with the last quality control of the replicas received by hot embossing. Most recent works describe the impact of polymer materials (viscosity, forming temperature and so on) as they rely upon the form and the related parameters (material, geometry, physical and thermomechanical properties, surface states and temperature) and on the parameters defining the hot embossing process (temperature and time for heating, holding and cooling time, applied force, demolding temperature, and so on) which are the critical parameters [20, 21].

In the hot embossing step, non-uniform force appropriation may result in height differences in the pattern. The distinctive thermal extension coefficient may show up an expansive thermal stress. Consequently, it is conceivable that cracks in polymers at a smaller scale structure may develop during the cooling step. The grip between the polymer and shape in the demolding step may impact final pattern abandons [22].

At the point when the imprinting force is not sufficiently high, any longer holding time is expected to offer complete filling of the pattern, which will result in long process durations and in low efficiency of embossing. Even though a high force can improve the embossing efficiency, an excessively high force can harm the friable mold as silicon. The usefulness of micro-structures with uncommon use might be influenced; the material that is used for photoelectric detectors, for instance, will be damaged when the pressure surpasses 6 MPa [23].

For thermal plastic materials, the mechanical behavior is generally impacted by the temperature. At the point when the temperature is excessively low, the polymer will need flowability, which will result in a high level of recuperation and expansive bends in the wake of demolding. At the point when the embossing temperature is excessively high, the polymer atom can be broken, and numerous deformities are created in the embossing area. Hu [99] outlined that there were numerous increases in the PMMA substrate after decorating when the embossing temperature had achieved 280 ºC. Then, again, in order to stay away from noteworthy material out arrangement

at the kick the die-to-die the dust interface, steady deformation of the polymer at moderately low temperatures is needed [24].

Chang *et al*. [25] connected a gas weight amid the contact between the mold and the polymer substrate in the hot embossing process. Along these lines, the looks into accomplished a uniform force at the outside of the polymer and improved the nature of the parts.

Lin, Chen and Hung [26] considered the force conveyance consequences for the polymer surfaces during the cooling stage in the hot embossing process. The outcome showed that a higher embossing force resulted in a progressively uniform shrinkage of the polymer related to the elastic deformation during the cooling stage.

Becker and Heim [27] highlighted that the hot embossing procedure could empower microstructure replication with high perspective proportion (tallness/segment) over huge thermoplastic polymer zones.

Bogdanski *et al*. [28] showed the capacity to effectively create replicas in flimsy layers with poly(methylmethacrylate) by hot embossing while using a delicate form in polydimethylsiloxane (PDMS) introducing concentric V grooves conveyed on an expansive surface.

Carvalho *et al*. [29] showed that the quality and roughness of the mold assumes a noteworthy job amid the hot embossing process so as to get imitations with the required quality.

Datta and Goettert [31] devised a number of steps to determine the optimum hot embossing process conditions without the use of any material model. The method was capable of determining optimum hot embossing conditions for PMMA, PC and polypropylene (PP). The most significant process parameters were found to be the molding temperature, the molding force, the molding rate, the hold time, the demolding temperature, and the demolding rate. The ideal power and temperature amid embellishment brought about total filling of form, thus creating excellent parts and longer shape embed lifetime.

Yao *et al*. [32] came up with a new scheme to make the hot embossing process faster: instead of heating and cooling the same stamp, they used two different stages.

Various researches sought to decrease the process duration for the hot embossing process by utilizing different heating strategies: direct liquid heating [33], introduction heating [34], laser heating [35], infrared (IR), ultrasonic and gas heating [36].

With a metallic mold, there is a likewise probability of harm to the formed pattern brought about by the frictional force between the mold of the molded form and the shaped example that becomes, possibly, the most important factor in the demolding procedure [37].

Most problems occur during the imprinting process; they are highlighted by the authors as follows:

- Microstructure filling ratio [38];
- Non-similar mold imprinting [39];
- Adhesion between the mold and the polymer [40];
- Roughness of the surface [41];

- Long cycle time [42].

In any case, merely the improvement of hot imprinting process parameters is not sufficient. It is necessary to consider the specific mechanical equipment, materials, etc. This requires new techniques and goes along with the progress towards accomplishing better quality replicas. These issues can be dealt with by using high frequency vibrations [37, 39].

High frequency vibrations are generally utilized in various applications and innovations. Capillary waves were utilized for bead development on a vibrating surface in [43]. Surface acoustic waves were employed to concentrate bio-particle suspensions [44], to control the temperature of fluid beads [45], to create single heartbeats and breaks [46], to deliver standard, long-run, spatially requested polymer designs without requiring the utilization of physical or concoction templating [47]. Ultrasonic engines were used to drive liquids [48], to operate in heart pressure devices, or to control electro-rheological liquids [49].

Miniaturized scale designing of polymers by ultrasound was first featured for dissolution and embellishment of powders [51, 52]. The improvement of miniaturized scale designing of polymer plates began with [37], and, in 2008, distribution on a smaller scale framework created by ultrasonic hot embossing was achieved.

In industry, ultrasonic vibration [54, 55] has been generally employed in the welding and joining of thermoplastics when a low temperature is required for softening. The instruments required for ultrasonic vibration hot embossing can incorporate an installation for holding the parts, a vibration horn, an electromechanical transducer to drive the horn, a high frequency control supply, and a cycle clock. In the course of ultrasonic vibration, high frequency (commonly, 10 to 40 kHz) low abundancy (regularly 1 to 25 μm) mechanical vibrations are connected to the parts. This outcome in patterned disfigurement of the parts and of any surface roughness. Ultrasonic energy is converted into heat through intermolecular grating inside thermoplastics. The created heat, which is the highest at the surface between the ace form and the plate because of ill tempers, is adequately high to soften thermoplastics and make it liquefy so that its stream fills the interface. Ultrasonic vibration heating may offer a successful method for heat generation to hot emboss the exact structure onto the outside of an expansive plate [37].

Liu and Dung [37] utilized ultrasonic vibration as a heat generator for hot embossing. They researched the replication limit of ultrasonic-heating embossing of both shapeless and semi-crystalline plastic plates; they also analyzed the impacts of various ultrasonic vibration parameters on the form of the reproduced structure; they distinguished the overall noteworthiness of every one of these parameters on the quality of the formed part. The test results demonstrated that ultrasonic vibrated hot embossing could serve as a powerful method for trimming of exact structures onto polymeric plates with great replicability. Shapeless materials displayed preferable replicability over semi-crystalline materials in ultrasonic vibrated embossed plates. The replicability of decorated plates diminished with the plate thickness. One can improve the replicability of an ultrasonic vibration hot embossing plate by: expanding the initial force, plentifulness of the vibration time and vibration intensity, and the

hold weight as well as hold time. What is more, the replicability of embossed plates increases with the energy input. In any case, if the energy input is excessively high, the replicability diminishes basically due to the overmelting of the plate.

Mekaharu *et al*. [39] managed exact replication of examples by inspiring ultrasonic vibration other than heat and the stacking power on micro scale hot embossing (MHE). They utilized a Ni electroformed form with miniaturized scale designs with seven sizes of passageways from 100 μm^2 to 1.2 mm^2. The trial was conducted on a polycarbonate (PC) sheet with longitudinal rush of ultrasonic vibration at greatest sufficiency of 1.8 μm. The impact of bubble deformity in the example was lessened or totally vanished was reduced by awing ultrasonic vibration. Besides, it was determined that ultrasonic vibration helped relaxed PC to move to the focal point of the specimen region in the form. The authors found that the impact of ultrasonic vibration was thoroughly articulated at a low contact level. It is likely that extremely high contact power might discourage the movement of ultrasonic vibration.

VAPs (Vibro active pads) are developed and fabricated for the thermal imprint process; they operate on the basis of inverse piezoelectric effect, i.e., converting AC voltage to harmonic mechanical displacements. The purpose of a VAP is to stimulate the flow of a pre-heated polymer towards the master microstructure and enhance replicability.

The objective of the VAPs device is to generate uniform vibratory displacements at every point of the top operating surface (Fig. 1.1). The ODS ensures uniform beneficial influence of the high-frequency vibratory excitation throughout the entire surface of the replicated microstructure.

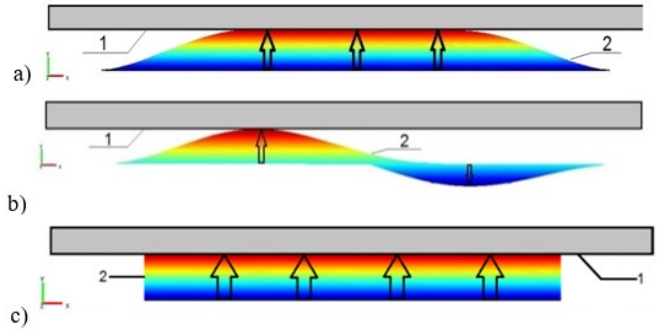

Fig.1. 1 Contact patterns between the VAP (2) and the polymer (1): the first ODS of the membrane (a), the second ODS of the membrane (b) and the ODS when the operating surface is in full contact with the polymer (c) [53]

A simplest test demonstrates that the nature of a replica is very low after hot imprinting. The question is whether high recurrence excitation of the polymer surface amid the procedure of hot imprinting could fill the holes between the mold and the polymer. A piezoelectric component *PZT-4* was selected as a source of high recurrence vibrations. The measurements of the component were the following: 50 mm outside distance across the ring; 20 mm inward breadth, and 3 mm thickness. The piezoelectric exciter was mounted under the platform which holds the polymer so as

to take out conceivable alternate routes or splits brought about by the pressure. The schematic outline of the hot imprinting test setup with the piezoelectric component which is mounted under the plate holding the glass covered by the polymer is shown in Fig.1.2.

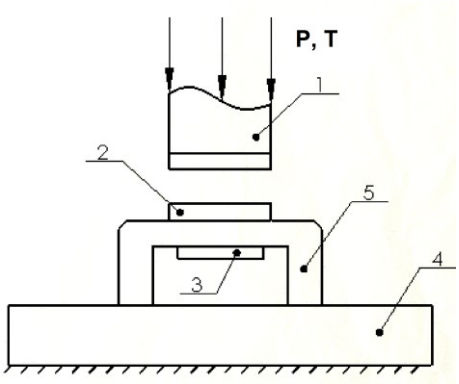

Fig.1. 2 Schematic diagram of the thermal imprint experimental setup with high frequency excitation: 1 – the coin; 2 – glass coated by the polymer; 3 – the piezoelectric element; 4 – the base; 5 – the vibrating platform [131]

Narijauskaitė (2013) used an aluminum disc type vibroactive pad, and the relative diffraction efficiency achieved when using this platform with a PZT-5 ring as a vibroactive material was 11.25% and 17.89% without and with vibratory excitation, respectively. The frequency was 8.5 kHz, and the temperature of thermal imprinting was 160 ºC [131].

The images of both prototypes are provided in Fig. 1.3. The application of several piezoceramic rings resulted in the multilayer effect, i.e., the superposition of layers caused higher amplitudes. The higher amplitude and force increased the velocity of the pre-heated polymer flow, which led to increased replicability.

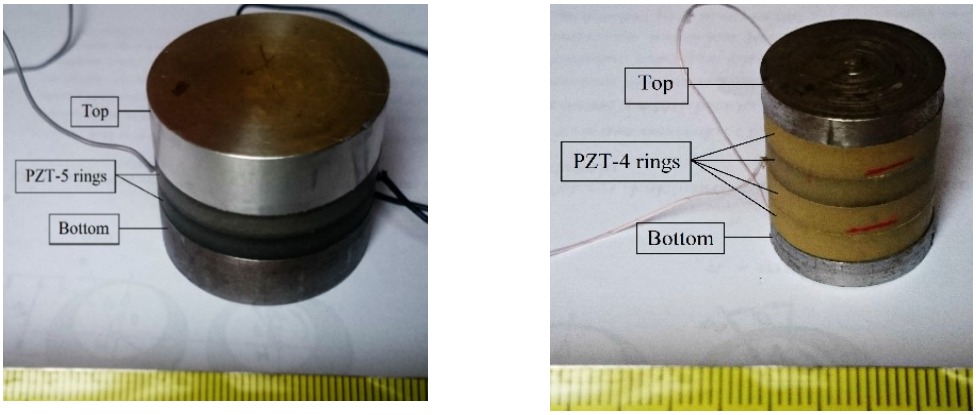

a) b)

Fig.1. 3 Prototypes of VAPs: VAP-1 (a) and VAP-2 (b) [53]

The Prototypes of the vibro active pad presented in Fig 1.3 were used by Šakalys (2014) for the thermal replication process on the polycarbonate material. The range of pressure was 100 to 500 kPa, the temperature was 152 ºC and 148 ºC, and the duration of imprinting was 10 sec. Vibratory excitation of 8.46 kHz was applied. The average achieved diffraction efficiency was 12.2% (with an imprint temperature of 148 °C) and 18.3% (with an imprint temperature of 152 °C) [53].

1.3. Review for simulation of replication process

Past investigations showed that the utilization of vibratory excitation as an advantageous strategy resulted in the decreased procedure length and imprint pressure. In addition, vibrations invigorated the progression of the melted polymer towards the main microstructure [56, 57, 58] thus allowing to improve the replicability. What is more, vibratory excitation is useful for the withdrawal of the main microstructure as it decreases the contact stresses thus reducing the likelihood of microstructure damage [59, 60].

Hot imprinting without help of vibratory excitation and vibratory equipment had already been independently displayed when intending to determine the polymer conduct throughout the procedure and set up the working parameters of actuators which were connected during the hot imprinting process [61, 62].

The numerical model of the procedure of mechanical hot imprinting into polycarbonate close to its glass progress temperature is displayed in this part. The trial results were contrasted with hot imprinting recreations in order to research the adequacy of the new model. These re-enactments were supplied with information which is valuable for contrasting against the test results in order to better comprehend the mechanical hot imprinting process. The modeling and simulation methodology by FEM including geometrical demonstrating, boundary conditions, meshing, material properties, process conditions and administering conditions are presented. In this modeling, Comsol Multiphysics was used. The hot imprinting model development chart is shown in Fig. 1.4.

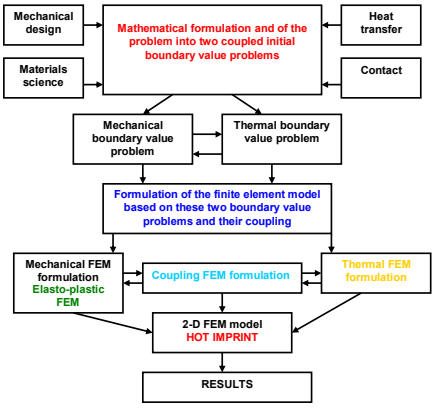

Fig.1. 4 Hot imprint mathematical model diagram [61]

The analyzed dependence between the temperature and pressure versus time is modified for this model as shown in Fig.1.5.

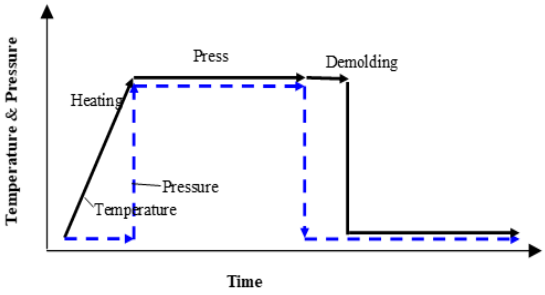

Fig.1. 5 Diagram of mechanical hot imprint process [61]

For this situation, the displayed model is comprised of three stages: heating, imprinting and demolding. A graph of mechanical hot imprinting is displayed in Fig. 1.6.

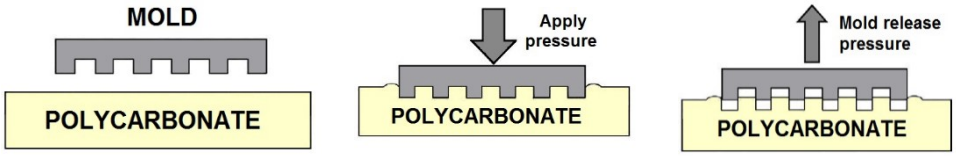

a) Heating step b) Hot imprint step c) Demolding step

Fig.1. 6 Steps of mechanical hot imprint process of periodical microstructure: on the left – the heating step; in the middle – the hot imprint step; on the right – the demolding step [62]

The elasto-plastic material model was selected. This model is simplified by assuming that polycarbonate can be cooled in a very short period of time, thus a separate cooling step is not analyzed.

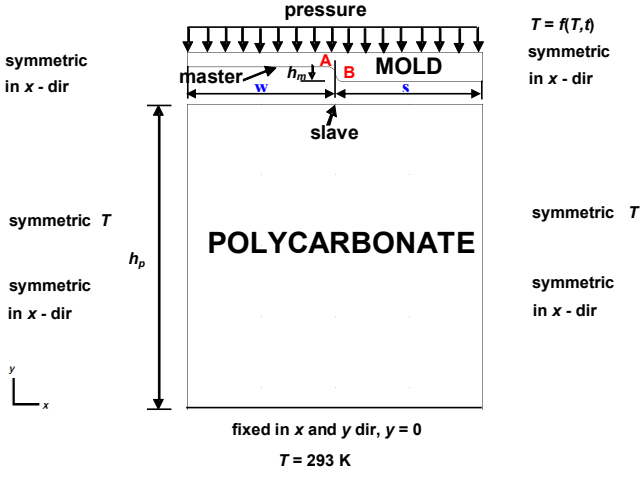

Fig.1. 7 Boundary conditions of the hot imprint process [62]

The total reproduction requires two diagnostic models: thermal examination when using the heat exchange model, and mechanical investigation when using model of basic mechanics together with the relevant information and solution. The boundary conditions and the initial qualities in Comsol Multiphysics programming are portrayed in three dimensions: sub-areas, edges, and points. Fig. 1.7 shows a two-dimensional (2-D) FEM model of Nickel mold, Polycarbonate substrate and boundary conditions.

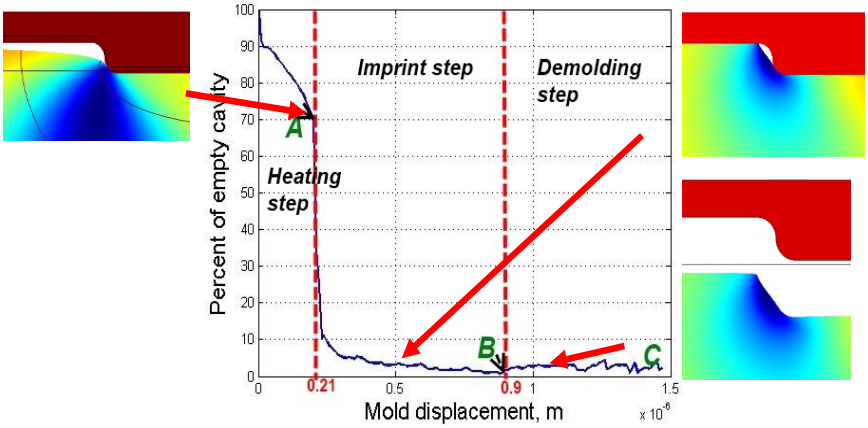

Fig.1. 8 The dependence of non-filling cavity on mold displacement [62]

As shown in Fig. 1.8, polycarbonate void hole diminishes gradually at the end of the heating advances (the mold moves to 2e-7 m) to 70%; at that point, the empty cavity quickly decreases (when the shape moves to 2.3e-7m) to 10%. Towards the finish of the embossing step, the empty cavity is decreased till 2%, yet, during the demolding step, the vacant cavity got marginally increased and reached about 4%.

However, a finite element model and exploratory confirmation of thermal imprinting helped by vibratory excitation is fundamental if we want to provide any significant observation about the changed procedure. The number of parameters and properties must be assessed in numerical models dependent on the finite element technique. Polymers are classified into three states: glass, semi-liquid, and stream in terms of the temperature; subsequently, the material model must correspond to the temperature. In the non-direct viscoelastic material model, such parameters as Young's modulus, thermo-conductivity coefficient, and consistency are administered by the temperature, pressure and procedure time. Commonly, material properties are obscure as for the specific procedure temperature; in this manner, the material properties are resolved tentatively, or, else, data is determined the other way around [63]. Tentatively acquired polycarbonate stress unwinding bends developed at 150 °C and at various prompt strains are connected in the estimation of model parameters [64].

The numerical simulation of thermal imprinting helped by vibratory excitation is fundamental to expand the breaking points of the procedure, to determine the ideal procedure conditions and to recreate microstructures with high accuracy and

precision. Several authors have applied elastoplastic, while other scientists have employed the viscoelastic material model [61, 65].

1.4. Techniques for investigation of periodical microstructure

It is of critical importance to comprehend the impact of the cross-section profile on the phase and spectral surface qualities by various strategies for shaping micro relief structures as it legitimately relies upon the properties of the optical diffraction framework [66–68]. In order to enhance the mechanical procedures of diffractive cells, solid, employable and informative control strategies are required. The techniques for periodic microstructure research can be divided into immediate and roundabout techniques. The scanning electron microscope (SEM) [69, 70], the atomic force microscope (AJM) [71, 72], optical magnifying instruments and other devices can legitimately determine intermittent microstructure parameters. When using diffractive and interfering measurement strategies, it is conceivable that we can research the optical properties of the diffractive grating, and, in a roundabout way, determine the geometrical parameters of the structure alleviation [73, 74].

Scanning electron microscopy and atomic force microscopy strategies can be used to measure the relief parameters (the depth and the period) of the relief wavelength [76–70]. These measuring tools allow to promptly obtain informative, clear and well-visualized results. However, such research equipment is relatively expensive. Also, due to the limited size of the object under investigation and the special geometric profile parameters, it is not always possible to inspect the specimen without breaking it. This is especially relevant for uninterrupted process control when the object under investigation continues to be used in production after measurements.

The optical parameters of the diffractive grating are evaluated by relative or absolute diffraction efficiency. The relative diffraction efficiency (SE) is expressed as the ratio of the intensity of the diffraction and reflected on the surface without micro relief flows. The absolute diffraction efficiency (DE) is expressed as the ratio of the diffraction and the falling flow intensities. Therefore, measurements of diffraction efficiency and diffraction maxima in space (Figure 1.9) are used to describe the studied objects in as much detail as possible.

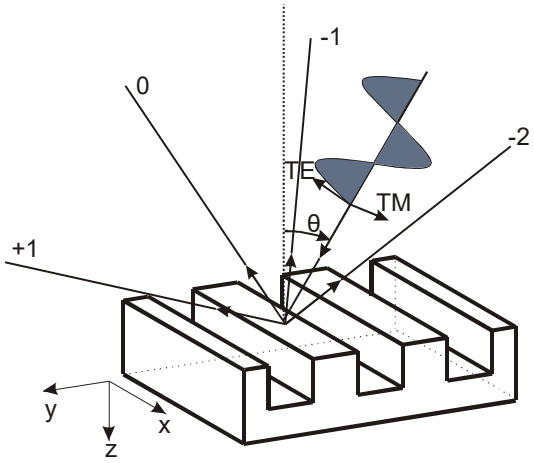

Fig.1. 9 Distribution of linear periodic microstructure diffraction peaks [76]

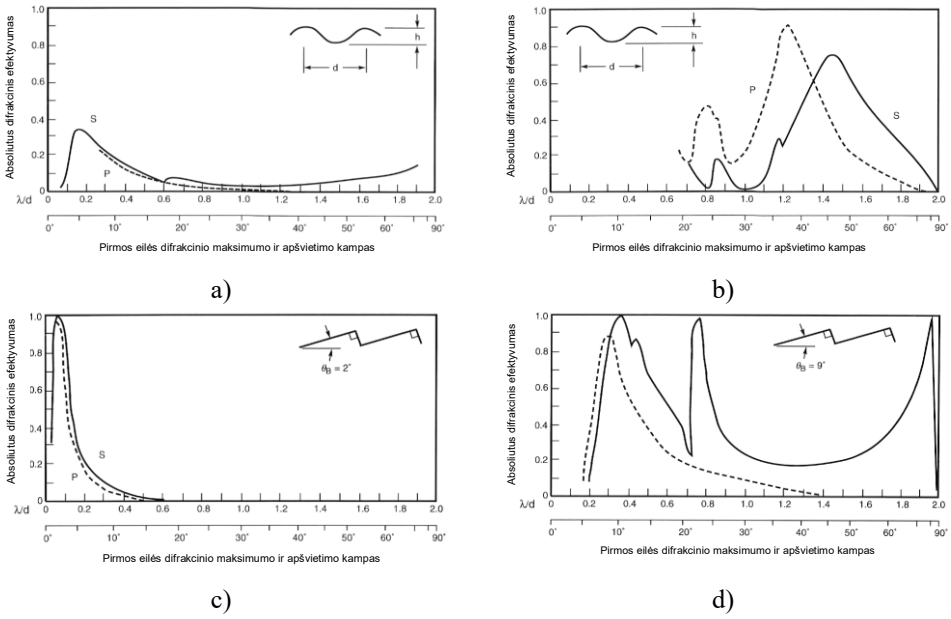

Fig.1. 10 Theoretical dependencies of the absolute diffraction efficiency of the first order diffraction peak on the wavelength and period ratio and on the angle of illumination [113]

From the diffractive lattice profile used for the properties of optical materials, from the coherent wavelength, the angle of fall, the diffraction gratings can change the amplitude and the phase of the incident electromagnetic light wave, which determines the distribution of the light intensity in the diffraction image [75, 76]. In the linear lattice diffraction spectrum, the maximum energy is accumulated at zero. In the linear grid, the energy of the groove can be accumulated in any row of the diffraction spectrum, thus reducing the energy of other, including zero-order, diffraction peaks.

The intensity of diffraction peaks is also influenced by the polarization of radiation in use. Depending on the diffraction grating profile, TM and TE polarization radiation diffraction may not differ (Fig. 1.10 a and c) or vary in different laws (Fig. 1.10 b and d). The non-polarized light diffraction efficiency curve is in the middle between the s and p curves [113]. Therefore, 45° polarization was used for the experimental and theoretical research of periodic microstructures. The following tasks are most often solved by examining two-dimensional diffractive cells:

1) Maximizing the intensity of the i-th line diffraction peak;

2) Minimizing the effectiveness of the zero-order maximum;

3) Selecting the angle of propagation of the i-th line diffraction peak.

The diffraction grid terrain and its geometric parameters are selected for these tasks [78]. All the three tasks are resolved by optical measurements. The diffraction grating terrain parameters are directly evaluated by using SEM and AJM microscopes. However, direct methods cannot always be used. Then, indirect geometric parameters (depth, period, form) can provide evaluation via optical measurement methods (diffraction and interference).

Spectroscopic ellipsometry (SE) [79, 80] can be used to study the periodic microstructure geometry. SE is a high precision and most commonly used scaterometric method which is sensitive to various structural parameters. Spectrum-elliptometric function (SEF) compared to the theoretical results with the least squares method unambiguously describes the geometric parameters of periodic microstructures. However, this method requires spectral analysis by changing the wavelength of the test radiation (200–800 nm) [79, 80].

A He-Ne laser is used to test the dichroic cells formed by two-beam interference. The intensity of the first diffraction peaks of the reflected and past energy is recorded in the photodiode. The dynamics of the periodic microstructure formation is observed by using the temporal dependence of the diffraction efficiency. This method only evaluates the properties of the material [81].

Determining the geometric parameters of deep (depth μm rows) periodic microstructures formed by various lithographic methods when using the traditional methods (AJM, SEM and SPM (scanning probe microscope)) in a non-destructive manner is prohibitively difficult or impossible at all [82]. Although a periodic microstructure of a rectangular profile is scanned by an AJM microscope, the profile pattern obtained by AJM does not correspond to the real structure geometry. With a periodic microstructure cross section, the geometry can be determined by using the above outlined methods, but it is not possible to perform this with a non-destructive method.

Diffraction efficiency η is the deviation between the theoretically ideal and the physically implemented CGH. It is the relation between the energy which passes to a particular area g_r and the total energy which enters the microstructure [82–83].

$$\eta = \frac{\sum_{m=-\frac{A}{2}}^{+(\frac{A}{2})-1} \sum_{n=-\frac{B}{2}}^{+(\frac{B}{2})-1} \left| g_{m-M_0, n-N_0} \right|^2}{MN}, \quad (1)$$

Similarly, diffraction efficiency can be expressed as the ratio of the diffracted and transmitted energy. The equation attains the following expression:

$$\eta = \frac{\eta_D}{\eta_T}, \tag{2}$$

here: η – diffraction efficiency, η_D – diffracted energy, η_T – transmitted energy.
The diffracted energy is expressed as:

$$\eta_D = \frac{\sum_{m=-\frac{A}{2}}^{+\frac{A}{2}-1} \sum_{n=-\frac{B}{2}}^{+\frac{B}{2}-1} \left| g_{m-M_0,n-N_0} \right|^2}{\sum_{m=-\frac{A}{2}}^{+\frac{A}{2}-1} \sum_{n=-\frac{B}{2}}^{+\frac{B}{2}-1} \left| g_{m,n} \right|^2}, \tag{3}$$

The transmitted energy is expressed as:

$$\eta_T = \frac{\sum_{m=-\frac{A}{2}}^{+\frac{A}{2}-1} \sum_{n=-\frac{B}{2}}^{+\frac{B}{2}-1} \left| g_{m,n} \right|^2}{MN}, \tag{4}$$

here: M and N – two-dimensional rectangular elements of the hologram plane, M_0 and N_0 – coordinates of the central reconstruction window, $G_{k,l}$ – complex transmittance, $g_{m,n}$ – discrete inverse Fourier transform, A and B – dimensions of the reconstruction window.

The total energy of phase-only holograms composes the signal $\eta = \eta_D$, while amplitude-only holograms absorb half of the energy, i.e., η_T=0.5 and η_D=0.25. As there is a twin signal, 25 percent of the energy is applied for generating the signal.

Higher diffraction efficiency values in +1 and –1 maxima of the periodic microstructure are needed in many applications as they indicate a high quality of DOE.

1.5. Polymeric micro sensor and actuator for biomedical applications

Sensors and actuators using polymeric frameworks stand out among the most promising fields of ‘smart polymers’, and it is ending up always imperative to relate artificial sensing and actuating frameworks with living creatures [83]. Testing of some promising applications has now begun in this field. The creation of fundamental comprehension of the field, its supporting advancements and current applications. This research has been committed to a wide scope of uses, specifically in the zones of humidity [84, 85], chemical [86], mechanical [87, 88], electromagnetic [89], electrochemical, piezoelectric [84, 86, 90], biosensors [84, 91] and wearable sensors and actuators. The strategies of manufacturing [92], materials characterization [90, 92] for the improvement of polymer sensors and actuators exhibitions just as

supporting electronics [85] have reached the stage of real life designing. Sensors and actuators using polymeric frameworks for biomedicine have already been designed.

The referenced methods depend on the interaction of a detecting component with the organic condition. We can assess and describe the procedures occurring in the explored organic condition due to the adjustments in the conduct of the mechanical characteristics of the utilized smart materials in microsystems or the optical properties of surfaces. Smart materials based on piezoelectricity provide a lot of opportunities for enabling inspection and analysis of biological objects in real time. Well known piezoelectric films Zirconium Titanate (PZT), Polyvinylidene Fluoride (PVDF) and Barium Titanate ($BaTiO_3$) are utilized and are seen as the detecting and activating component in a major part of microelectromechanical frameworks. In this way, they are helpful in devising novel instruments for examination in the environmental, industrial and defense areas. Besides, they might be utilized for the examination of environmental condition. The principal advantage of the utilization of such materials is their reduced size and the effortlessness when being used, as well as the control, high affectability, avoidance of radioactive materials, and biocompatibility. Subsequently, it makes them exceptionally alluring in the structure of biomedical devices.

The developed diffractive optical elements with outstanding surface, mechanical and optical properties can be used to create a therapeutic patch for the monitoring of wound healing. These medical patches are a thin nanocomposite film (Ag / PVP or Ag / PMMA) with a diffractive grating on one side and a medical adhesive on the other side.

The use of this patch to monitor the wound healing process is fairly simple: the patch is applied directly to the affected skin, and changes in the diffraction efficiency from surface deformations are observed. Changes in the geometry of the diffractive optical element due to swelling or healing (Fig. 1.11) can be detected during tests.

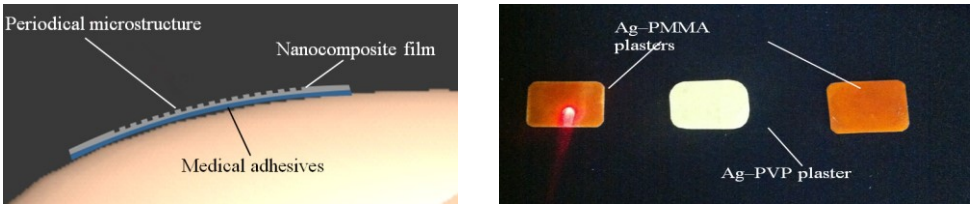

a) b)

Fig.1. 11 Medical patch a) Components b) Created prototypes [93]

One of the most promising areas is the visual cryptography system used for the visual inspection of biological samples when using MOEMS elements [93].

1.6. Visual cryptography system

It is hard to envision the human health care industry without advanced technology for the examination and biological investigation of biological structures without using functional components containing smart materials where sensitive

components provide functionality to investigate, control, or assemble synthetic and additional biological substances in the miniaturized scale, for example, pacemakers [94–95], vascular stents [96–98], hearing aids [99], cochlea inserts [100], microelectrodes [101], microendoscopes [102], micro catheter systems [103], biosensors [104, 105], viscometric sensors [106–109], and so on.

Visual cryptography is a cryptographic technique for the encryption of visual data so that unscrambling can be performed by human visual framework without the guide of PCs. Visual cryptography was first presented by Naor and Shamir [110]. They presented a visual mystery sharing plan where a picture was separated into *n* partakes so that only an individual with all *n* values could decode the secret picture. Dynamic visual cryptography is another picture concealing procedure. It consolidates two distinct strategies – visual cryptography and time-averaging geometric moiré by misusing time-averaging moiré for amalgamation of a predefined example of time-arrived at the midpoint of edges [111].

Computer produced holography is the technique which empowers digital generation of holographic interference patterns. The fundamental distinction from traditional holography is that the diffractive optical component is upgraded numerically by using a PC instead of tentatively [112]. Computer produced 3D images are being utilized for the development of high spatial frequency gratings [113], direct laser beam composing [114], and grey tone lithography [115]. Distinctive computational procedures can be utilized to register a computer produced multidimensional image of a virtual item. Fourier transform strategy and point source multidimensional images are two unique systems that a major part of calculations are employing. Adaptive-Additive algorithms [116] and Gerchberg- Saxton algorithms [117] are two normal strategies dependent on Fourier transform calculations, and they are utilized to compute conveyance of the phase hologram.

Computer generated holography has been used in picture cover-up and encryption plans by Wang *et al*. 2007. A technique for optical picture encryption using pixel-scrambling innovation and parallel Fourier transform computer produced holography was proposed in [118], where requests of pixel scrambling merely as the encoded picture are utilized as the keys to decode the first picture. Computer created holography has been misused in cryptography by using its hypothesis with the 4f double random phase encryption framework so as to execute optical picture encryption [119]. Computer generated 3D images have also been employed for three-dimensional data of various leveled encryptions [120]. Among the latest examinations, proposes symmetric and hilter kilter half and half cryptosystem dependent on compressive detecting and computer produced holography have been suggested [121].

The improvement of complex 3D microstructures dependent on computer created holography and their utilization for biomedical applications is introduced in paper [122].

Thus in order to create a visual cryptography framework, new ideas of the novel microsystem stage with a small-scale optical component for the field of biomechanics

using an optical method of picture encryption and correspondence dependent on computer produced holography ought to be proposed.

1.7. The aim of the dissertation

In the light of the study of literature, **the aim of the dissertation** is to create a vibration based thermal imprint technology on a polymer type material for manufacturing functional micro optical elements of sensors applied in visual cryptographic human health monitoring systems

TASKS:

1. To investigate the influence of forced high frequency vibration acting in the normal direction to the imprinted surface on the distribution of plastic deformations on the surface of a thermal imprinted polymer;
2. To design and investigate a sonotrode and to apply it in vibration based thermal imprint technology on a polymer for manufacturing optical microstructures in the scale useable for coherent optics;
3. To design and investigate an active-thermal sonotrode for a vibration based thermal formation technology of polymer microstructures used in coherent optics technologies;
4. To manufacture a functional element of sensors applied in a visual cryptographic human health monitoring system.

2. MODELING OF THERMAL IMPRINT PROCESS

The process of thermal compression is applied for microstructure replication on the surface of polymers. Vibration assistance increasing flow of the polymer is used as an additional means enabling quality increase of the replicated structure. However, polymers affected by vibrations have not been sufficiently researched yet.

In this chapter, microstructure replication by vibrational thermal imprint is modeled and simulated by using *COMSOL Multiphysics* software in order to reveal better specific properties of the replication process and to enable improvements of the process. The applied methodology and results were published in *Microsystem Technologies* (2019). The process is analyzed from different aspects: the imprint depth, pressure, applied force, distribution of the temperature field in time; plastic deformations of the polymer and von Misses stresses are analyzed as well. Theoretical research is verified by experiments. The results of the research showed that applying vibration excitation during the process results in a greater imprint depth in comparison with with the samples imprinted under conventional conditions.

2.1. Thermal imprinting process

The thermal imprint process is analyzed in two aspects: without vibrational excitation and with the excitation of the stamp $U_{MOLD}(t)$. The calculation scheme of the model is presented in Fig. 2.1.

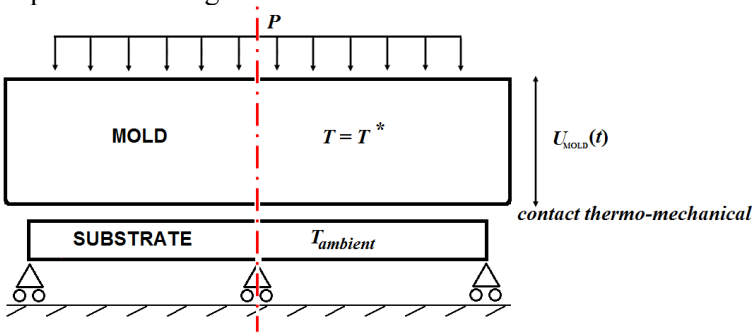

Fig. 2. 1 Computational scheme of the developed axis symmetrical model

Process modeling of the developed axis symmetrical model includes two coupled models: thermal analysis using heat transfer, and mechanical analysis using planar structural mechanics. The thickness and the width of the polycarbonate are respectively 2 mm and 11 mm. The boundaries of the mathematical model of 2-D thermal imprint are presented in Fig. 2.2.

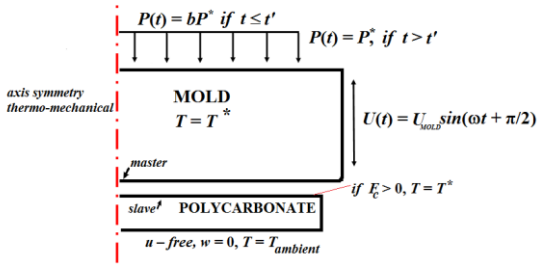

Fig. 2. 2 Boundary conditions of thermal imprint process (P – pressure, U_{MOLD} – amplitude of harmonic excitation of the mold, T^*– imprint temperature, P^* – maximal pressure, $T_{ambient}$ – ambient temperature, b – parameter, a – amplitude, t – time, ω – excitation frequency, F_c – contact force, t'– time when the working pressure was achieved)

The bottom of the polymer features zero displacements in the vertical direction and is free in the horizontal direction. The bottom of the polymer is fixed over the entire surface with respect to the vertical displacement and can only move freely horizontally. Such boundaries are chosen to best describe the behavior of the polycarbonate. The initial temperature of the polycarbonate and the stamp is 293 K, and it was preheated up to 424 K. Molding temperature $T = f(T,t)$ is defined as the function of the temperature of the stamp T (K) of time t. The deforming and deformable contact type is used in the model. The polycarbonate is considered to be deformable, and the mold is considered as the deforming tool. The model is 2-D, thus, at the contact edge, the pairs contact boundary conditions are set.

Polycarbonate behavior during simulation was analyzed without the microstructure by pressing a rectangular template (a simplified model of the mold was used to obtain preliminary data for the deep analysis), as it is intended to show the areas of plastic deformation and their distribution by comparing the conventional thermal imprint and the vibrational thermal imprint processes.

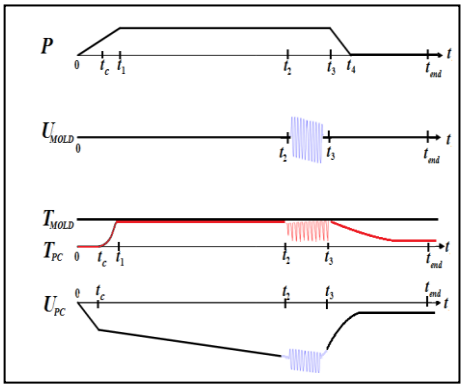

Fig. 2. 3 Parameters of the thermal imprint process during the technological process P – pressure, U_{MOLD} – displacement of the stamp due to vibrations , U_{PC} – displacement of the polycarbonate, T_{MOLD} – temperature of the stamp, T_{PC} – temperature of the polycarbonate, t – time)

In Fig. 2.3, a schematic diagram of the transient process of the thermal imprint that is simulated with the finite element model is presented. The following time instants are discussed:

- t_c – contact between the stamp and the polycarbonate.
- t_1 – the imprint pressure is reached.
- t_2 – vibrational excitation is switched on.
- t_3 – vibrational excitation is switched off.
- t_4 – the stamp is moved away.
- t_{end} – the process is finished.

In the model, the technological process (Fig. 2.3) consists of five time intervals:

- First interval $(0; t_1)$ – the working pressure from $P = 0$ until $P = P^*$ is achieved.
- Second interval $(t_1; t_2)$ – the pressure $P = P^* = \text{const}$.
- Third interval $(t_2; t_3)$ – the pressure is constant $P = P^*$, and vertical harmonic excitation, which is characterized by amplitude U_{MOLD} and frequency ω of the mold, is applied.
- Fourth interval $(t_3; t_4)$ – demolding the mold.
- Fifth interval $(t_4; t_{end})$ – polycarbonate is quenched, and the process is finished.

The pressure is defined with a function.
The pressure is described as the following function:

$$P(t) = \begin{cases} bP^*, t \le t_1 \\ P^*, \ t > t_2 \end{cases}, \qquad (2.1)$$

where b is a parameter, P^* – working pressure.

The temperature of the stamp during the entire process at all contact points is T^*. Starting from $t = 0$ up to t_c (the start point of the stamp and the polycarbonate) $P(t)$ increases linearly. After t_c, the polycarbonate is heated up to t_1 and reaches temperature T^*. Constant pressure is maintained from imprint phase t_1 to t_2 – the stamp is imprinted into the polycarbonate. Vibration excitation is applied from t_2 to t_3 – displacement of the stamp becomes harmonic. In the time interval from t_2 to t_3, vibration excitation is switched on, and the stamp does not contact with the polycarbonate constantly. Demolding takes place from t_3 to t_4, the mold is retracted, thus the imprint process is finished. Time interval from t_4 to t_{end} describes polycarbonate quenching and recovering.

2.2. Material properties

Nickel film was used to metalize the master microstructure considered to be isotropic and elastic. The general properties of the nickel film are presented in Table 2.1.

Table 2. 1 General properties of nickel film

Melting point	1455 °C
Density	8.908 g/cm^3
Young's modulus	200 GPa

A polycarbonate material was used for hot imprinting, and the properties of the material are presented in Tables 2.2–2.4. Polycarbonate is a substrate material; it is an amorphous polymer having a glass transition temperature of about 423 K. The set of graphs in *COMSOL Multiphysics* Materials Library describes polycarbonate parameters in relation to temperature as presented in Fig. 2.4.

Table 2. 2 Thermal properties of PC (Pérez, Vilas *et al*. 2010) [129]

Melting temperature *(T_m)*	267 °C
Glass transition temperature *(T_g)*	150 °C
Heat deflection temperature at 10 kN	145 °C
Heat deflection temperature at 0.45 MPa	140 °C
Heat deflection temperature at 1.8 MPa	128–138 °C
Upper working temperature	115–130 °C
Lower working temperature	–40 °C
Linear thermal expansion coefficient	65–70*10^{-6} /K
Specific heat capacity	1.2 kJ/(kg*K)
Thermal conductivity 23 °C	0.19–0.22 W/(m*K)

Table 2. 3 The mechanical properties of PC [130]

Young's modulus	4.1 GPa
Tensile strength	55–75 MPa
Compressive strength	>80 MPa
Poisson's ratio	0.373
Coefficient of friction	0.31

Table 2. 4 Physical properties of PC [130]

Density	8.908* 10^3 kg/m^3
Refractive index	1.584–1.586
Water absorption at equilibrium	0.16–0.35%
Water absorption – over 24 h	0.1%
Light transmittance	88%

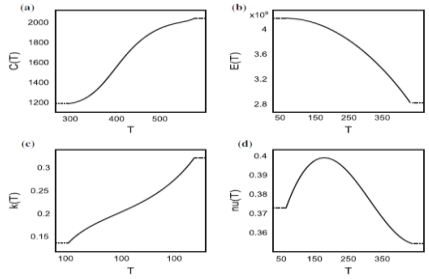

Fig. 2. 4 Set of plots describing the parameters of the polycarbonate with respect to temperature. Material heat capacity is given in a, elastic modulus is given in b, thermal conductivity is given in c, and Poisson's ratio is given in d

Simulation of the thermal imprint process with coupled thermo-mechanical analysis includes heat transfer, structural mechanics, and thermomechanical contact analysis. The following material parameters are taken into account: thermal conductivity (k), density (ρ), heat capacity (c_p), Young's module (E), Poisson's ratio (ν) and thermal expansion coefficient (α)), which is defined as a temperature function.

The mechanical properties of the materials and the behavior of the materials during the thermal imprint process are very important in determining the optimal parameters of the process in order to replicate defect-free microstructures. Precise determination of the critical parameters of the material below or above T_g is considered to be an essential modeling requirement. Elastic plastic materials are used to describe the deformation under high stress.

Piezoelectric material Lead zirconate titanate (PZT-5) piezoceramic rings are applied as actuators in the sonotrode device design actuator operating in the thickness mode (d_{33} direction). The characteristics of PZT-5 are presented in Table 2.5.

Table 2. 5 Properties of PZT-5

General	
Density $\left(10^3 kg/m^3\right)$	7.75
Curie temperature (°C)	350
Elastic Constants	
c_{11}^E (GPa)	15
C_{33}^E (GPa)	18.8
Piezoelectric constants	
e_{31} $\left(C/m^2\right)$	–10.6
e_{33} $\left(C/m^2\right)$	24.8
e_{15} $\left(C/m^2\right)$	38.2
Dielectric constants	
ε_{11}^T $\left(10^{-9} F/m\right)$	1730
ε_{33}^T $\left(10^{-9} F/m\right)$	1700

2.3. Elasto-plastic polycarbonate model

The micro hot imprint process is performed near the glass transition temperature of the polycarbonate, at which it behaves as an elasto-plastic material. Under a constant load, a material would undergo two stages of deformation: instantaneous elastic deformation ε_e at the beginning of the process followed by plastic deformation ε_p. The total deformation is described as:

$$\varepsilon = \varepsilon_e + \varepsilon_p . \tag{2.1}$$

The behavior of an elasto-plastic material can be described as a model with a set of spring and friction components. Rheological models of an elasto-plastic body with hardening are given in Fig. 2.5 and Fig. 2.6, where σ_k – yield strength, E_2 – modulus of plasticity, E_1 – modulus of elasticity.

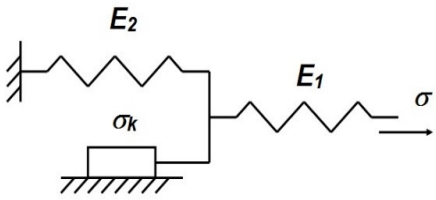

Fig. 2. 5 Schematic diagram of elasto-plastic model

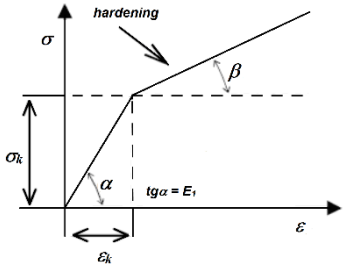

Fig. 2. 6 Deformation characteristic

In the figure means:

$$tg\alpha = E_1 , \; tg\beta = \frac{E_1 \cdot E_2}{E_1 + E_2} \text{ (Neto, Peric, Owen, 2008).} \tag{2.2}$$

Elastic-plastic models in FE systems require data in the form of elastic constants in order to describe the elastic characteristics and parameters which describe the yield, hardening and flow behavior in order to describe the plastic behavior.

In this model, the yield function of von Misses was used:

$$\sigma_Y = \sqrt{\frac{1}{2}\left(\sigma_1 - \sigma_2\right)^2 + \left(\sigma_2 - \sigma_3\right)^2 + \left(\sigma_1 - \sigma_3\right)^2} , \tag{2.3}$$

where $\sigma_1, \sigma_2, \sigma_3$ are principal stresses, and σ_Y is the equivalent stress [127],

The yield stress is obtained by [62]:

$$\sigma_y(T) = E(T).\varepsilon_y(T) , \tag{2.4}$$

where T – the present temperature, E(T) – Young's modulus function, εy(T) – the yield strain function. The polycarbonate E(T) function is taken from the *COMSOL*

Multiphysics Materials Library, the εy(T) function was created as a linear function according to the results published in [134]. The yield strain varies from 8% to 5% when the temperature varies from 293 K to 417 K. The tangent modulus and the yield stress depend on the temperature.

The hardening function is a function of the effective plastic strain, and it describes the behavior which starts from the yield stress of the material. The hardening model is a phenomenon that the yield stress increases with the further plastic strain. Isotropic hardening has been proposed to define the modification of the yield surface during plastic deformation. By using this model of hardening, it was assumed that the initial yield surface expands uniformly without distortion and translation as flow of plastic takes place. The isotropic tangent modulus is ETiso = MPa [134]. Lagrangian formulation was used for incremental general nonlinear analysis in COMSOL Multiphysics.

2.4. Mathematical model

The thermo-mechanical coupled finite element model of the thermal imprint process was created. The time-dependent thermal model was implemented. The inputs of the model were as follows: material properties, temperature, stamp pressure, vibration frequency, amplitude and duration of each phase of the process. The outputs of the model were the temperature and displacement characteristics of the deformable body versus time and their distribution in the imprinting phases.

FEM analysis related to thermal coupled thermo-mechanical contact interaction dynamics was proposed. Heat was released during the transformation of the solid state phases, thus affecting the thermal field. Both mechanical and thermal properties varied with temperature and deformation. By using the laws of equilibrium and transfer, field equations can be derived from temperature T, displacement u_{PC}, and Navier equations:

$$G\nabla^2 u_{PC} \frac{1}{3}(G+3K)\varepsilon = K\alpha T \tag{2.5}$$

Heat transfer plays a critical role in the imprint process. The mathematical model for heat transfer through conduction is expressed with the following heat equation:

$$\rho c_p \frac{\partial T}{\partial t} - \nabla(k\nabla T) = 0 \tag{2.6}$$

In the above equations, u_{PC} is the substrate displacement vector, ε – the total strain tensor, T – temperature, G – shear modulus, K – rock's bulk modulus, α – thermal expansion coefficient, k – thermal conductivity, ρ – density, c_p – heat capacity. The heat transfer is calculated separately because stress does not alter significantly because of the temperature field.

The polycarbonate imprint is defined by the matrix state equation:

$$M\ddot{u} + C\dot{u} + Ku = F(t) \tag{2.7}$$

where: M – mass matrix, C – damping matrix K – stiffness matrix, and vector $\{F\}$ defines the contact force:

$$\{F(t)\} = \begin{cases} \{0\}, & if\ u^i_{MOLD} < u^i_{PC} \quad or \quad \dot{u}^i_{MOLD} < 0 \\ \{P_{CONT}(\dot{u}^i_{PC}, u^i_{PC}, t)\} & if\ u^i_{MOLD} \geq u^i_{PC} \quad and \quad \dot{u}^i_{MOLD} \geq 0 \end{cases} \tag{2.8}$$

where: $\{P_{CONT}(\dot{u}_{PC}, u_{PC}, t)\}$ – vector of nonlinear interaction in the contact pair:

$$P_{CONT} = \left(k_{CONT} \cdot \dot{u}^i_{PC}\right)^2 + c_{CONT} \cdot \dot{u}^i_{PC} \tag{2.9}$$

where: u^i_{MOLD} and $\dot{u}^i_{MOLD}$ – vertical displacement and velocity of the mold at time t, u^i_{PC} and $\dot{u}^i_{PC}$ – vertical displacement and velocity of the polycarbonate at time t, k_{CONT} and c_{CONT} – stiffness and damping coefficients of the coupling element, respectively, where i – index – denotes the nodes of edges which are in contact.

The contact model is included into the FE model of the thermal imprint process and describes the contact forces acting at the points of the edges of the polycarbonate. The coefficient of friction between the stamp and the polycarbonate was sourced from literature, i.e., it is a temperature-dependent coefficient. (Pouzada *et al*. 2006). Therefore, the friction coefficient value in the dissertation was determined by temperature.

The thermal imprint process is modified by imprinting duration (10 s and 20 s) and pressing nature (constant pressing and pressing with kinematic excitation of the stamp).

The amplitude of the vibrations was kept at 1 μm, and the selected frequency was 600 Hz. The stationary polycarbonate process of the temperature was not steady at the imprinting time of 10 s, and it became steady at 20 s.

2.5. Experimental verification

In order to verify the model, experiments of the vibrational thermal imprint were conducted. For the experimental verification, the employed vibroactive device contained a stack of the PZT-5H rings, the front mass, a heating element, and a stainless steel ring. A schematic diagram of the vibroactive device is presented in Fig. 2.7.

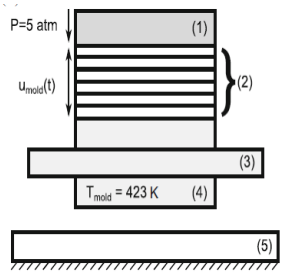

Fig. 2. 7 Vibroactive device comprises a stainless steel ring (1), six piezoceramic rings (2), a heating element (3), a front mass (4), and a polycarbonate (5)

The contact pattern between the vibroactive device and the polycarbonate is presented in Fig. 2.8.

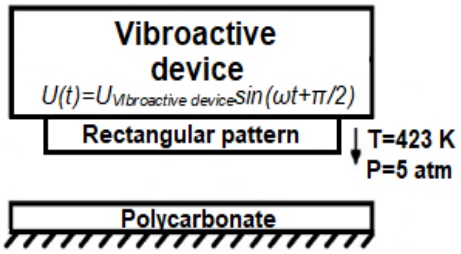

Fig. 2. 8 Thermal imprint with high frequency vibration assistance

In the vibroactive device (Figs. 2.7–2.8), the operation frequency of 600 Hz and the amplitude of 1 μm was used. The procedure of the thermal imprint involved the following steps:

In general, the simulation model and the obtained numerical results provide us with useful understanding of the fundamental formation mechanism during the hot imprint process and serve as a useful guide for specifying the optimal processing conditions for a variety of hot imprint applications.

The hot imprint process can be divided into three steps: heating, imprinting, and demolding. In this case:

1) Heating. The initial stage of the experiment starts at room temperature of the mold, i.e., at 293 K (ambient temperature). When the stamp touches the polycarbonate, the heating of the mold up to 421 K temperature begins. During the heating process, heat is carried to the polycarbonate, and it starts to deform due to the effect of the heat.

2) Imprinting. During this process, the mold goes down and presses the polycarbonate, at the same time, the contact force between the mold and the polycarbonate increases. The polycarbonate is being further deformed, and plastic deformation appears. For hot imprinting, several parameters are set to be considered, such as the time of imprinting of 10 s and 20 s. Vibrations are applied for the time period of 0.05 S., thus the imprinting step is performed several times according to the selected parameters which are presented in Table 2.6.

3) Demolding. In this step, the hot mold ($T = 421$ K) is demolded, and, finally the polycarbonate is cooled. The polycarbonate assumes the form of the mold's periodic microstructure.

Table 2. 6 Experimental matrix

Duration of imprint, s	Duration of vibratory excitation, s	Temperature of imprint, K	Imprint pressure, Atm
10	-	423	5
10.05	0.05	423	5
20	-	423	5
20.05	0.05	423	5

The experiment was performed according to the parameters which are outlined and presented in the Table 2.6.

2.6. Results

2.6.1 Finite element modeling results

From the finite element model, a number of results were obtained in order to know the effect of the different time periods of the process, with and without vibratory excitation. Also, the quality of the mechanical hot imprinting and the achieved residual depth are presented in this chapter.

Figures 2.9–2.17 demonstrate mold displacement and polymer recovering after mold retraction.

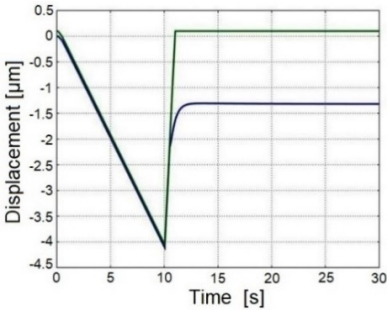

Fig. 2. 9 Dependency of mold displacement with respect to time: imprint duration t_2 = 10 s, frequency ω = 0 Hz (green – mold, blue – polycarbonate)

Thermal imprint for a time period of 10 s without vibratory excitation (Fig. 2.9) enables to obtain the imprint on the polycarbonate specimen; the obtained depth during the process is 1.3 μm as shown in the graph with the blue line.

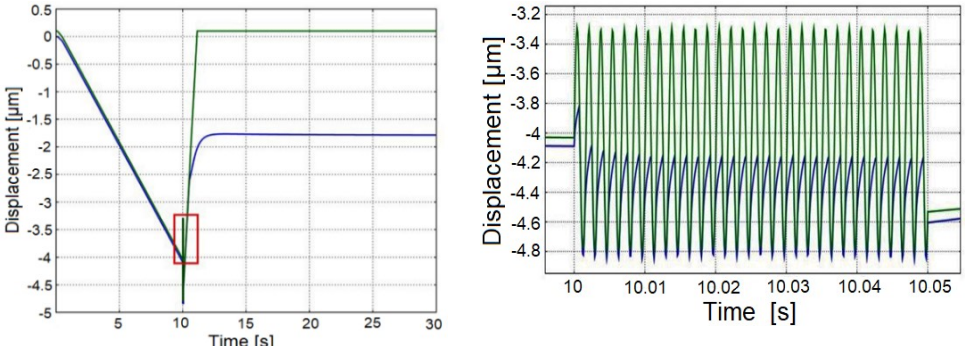

(a) (b)

Fig. 2. 10 Dependency of mold displacement with respect to time: imprint duration t_2 = 10 s, frequency ω = 600 Hz (green – mold, blue – polycarbonate). The process runs from 0 to 30 s (a), and the time interval of the application of vibratory excitation is 10 to 10.05 s (b)

During the next step of the thermal imprinting process, the time duration for the printing was 10 s with vibratory excitation for the time duration of 0.05 s. The obtained results (Fig. 2.10) show that, by applying vibratory excitation, the resudual depth of the rectangular pattern is achieved at 1.75 µm. It means that the application of vibratory excitation results in an increased profile depth (by 0.45 µm) for the same process duration.

In (Fig. 2.10 a), the dependency of the mold displacement with respect to time imprint duration t_2 = 10 s, frequency ω = 600 Hz (green – mold, blue – polycarbonate) is presented, and in (Fig. 2.10 b), the time interval of the application of the vibratory excitation for the interval 10 to 10.05 is presented in order to understand the behavior of the printing process during the application of vibratory excitation.

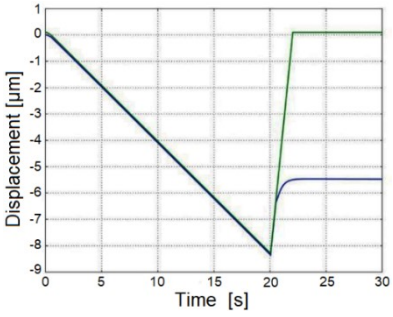

Fig. 2. 11 Dependency of mold displacement with respect to time: imprint duration t_2 = 20 s, frequency ω = 0 Hz (green – mold, blue – polycarbonate)

Figure 2.11 demonstrates the thermal imprint for the time period of 20 s duration without vibratory excitation. After the retraction of the mold, the depth of the imprinted rectangular pattern achieved 5.4 µm. From the obtained results, it is clear that the increase in the process duration leads to a higher profile depth (by 4.1 µm) than the depth achieved during the time period of 10 s when the process was performed without vibratory excitation.

Figure 2.12 shows the time period for the thermal imprinting process of 20 s duration, and, by applying the vibratory excitation for 0.05 s of the time period, the achieved residual depth is 5.9 µm. It suggests that the largest residual profile depth is observed when the thermal imprint of 20 s duration with an assistance of vibratory excitation is performed. In this case, the profile depth is 5.9 µm, or, by 0.5 µm larger when compared to the process without vibratory excitation, but for the same duration.

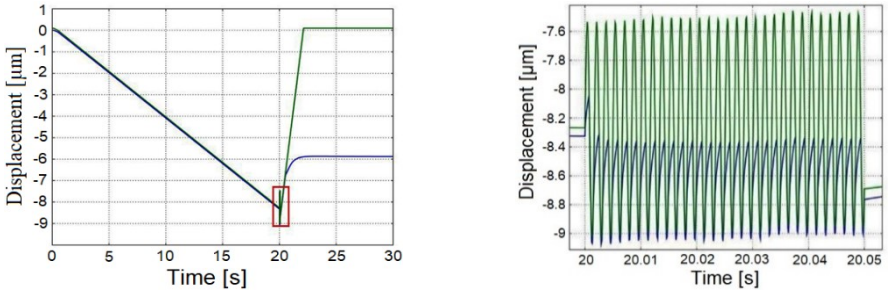

(a) **(b)**

Fig. 2. 12 Dependency of mold displacement with respect to time: imprint duration t_2 = 20 s, frequency ω = 600 Hz (green – mold, blue – polycarbonate). The process runs from 0 to 30 s (a), and the time interval of the application of vibratory excitation is 20 to 20.05 s (b)

The obtained results demonstrate that the application of vibratory excitation increases the imprinted profile depth by 0.45 and 0.5 µm when the process duration is 10 and 20 s, respectively.

Subsequently, in order to know the change in the applied pressure and traction force during the hot imprinting process, the dependency of the pressure and traction force with respect to time are analyzed. The obtained results are presented in (Fig. 2.13 a–d).

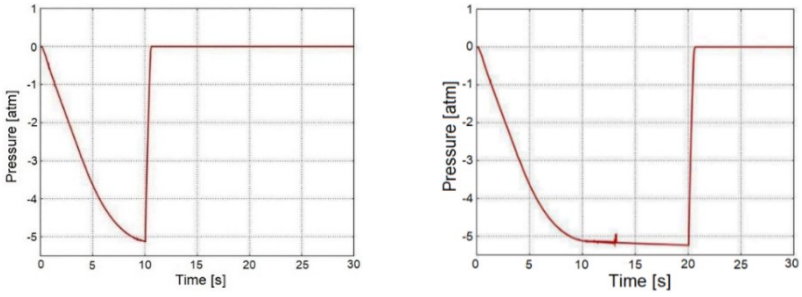

(**a**) (**b**)

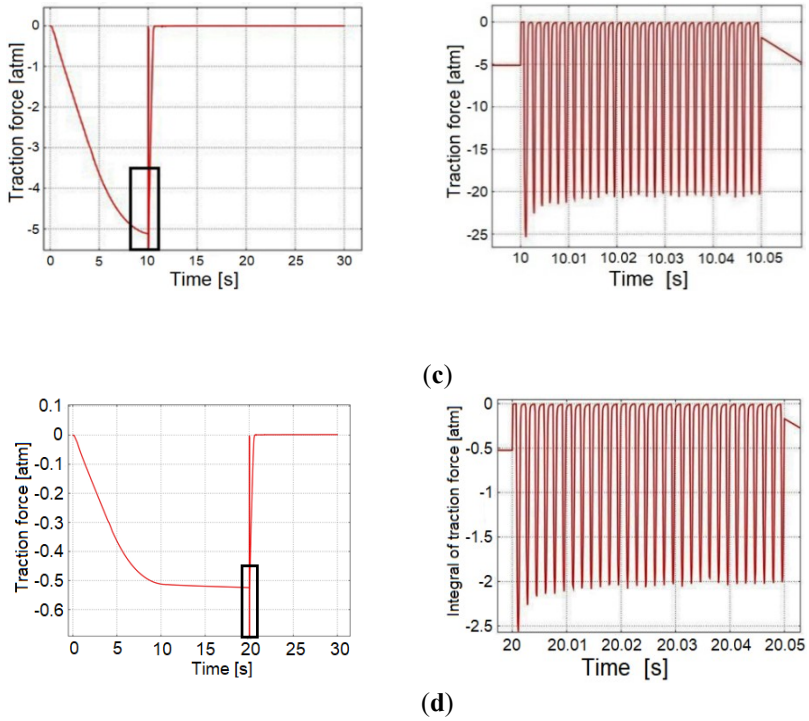

Fig. 2. 13 The dependency of the mold pressure on the polycarbonate with respect to time: (a) imprint duration $t_2 = 10$ s, process without vibratory excitation, (b) imprint duration $t_2 = 20$ s, process without vibratory excitation, (c) imprint duration $t_2 = 10$ s, process with vibratory excitation (c), and (d) imprint duration $t_2 = 20$ s, process with vibratory excitation

Figure 2.13 (a) – (b) demonstrates the pressure dependency on time curves for the time duration of the 10 s and 20 s, respectively. It demonstrates that the pressure is almost stabilized after the imprint duration of 10 s, and the obtained value of the pressure is observed as 5.1 atm. The increase of the process duration by 10 s with the total time reaching 20 s for hot imprinting while considering the graph shown in (Fig. 2.13 b) yields the rise of pressure by 0.1 atm (up to 5.2 atm); therefore, it can be stated that the process becomes stationary after 10 s.

Fig. 2.13 (c) – (d) demonstrates the traction force after the hot imprinting process with vibratory excitation. The process of 10 s duration (Fig. 2.13 (c)) is showing almost 10 times higher values (5.1 atm) when compared to the traction forces obtained after 20 s (0.52 atm) (Fig. 2.13 (d)). This can be explained by the dissimilar temperature field of the polycarbonate at different process durations (10 s and 20 s), respectively.

In Fig. 2.14, the temperature dependence with respect to time is presented. We wish to find out whether the temperature is stable during the process or after the process ends. In Fig. 2.15 (a) and (b), the values demonstrate the temperature dependence with respect to time values of 10 s and 20 s without any vibratory excitation respectively.

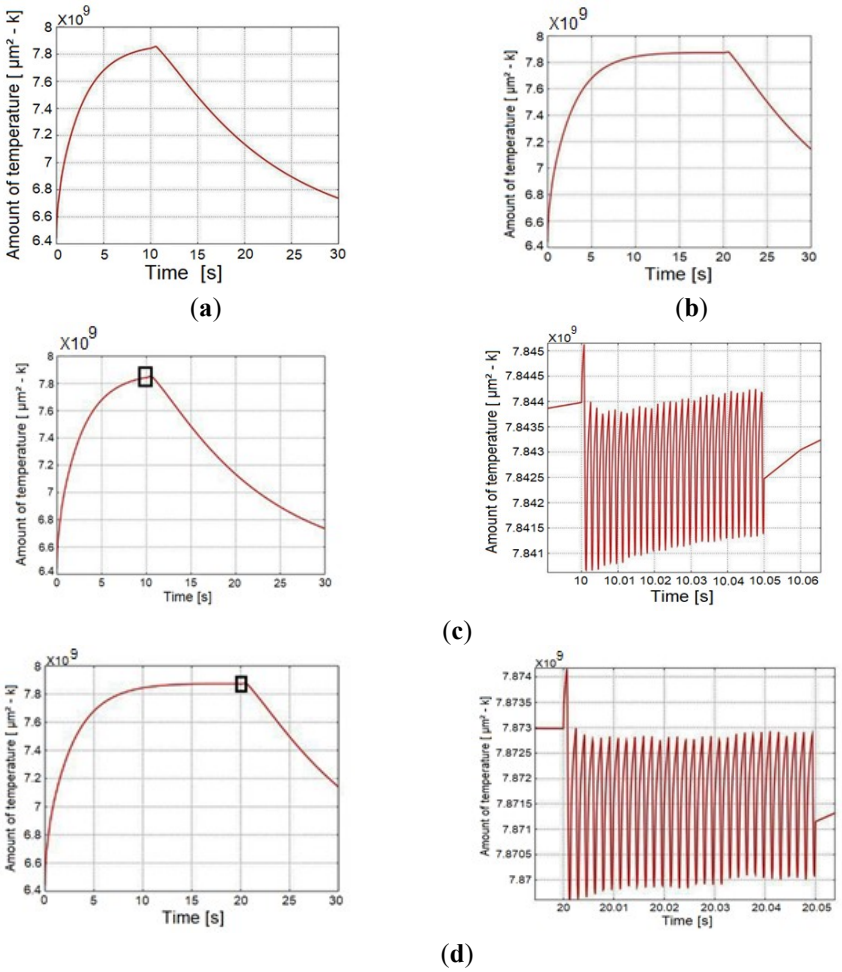

Fig. 2. 14 Dependency of the amount of temperature with respect to time: (a) imprint duration 10 s, process without vibratory excitation, (b) imprint duration 20 s, process without vibratory excitation, (c) imprint duration 10 s, process with vibratory excitation, (d) imprint duration 20 s, process with vibratory excitation

From Fig. 2.14 (a) and (b), it is clear that no significant change is observed. In Fig. 2.14 (c), it is clear that the process is not stable yet, and, as the application of vibration excitation slightly increases, the temperature is observed. However, from Fig. 2.14 (d), after a 20 s increment of the 10 s in the previous time period, the process is already stabilized, and it is possible to state that the application of vibration excitation does not cause any significant increase of the temperature.

Residual polycarbonate plastic deformations at the end of the compression process are presented in Fig. 2.15 with and without vibratory excitation.

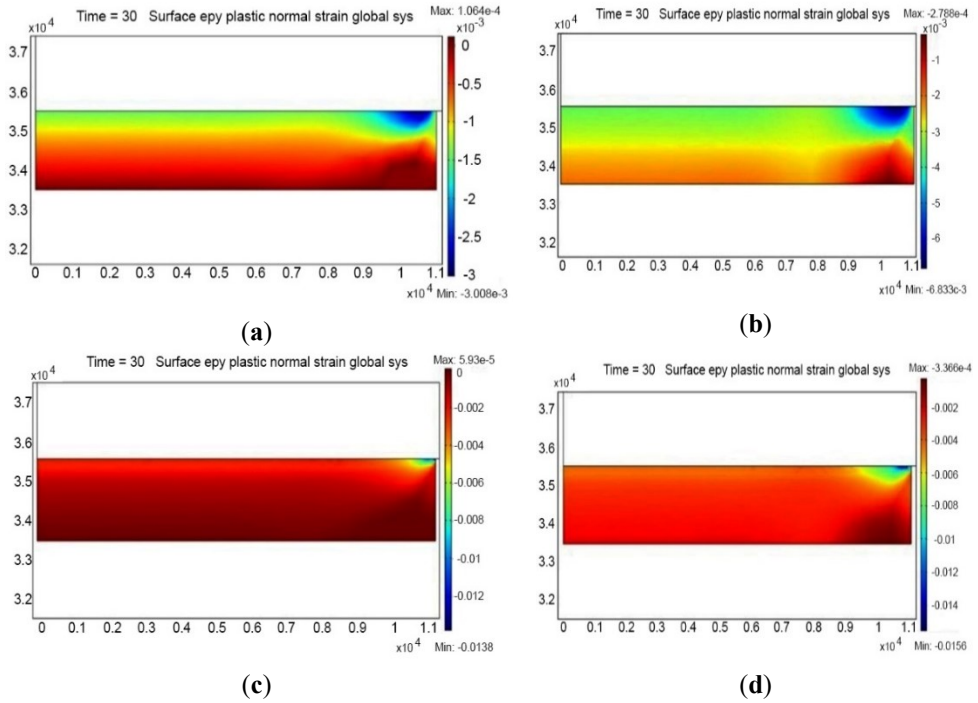

Fig. 2. 15 Residual plastic deformations field on the polycarbonate surface after thermal imprint (30 s from the onset of the process): (**a**) imprint duration 10 s, process without vibratory excitation, (**b**) imprint duration 20 s, process without vibratory excitation, (**c**) imprint duration 10 s, process with vibratory excitation, (**d**) imprint duration 20 s, process with vibratory excitation. The horizontal and vertical axes represents the length and the thickness of the specimen

In Fig. 2.15, the residual polycarbonate plastic deformation field at the end of the compression process for the total time of 30 s is presented. The process without any vibratory excitation is presented in Fig. 2.15 (a) and (b), and inconsistent values of polycarbonate plastic deformation are observed.

However, due to the applied vibration excitation, the profile of plastic deformation is equally concentrated in the top layer of the polycarbonate as shown in Fig. 2.15 (c) and (d).

The residual Von Misses stress field after the process is shown in Fig. 2.16. In Fig. 2.16 (a) and (b), we observe samples without any vibratory excitation, whereas (c) and (d) feature vibratory excitation. The process features a time period of 10 and 20 s duration.

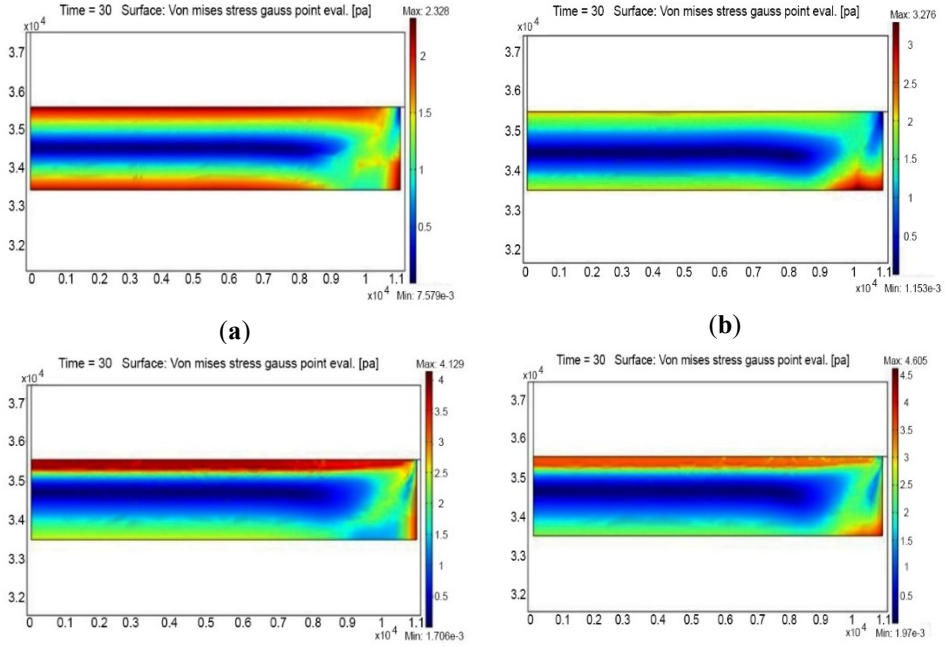

Fig. 2. 16 Residual Von Misses stress field on the polycarbonate surface after thermal imprint (30 s from the onset of the process): (**a**) imprint duration 10 s, process without vibratory excitation, (**b**) imprint duration 20 s, process without vibratory excitation, (**c**) imprint duration 10 s, process with vibratory excitation, (**d**) imprint duration 20 s, process with vibratory excitation. The horizontal and vertical axes represent the length and the thickness of the specimen

When applying Vibratory Excitation, von Misses stresses are concentrated in the upper layer of the polycarbonate as shown in Fig. 2.16 (c) and (d), and the maximum values of the stresses reach up to 4 and 3.5 Pa when the pressure duration is 10 and 20 s, respectively. However, the samples without vibratory excitation are characterized by various Von Misses stress values in the upper polycarbonate layer.

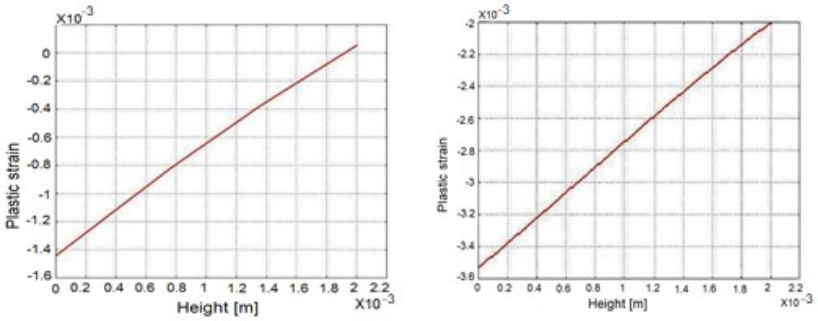

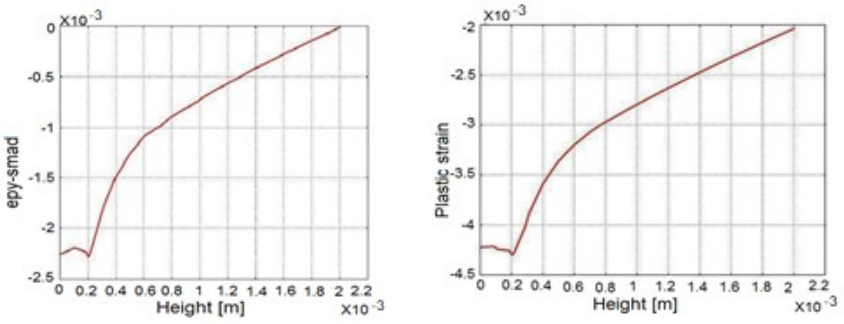

(**c**) (**d**)

Fig. 2. 17 Change of plastic deformations in the vertical cross-section at the point of the symmetry axis of the model (time point – 30 s): (**a**) imprint duration 10 s, process without vibratory excitation, (**b**) imprint duration 20 s, process without vibratory excitation, (**c**) imprint duration 10 s, process with vibratory excitation, (**d**) imprint duration 20 s, process with vibratory excitation

Figure 2.17 demonstrates the distribution of plastic deformations in the cross-section of the polycarbonate specimen after the termination of the technological process (time point – 30 s).

As shown in Fig. 2.17 (a) and (b), plastic deformations of the polycarbonate cross-section are linear without any vibrational excitation. On the other hand, Fig. 2.17 (c) and (d) reveals that the application of vibration excitation changes the distribution of the plastic deformations of the polycarbonate cross-section to nonlinear. The linearity of plastic deformations is maintained within the zone of 0.2 μm from the upper surface of the polycarbonate sample, it is here that the highest values of plastic deformation are observed. Such a uniform zone in terms of the deformed body is very significant when replicating high quality microstructures.

2.6.2 Experimental results

After completing the step of mechanical hot imprinting, the samples are analyzed by using an atomic force microscope (AFM). The main idea to use this technique is the feasibility of checking the quality of the replicated microstructure on the polycarbonate so that attention could be focused on the depth of the replicated profile on the polycarbonate.

According to the experimental matrix presented in Table 2.6, the duration of the imprinting time, the duration of vibratory excitation, and the temperature for the printing and imprinting pressure were investigated.

Figure 2.18 demonstrates a 3D image (a) and the profile topology (b) of the sample which was prepared without any vibratory excitation, and the time duration of the imprinting was 10 s.

The results obtained under the same process conditions during the simulation show that the achieved depth is 1.3 μm. On the other hand, the results determined from the 3D image and the profile topology when using an atomic force microscope achieved depth of the imprinting without assistance of vibratory excitation is 1.2 μm.

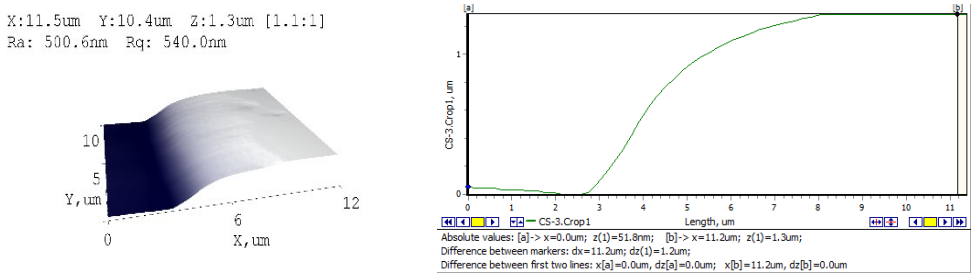

(**a**) (**b**)

Fig. 2. 18 3D image (**a**) and profile topology (**b**) of the specimen replicated at duration of 10 s without vibratory excitation

From the comparison of the simulated and experimental results under the same conditions of the experiment without vibratory excitation and the time duration of 10 s, the difference in the values is 8.33%.

For the next step, an experiment was performed with the time duration of 10 s, and then vibratory excitation was applied for the time duration of 0.05 s. The obtained 3D image and profile topology are presented in Fig. 2.19 (a) and (b), respectively.

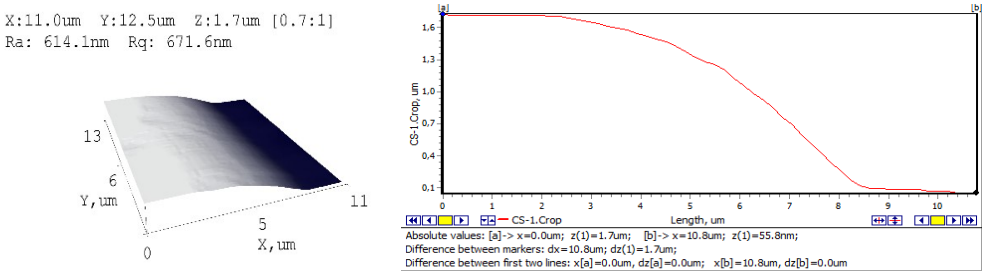

(**a**) (**b**)

Fig. 2. 19 3D image (**a**) and profile topology (**b**) of the specimen replicated at 10.05 s duration including vibratory excitation

Fig. 2.19 demonstrates the 3D image (a) and the profile topology (b) of the sample which was prepared with vibratory excitation and time duration for 10.05 s imprinting.

In Fig. 2.19 (a) and (b), it is clearly visible that the application of vibratory excitation increases the depth of the profile up to 2.17 μm. In other words, we could state that the profile depth is increased by 0.5 μm compared to the samples without vibratory excitation. The depth of the sample simulated under analogous process conditions is 1.75 μm.

The difference between the experimental and simulation results with the application of the vibratory excitation is 2.9%.

In addition, from Fig. 2.19 (b), it may be observed that the lower region of the microstructure is less elevated than the values shown in Fig. 2.18 (b). This proves that

vibration excitation reduces adhesion between the stamp and the polycarbonate. Vibration excitation reduces surface tension not only in the boundary region but also in the center of the sample.

For the next step, thermal imprinting was performed with the time duration of 20 s, and no vibratory excitation was applied. The obtained 3D image and profile topology are presented in Fig. 2.20 (a) and (b), respectively.

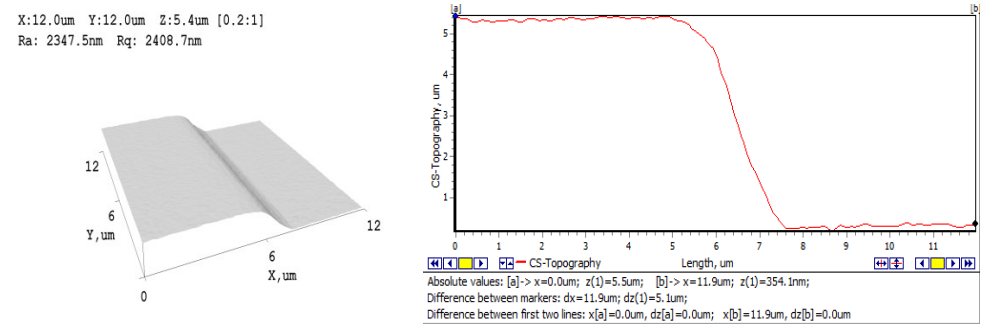

(**a**) (**b**)

Fig. 2. 20 3D image (**a**) and profile topology (**b**) of the specimen replicated at 20 s duration with and without vibratory excitation

Fig. 2.20 demonstrates a 3D image (a) and the profile topology (b) of the sample which was prepared without any vibratory excitation and time duration for the imprinting at 20 s.

AFM images revealed that the profile depth of the replicated pattern after the process of the thermal imprint is 5.1 µm, while the simulated profile depth obtained under the same process conditions is 5.4 µm. The difference between the experimental values and the numerical values is 5.9%.

For the final step, the experiment was performed with the time duration of 20 s, and then the vibratory excitation was applied for the time duration of 0.05 s. The obtained 3D image and the profile topology are presented in Fig. 2.21 (a) and (b), respectively.

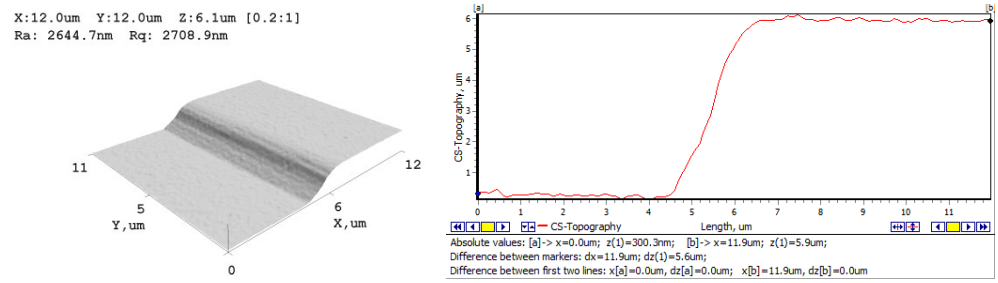

(**a**) (**b**)

Fig. 2. 21 3D image (**a**) and profile topology (**b**) of the specimen replicated under the duration of 20.05 s including vibratory excitation

In Figure 2.21, it is proved that the application of vibration excitation increases the depth of the profile by 0.5 μm (the profile depth is 5.6 μm) in comparison with the sample obtained with no vibration excitation. 5.9 μm depth was obtained by simulation. The difference between the experimental values and the simulated values is 5.6%.

2.7. Chapter conclusion

1. In this chapter, a simulation of the vibrational thermal imprint and its experimental verification was performed. The simulation results show that the application of vibratory excitation can lead to a deeper profile than that obtained without vibratory excitation. An increase of depth by 0.45 or 0.5 μm was observed when the process duration was 10 s and 20 s, respectively.
2. The FEM model was verified experimentally. The profile depth of 1.3 μm was obtained after the process of 10 s duration without vibration excitation. The application of vibration excitation allows increasing the profile depth up to 1.75 μm in the case of a process of the same duration. The profile depth of 5.4 μm and 5.9 μm was obtained after the 20-second process without and with vibration excitation, respectively. The results of the simulation and experimental research do not differ more than by 9%, which is within acceptable limits.
3. In addition, it was determined that the application of vibration excitation at any stage of the process results in concentration and uniformity of plastic deformations and residual von Misses stresses on the polycarbonate's surface. The linearity of plastic deformations is maintained within the zone of 0.2 μm from the upper surface of the polycarbonate sample. This uniform zone of the deformable body is very important for replicating high-quality microstructures.
4. It was determined in this chapter that the application of vibration excitation during the thermal imprint process increases the depth of imprinted profiles and results in uniform distribution of plastic deformations and Von Misses stresses.

3. SONOTRODE MODELING DESIGN, REALIZATION AND MICROSTRUCTURE REPLICATION

To perform further thermal hot imprinting, it is necessary to design and model a sonotrode device which will be used as a vibro-active device in the process for the assistance of vibratory excitation. Firstly, the chapter explains the modeling of the sonotrode device design. Also, in order to know the function of the sonotrode device, the bump test was conducted, and, for the resonance and anti-resonance frequency, impedance analysis was done with various conditions; it is also presented in this chapter.

Secondly, the chapter explains the experimental setup for the mechanical hot imprinting technology with the newly designed sonotrode, the thermal temperature distribution for the front mass, the bump test, and impedance analysis. Also, the chapter contains the numerical simulation of the prestressed sonotrode device in order to know the uniform displacement field throughout the entire operating surface and various points. Moreover, the determination of the operating frequency of the sonotrode device model was simulated by using the *Comsol Multiphysics 5.4* software package. For the determination of the reaction of applied frequency, the sonotrode device reaction in the normal downward direction to the substrate is presented in this chapter.

Finally, the chapter describes the quality evaluation method of the printed microstructure on the polycarbonate material with various conditions of the experiments and evaluates the use of the diffraction efficiency and optical microscope. Also, the results were compared with and without applying vibratory excitation. The modeling, the test results and the employed methodology are published in conference proceedings and in Journal *Mechanika*.

3.1. Modeling (Designing) of sonotrode

In order to increase the quality of the replication process, the primary objective is to design the sonotrode by introducing high-frequency oscillations to the replication process. The primary function of the sonotrode is to transmit normal to surface mechanical vibrations to the formable poly-carbonate material. In this chapter, a design is proposed, and its functional analysis is conducted.

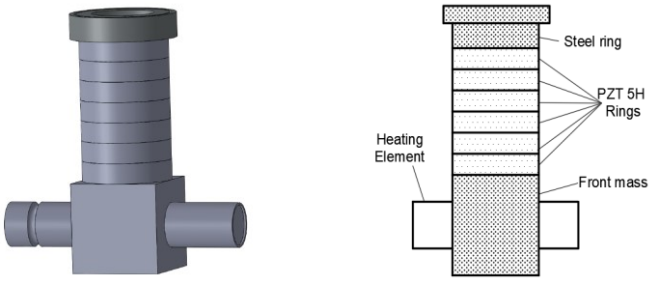

Fig. 3. 1 3D model of the designed sonotrode **(a)**, and the essential elements of the designed sonotrode model **(b)**

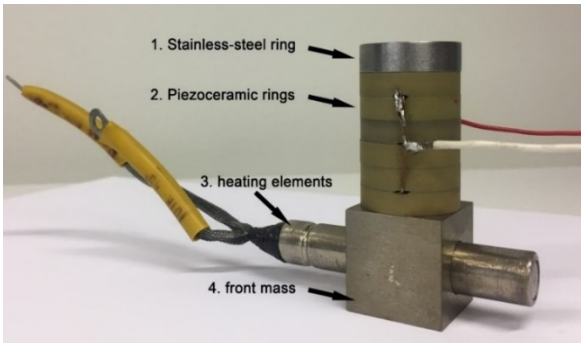

Fig. 3. 2 Photo of the designed sonotrode: 1 – steel ring, 2 – piezoceramic rings, 3 – heating element, 4 – front mass

The sonotrode was designed by using the *3D CAD Solid Works 2017* software. The basic model is drawn according to the dimensions as shown in (Fig 3.15 (a)). Fig 3.1 (a) and (b) presents the 3D model and the essential elements of the sonotrode device, respectively. The physical model of the sonotrode is presented in Fig. 3.2. Starting with the Stainless steel ring (22 mm outer diameter and 9 mm inner diameter; height 5 mm), PZT Rings (22 mm outer diameter and height 5 mm), Conical Heating element (11 mm diameter and 52 mm length) connected to the front mass steel box (22 mm x 22 mm), each part is drawn, and then they are assembled, preassembled parts of the sonotrode are connected via a high tensile steel 4340 screw (37mm length and 2 mm diameter) as shown in Fig. 3.3.

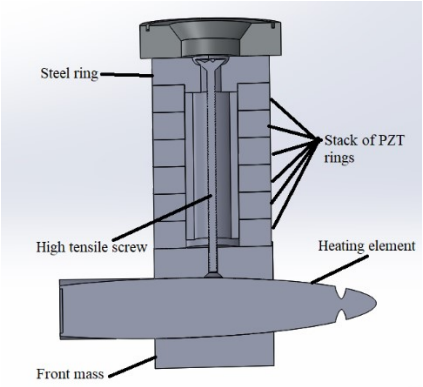

Fig. 3. 3 Cross-section view of the assembled sonotrode device

In order to avoid deflection of shape in the Sonotrode device while vibrating at a high speed, a stainless steel ring was specially designed which is located on the top of the device and connected on the top of the piezoceramic rings (diameter 20 mm); below the stainless steel ring, there are piezoceramic rings (diameter 20 mm). The piezoceramic rings (diameter 20 mm) are placed in the middle of the device. There are 6 piezoceramic rings with a total height of 30 mm. The reason for placing 6 PZT rings is that high vibrations make the process faster and reduce the time of the replication process as the piezoceramic rings are made of a different material, i.e.,

ceramics. The final part is the heating element in the conical shape which is connected to the front mass and fixed with a high tensile steel 4340 screw (10 mm length and 2 mm diameter); the heating element is used for the proper distribution of the heat throughout the contact surface of the sonotrode. The Smart Sonotrode device will vibrate in contact with the master microstructure and the polycarbonate at the bottom of the device.

Table 3.1 Material properties of the sonotrode

Property	Stainless steel	Piezoceramic
Young's modulus, E	200 x 10^9 Pa	-----
Poisson's ratio, ν	0.33	0.31
Density, ρ	7850 kg/m^3	7600 kg/m^3
Piezoelectric constant, d_{33}	------	.750
Coupling coefficient, K_{33}	------	585

The main part of the sonotrode device is the front mass and the stack of the piezoceramic rings. The material properties of the sonotrode device are presented in Table 3.1.

3.2. Determination of damping coefficient and impedance analysis for sonotrode

In order to determine the damping coefficient of the sonotrode, the bump test was performed. The damping ratio which was necessary for the numerical model of sonotrode was obtained analytically. Also, the model is 3D since the objective of the numerical frequency response analysis is to determine the frequency at which the operating surface of the sonotrode vibrates with a uniform displacement field. The impedance analysis was performed in order to determine the working regimes, such as the resonant and anti-resonant frequency of the designed sonotrode.

3.2.1 Bump test analysis

The bump test is the measured response of an impact to an object. The damping coefficient was determined by using the bump test system. It consists mainly of a vibrometer and a computer oscilloscope *PicoScope 3424*. The device records in the computer memory the multi-frequency electrical signal and performs spectral analysis (four signals are recorded synchronously). Signals are received from various sensors (vibration, pressure, force, acoustic, etc.). The data is recorded in a computer and presented graphically by using software *PicoScope R5.16.2*. Its specifications are given in Table 3.1.

Table 3. 1 Specifications of Oscilloscope PicoScope 3424

Bandwidth	10 MHz
Channels	4
Vertical resolution	12 bits
Dynamic range	72 dB
Input ranges (full scale)	±20 mV to ±20 V in 10 V steps
Input characteristics	1 MΩ in parallel with 20 pF
Input type	Single-ended, BNC connector
Timebase ranges	500 ns/div to 50 s/div in 25 ranges
Timebase accuracy	100 ppm
Frequency range	DC to 10 MHz
Display modes	Magnitude, peak hold, average
Window types	Blackman, Gaussian, triangular, Hamming, Hann, Blackman-Harris, flat-top, rectangular

The experimental setup for the bump test is presented in Fig. 3.4. It consists of a sonotrode (1), a laser displacement sensor *LK-G82* (produced by *KEYENCE*) (2), an oscilloscope *PicoScope 3424* (3), and a DC supply for the displacement sensor controler (4), a controler *LK-G3001PV* of the displacement sensor (5), and a computer system (6).

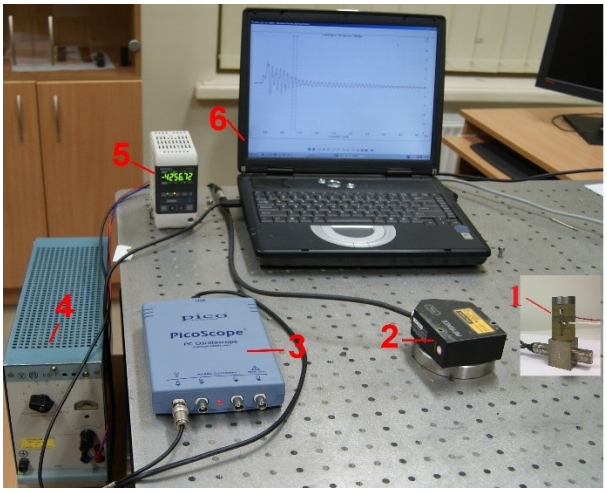

Fig. 3. 4 Experimental setup for the bump test for sonotrode consists of : Sonotrode (1), laser displacement sensor *LK-G82* (*KEYENCE*) (2), oscilloscope *PicoScope 3424* (3), DC supply for the displacement sensor controler (4), controler *LK-G3001PV* of the displacement sensor (5), a computer (6)

The sonotrode (1) is exposed to low mechanical impulses (on the center of the front mass). Excited mechanical vibrations are registered by the laser sensor (2) and transfered to the oscilloscope (3). The signal is then processed by using special software and the PicoScope, and the results are represented on the display of the computer (6) as shown in Fig. 3.5.

Damping measurement requires a dynamic test. A record of the response displacement of an underdamped system can be used in order to determine the damping ratio.

The logarithmic decrement can be calculated with the following formula:

$$\delta = \frac{1}{n} \ln\left(\frac{x(t)}{x(t+nT)}\right), \tag{3.1}$$

where n is any integer number of successive (positive) peaks. Values $x(t)$ and $x(t+nT)$ are two successive peaks.

The damping ratio can be calculated with the following formula:

$$\varsigma = \frac{\delta}{\sqrt{4\pi^2 + \delta^2}}. \tag{3.2}$$

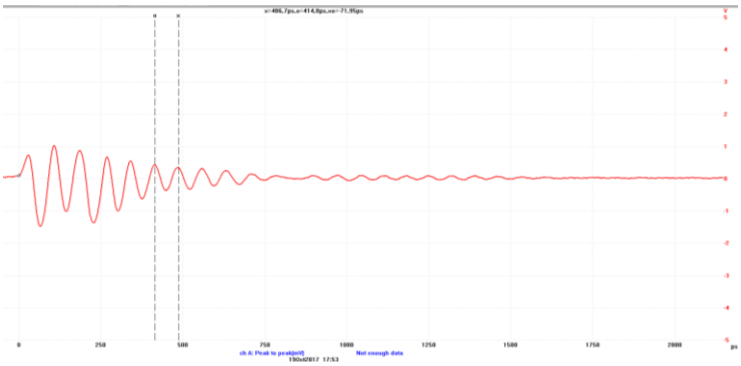

Fig. 3. 5 Transient oscillation of sonotrode

The experimentally obtained response from the Picoscope is presented in Fig. 3.5. Vibration amplitudes $x(t_0)$ and $x(t_n)$ were measured at time intervals t_0 and t_n. The logarithmic decrement δ and damping ratio ζ were calculated by using Equations 3.1 and 3.2. The bump test for the sonotrode was performed five times in total. δ and ζ were calculated with five different n values: 1, 6, 10, 16, 21 in each graph**.** In order to evaluate the resulting noise of the experiment, the average value of the damping ratio was calculated. The results are presented in Table 3.2.

Table 3. 2 Average logarithmic decrements and damping ratios of the devices

Sonotrode device	Average logarithmic decrement	Average damping ratio
Sonotrode	0.12	0.02

3.2.2 Impedance analysis

- **BGI mark – 10 force gauge**

An innovative BGI Universal Force / Torque Gauge (Fig. 3.6) was used to measure the load that was applied to the sonotrode. It is the ultimate device in the force and torque measurement flexibility. With all the features of the BGI mark 10

gauge, coupled with compatibility with a wide selection of interchangeable force and torque sensors, BGI is a versatile solution for many force and torque testing applications.

Fig. 3. 6 BGI universal force / torque gauge

Specifications of the device are presented in Table 3.3.

Table 3. 3 Specifications of BGI mark – 10 force gauge

Accuracy	±0.1% of full scale ±1 digit + sensor
Power	AC or rechargeable battery with Intelligent Power Management System (IPM).
Measuring range	200 lb
Selectable units of measurement	lb, kg, g, N, ozin, lbFin, kgFmm, kgFm, Ncm, Nm (depending on the sensor)
Environmental requirements	40° F – 100°F [5°C – 45°C],
Thermal effects	Zero: 0.03% of full scale/°C, Span: 0.01% of full scale/°C for all remote sensors

- **Impedance analyzer 6500B**

For impedance measurement, 6500B (Fig. 3.7) series of Precision Impedance Analysers provide precise and fast testing of components at frequencies of up to 120 MHz. The basic measurement accuracy is ±0.05%. The accuracy and versatility make precision analyzers the ideal choice for many various tasks and applications including passive component design, dielectric material characterization and manufacturing. High measurement accuracy, capacitance, inductance and impedance basic accuracy is at an excellent level of ±0.05%. The dissipation factor accuracy is ±0.0005, and the quality factor accuracy is ±0.05%. For the graphical sweep of the component, the 6500B series of precision impedance analyzers is highly accurate high frequency component analyzers with a host of useful features. The graphical sweep of two measured parameters is available and displayed on a clear, large color display [132].

The swept parameters are frequency, drive level and DC bias. The available display formats include a series or parallel equivalent circuit. An equivalent circuit

analysis function is available. This allows modeling and curve fitting to various equivalent circuit models.

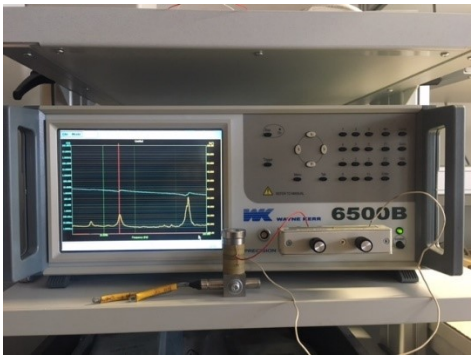

Fig. 3. 7 Impedance analyzer (*6500B*)

Four types of a three-component and a four-component model are available. This instrument will calculate the nearest equivalent circuit parameters the measurement traces and revise the results.

- **Testo 845 IR thermometer**

In order to measure the applied temperature to the sonotrode, a *Testo 545 IR* thermometer (Fig. 3.8) was used. It is a non-contact type infrared thermometer which gives accurate measurements. Surface temperatures with smallest diameters can be measured accurately at short and long distances. The switchable optics for far field and close focus measurement make this possible. Far-field measurements are carried out at an optical resolution of 75:1. In this way, surface temperatures can be measured accurately even at great distances from the object to be measured [133].

Fig. 3. 8 *Testo 545 IR* thermometer

At 1.2 meters from the object to be measured, the measuring spot diameter is only 16 mm. A cross laser marks the measuring spot exactly during the measurement. During measurements at a short distance from the object being measured, the close focus optics has a spot diameter of only 1 mm at 70 mm. Two laser points mark the

spot exactly. Specifications of the temperature measuring instrument are presented in Table 3.4.

Table 3. 4 Specifications of the temperature measuring instrument (*Testo 545 IR* thermometer)

Measuring range	-31.0° to 1742.0 °F / -35 to +950 °C
Accuracy	±4.5 °F (-31.0° to -4.2 °F)
Resolution	0.1 °F / 0.1 °C

In order to know the working regimes of the modeled sonotrode, impedance analysis was performed. For the determination of the working regimes, impedance analysis at different conditions was conducted. Fifteen different experiments with a periodically excited and mechanically-thermally prestressed sonotrode were performed. For the experiment, three different loads (0 kPa, 7.7 kPa and 12.5 kPa) and five heating conditions (0 °C, 80 °C,100 °C, 130 °C and 160 °C) were selected according to the usual thermal replication process of periodic microstructures. From the experiment, resonant and anti-resonant frequencies are identified for the different loads with respect to the temperature applied to the sonotrode.

The experimental setup of the impedance analysis measurement of sonotrode is presented in Fig. 3.9. It consists of a *BGI mark – 10* force gauge (1), a force gauge controler (2), a *6500B* series of precision impedance analyzer (3), the designed sonotrode (4), and a *Testo 845* infrared temperature measuring instrument (5).

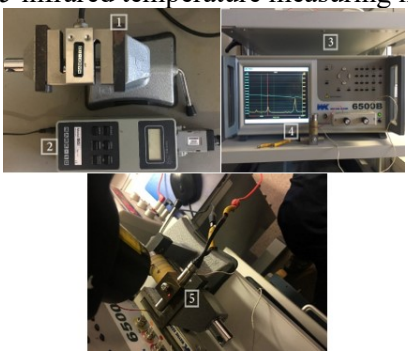

Fig. 3. 9 *BGI mark – 10* force / torque gauge (1) force gauge controler (2), *6500B* series of Precision Impedance Analyzers (3), Sonotrode (4) *Testo 845* Infrared temperature measuring instrument (5)

As impedance is an AC property, it cannot be as easily measured as resistance. Therefore, in this particular case, connecting the sonotrode across the input or output of an amplifier only indicates the DC resistance. It is quite possible, however, to measure the input and output impedance at any frequency by using a signal generator, an oscilloscope (or an AC voltmeter) and a decade resistance box or a variable resistor. For impedance measurement, the sonotrode was connected to a *6500B* series of Precision Impedance Analyzers device by using wires (Fig. 3.9) connected to the piezoceramic rings in order to provide precise and fast testing of the components at frequencies up to 120 MHz which were applied by using a waveform generator and a Liner amplifier. The temperature was measured by using a *Testo 845* – Infrared

temperature measuring instrument. The temperature was applied and regulated with a voltage device in order to reach the 150 °C at a voltage of 16 V. The pressure was measured with a *BGI mark – 10* force / torque gauge which covers a variety of force measurement and torque measurement applications in order to reach 12.5 kPa.

The results of impedance analysis are presented in Fig. 3.10. The presented graph of impedance analysis was obtained from the impedance analyzer for the given boundary conditions of P = 12.5 kPa pressure, and the applied temperature was T = 130 °C.

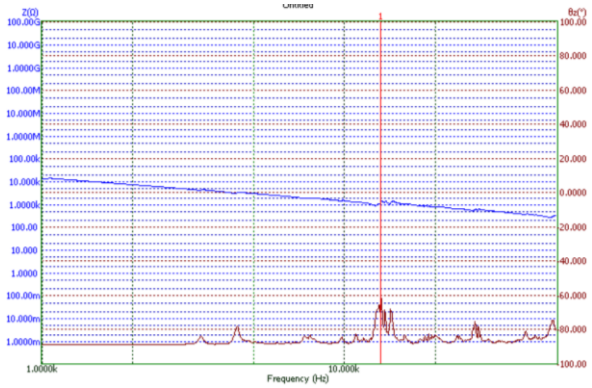

Fig. 3. 10 Impedance (Z) and phase (θ) of the prestressed sonotrode (P = 12.5 kPa, T = 130 °C)

Impedance analysis was performed for the experiment three different loads (0 kPa, 7.7 kPa and 12.5 kPa) and five heating conditions (20 °C, 80 °C, 100 °C, 130 °C and 160 °C). The obtained results are presented in Table 3.5.

Table 3. 5 Impedance analysis of the sonotrode

No.	Load / pressure, kPa	Temperature, °C	Resonant frequency, kHz	Anti-resonant frequency, kHz
1	0	20	15.140339	15.55116
2	0	80	12.028077	12.26610
3	0	100	11.309563	11.79485
4	0	130	10.538630	10.85286
5	0	160	10.487158	10.33421
6	7.70	20	13.863118	13.22421
7	7.70	80	12.508555	12.44751
8	7.70	100	12.326167	12.32621
9	7.70	130	11.852694	11.50961
10	7.70	160	11.852694	10.33421
11	12.5	20	14.068249	14.26812
12	12.5	80	13.863110	13.66523
13	12.5	100	13.136233	13.26165
14	12.5	130	12.881460	12.52521
15	12.5	160	12.693642	12.11614

From Table 3.5, it can be observed that the resonant frequency of the sonotrode varies from 15.1 kHz to 10.5 kHz depending on the working conditions, while the anti-resonance frequency varies from 15.5 kHz to 10.3 kHz. From the analysis, it is obvious that the resonant and anti-resonant frequency has direct dependence on the load, i.e., a higher load induces a higher frequency. Simultaneously, a higher imprint temperature leads to lower resonant and anti-resonant frequencies. It could be explained by the lower module of elasticity at a higher temperature.

3.3. Temperature distribution of the sonotrode

The sonotrode device was used to achieve high quality mechanical hot imprinting on the polycarbonate material. The temperature plays an important role to print good quality replicas. The temperature distribution test is done because it is necessary to know the thermal distribution of temperature over all the parts of the sonotrode. By applying a broad range of temperatures on the sonotrode, we should know the exact temperature distribution on the surface of the sonotrode for identifying the influence of temperature in order to increase the quality of the imprint process. Therefore, a thermal imaging camera was used to identify temperature distribution on the surface of the sonotrode

To investigate the thermal Temperature distribution on the surface of the sonotrode FLIR T450SC (Fig. 3.11) was measured and analysed using thermal imaging camera.

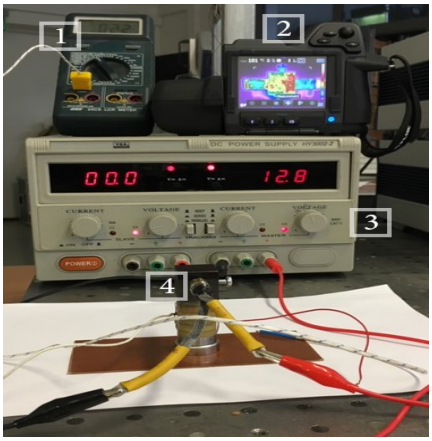

Fig. 3. 11 Experimental setup of temperature distribution: Thermometer (1), *FLIR T450SC* thermal imaging cameras (2), Power supply (3), Sonotrode (4)

The experimental setup of the temperature distribution test consists of a multi-meter measuring the temperature (thus it will act as a thermometer), a *FLIR T450SC* thermal imaging camera for capturing the image to analyze the thermal distribution of the temperature over the entire surface of the sonotrode, DC power supply which is directly connected with the sonotrode for applying heat, and the sonotrode. The experimental setup is presented in Fig. 3.11.

The *FLIR T450SC* thermal camera (as shown in Fig. 3.12) features a tiltable IR unit which gives great flexibility and allows to conduct experiments fast and in a

comfortable position. An un-cooled Vanadium Oxide (VoX) microbolometer detector produces thermal images of 320 x 240 pixels. The generated crisp and clear detailed images are easy to interpret, which results in reliable imaging with high accuracy. The device is equipped with a 3.1MP visual camera. A 3.5" (320 × 240) LCD touch screen keeps onscreen temperature data upright in portrait or landscape modes.

Fig. 3. 12 *FLIR T450SC* thermal camera

The experimental results of thermal distribution are presented in Fig. 3.13. When the heating element is connected to a DC voltage of 12.7 V and the temperature reaches 150 °C, we can observe that the heating element functions well, and the heat is distributed on the bottom part of the front mass.

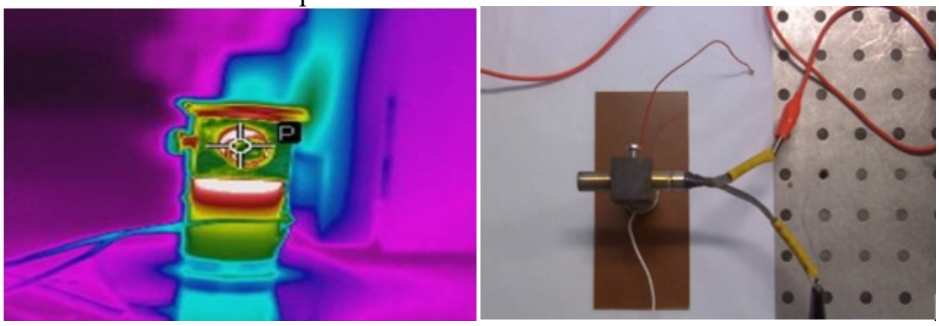

Fig. 3. 13 Experiment results with *FLIR T450 SC* thermal imaging cameras for the designed sonotrode when the temperature is 150 °C

During the thermal analysis of the sonotrode, a variety of temperatures (100 °C, 125 °C, 130 °C, and 150 °C) was tested; however, it was found that a temperature of 150 °C resulted in equal distribution across the whole surface of the front mass which is required for hot imprinting of microstructure to the polycarbonate material.

3.4. Finite element analysis of the sonotrode

Finite element analysis was performed in order to determine the behavior of the designed sonotrode and the operational frequency of the device. According to the design, the model was prepared by using *COMSOL Multiphysics 5.4* software. Also, in order to exploit all the potential of the designed sonotrode, it is necessary to obtain the highest displacements at the vibration frequency. This is only possible when the sonotrode works at the first resonant frequency. In order to determine the resonant

frequency, numerical simulations must be performed. The prepared model of the sonotrode in *COMSOL Multiphysics* is presented in Fig. 3.14.

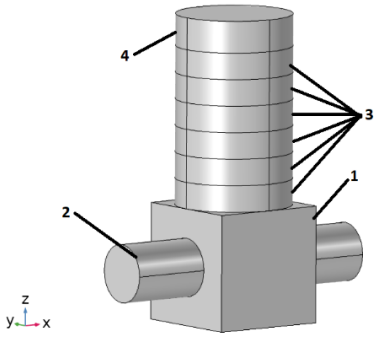

Fig. 3. 14 Numerical model of sonotrode design in *COMSOL 5.4*. consists of Front mass (1), Heating element (2), Six PZT 5H rings (3), and Top stainless steel ring (4)

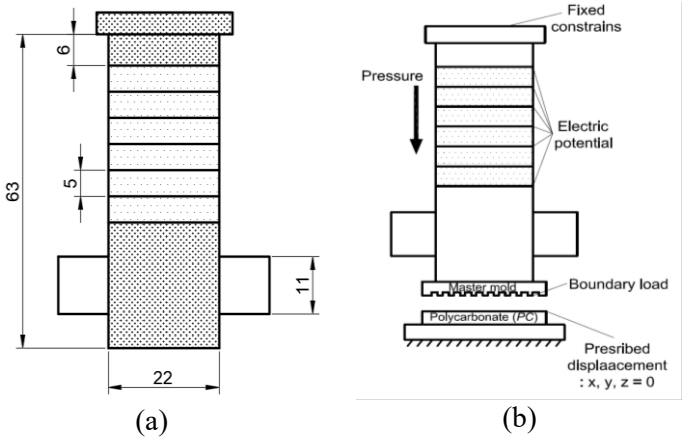

Fig. 3. 15 Computational schemes with boundary conditions of the sonotrode: Dimensions (a) and boundary conditions (b)

The sonotrode can be described with the following geometric parameters: the height of the piezoceramic ring stake is 30 mm; the height and the width of the front mass is 22 x 22 mm, and the diameter and the height of structural ring is 22 mm and 6 mm, respectively. The heating element is made of structural steel, and the diameter of the heating element is 11 mm, and its length is 52 mm. It is inserted in the front mass. The top of the device is immovably fixed in horizontal directions of the global coordinate axis. The actuation voltage between the top and the bottom of *PZT-5* varies from 5 V to 200 V. Structural steel and *PZT-5* are used for the metallic part of the sonotrode device and the piezoceramic material.

An unstructured tetrahedral mesh is used for all the parts of the sonotrode. Piezoelectric devices physics interface is used for a computational simulation which combines solid mechanics and electrostatics together with the constitutive relationships required to model piezoelectric effects. In this simulation, inverse

piezoelectric effects are modeled, and piezoelectric coupling is formulated by using a stress-charge form. Consecutive equations of the material parameters of the piezoelectric constituents of the relevant devices are selected as a stress-charge form for the constitutive equation.

The material parameters for piezoelectric materials (*PZT-5*) are characterized by the elasticity matrix– c_e, the coupling matrix– e and the relative permittivity matrix– ε_{rs}. The polarization of piezoceramic elements is considered in y direction, i.e., corresponding to the real conditions.

The elasticity matrix characterizes the stress applied to the material and its strain response. The stress-strain relationship throughout the elasticity matrix is expressed as follows:

$$\sigma = c_e \varepsilon \,, \tag{3.3}$$

here: σ – stress, ε – strain, and c_e – the elasticity matrix.

The elasticity matrix of PZT-5 has the following expression:

$$c_E = \begin{bmatrix} 1.20346e11 & 7.51791e10 & 7.50901e10 & 0 & 0 & 0 \\ 7.51791e10 & 1.20346e10 & 7.50901e10 & 0 & 0 & 0 \\ 7.50901e10 & 7.50901e10 & 1.10867e11 & 0 & 0 & 0 \\ 0 & 0 & 0 & 2.10526e10 & 0 & 0 \\ 0 & 0 & 0 & 0 & 2.10526e10 & 0 \\ 0 & 0 & 0 & 0 & 0 & 2.25734e10 \end{bmatrix}$$

The coupling matrix. The piezocoupling matrix, denoted by e, is applied in the stress-charge relationship:

$$\sigma = c_E \varepsilon - e^T E \,, \tag{3.4}$$

here: σ – stress, ε – strain and E – the electric field.
The coupling matrix of *PZT-5* is expressed as:

$$e = \begin{bmatrix} 0 & 0 & 0 & 0 & 12.2947 & 0 \\ 0 & 0 & 0 & 12.2947 & 0 & 0 \\ -5.35116 & -5.35116 & 15.7835 & 0 & 0 & 0 \end{bmatrix}$$

The relative permittivity matrix ε_{rS} is applied in the constitutive relation of stress-charge and strain-charge forms:

$$D = e\varepsilon + \varepsilon_0 \varepsilon_{rS} E \,, \tag{3.5}$$

The relative permittivity matrix of *PZT-5* can be represented with:

$$\varepsilon_{rS} = \begin{vmatrix} 919.1 & 0 & 0 \\ 0 & 919.1 & 0 \\ 0 & 0 & 826.6 \end{vmatrix}$$

The piezoelectric equations are written in the forms of nodal displacement $\{U\}$ and nodal electrical potential $\{\phi\}$. Force F for unstressed devices is equal to zero, and the nodal electric loads are expressed as $\{Q\}$:

$$\begin{bmatrix} [M_{UU}] & 0 \\ 0 & 0 \end{bmatrix} \begin{Bmatrix} \{\ddot{U}\} \\ \{\ddot{\phi}\} \end{Bmatrix} + \begin{bmatrix} [C_{UU}] & 0 \\ 0 & 0 \end{bmatrix} \begin{Bmatrix} \{\dot{U}\} \\ \{\dot{\phi}\} \end{Bmatrix} + \begin{bmatrix} [K_{uu}] & [K_{u\phi}] \\ [K_{u\phi}] & [K_{\phi\phi}] \end{bmatrix} \begin{Bmatrix} \{U\} \\ \{\phi\} \end{Bmatrix} = \begin{Bmatrix} \{0\} \\ \{Q\} \end{Bmatrix}, \quad (3.6)$$

$$[K_{UU}] = \iiint_{\Omega e} [B_U]^T [c][B_U] dV, \quad (3.7)$$

$$[K_{U\phi}] = \iiint_{\Omega e} [B_U]^T [e][B_U] dV, \quad (3.8)$$

$$[K_{\phi\phi}] = \iiint_{\Omega e} [B_\phi]^T [\varepsilon][B_\phi] dV, \quad (3.9)$$

$$[M_{UU}] = \rho \iiint_{\Omega e} [N_U]^T [N_U] dV, \quad (3.10)$$

$$[C_{UU}] = \beta [K_{UU}], \quad (3.11)$$

here: $[K_{UU}]$ – mechanical stiffness matrix, $[K_{U\phi}]$ – piezoelectric coupling matrix, $[K_{\phi\phi}]$ – dielectric stiffness matrix, $[M_{UU}]$ – mass matrix, ρ – piezoelectric density, $[N_U]$ – matrix of elemental shape functions, $[C_{UU}]$ – mechanical damping matrix, $[B_U]$ and $[B_\phi]$ – derivatives of FE model shape functions, $[c]$ – elastic coefficients, $[e]$ – piezoelectric coefficients, $[\varepsilon]$ – dielectric coefficients, β – damping coefficient. VAP is excited with a harmonic voltage signal, and the electrical potential is expressed as follows:

$$Q = A \sin \omega, \quad (3.12)$$

here: A – amplitude, and ω – angular frequency.

The simulated dynamic behavior of the sonotrode is provided in terms of point displacement. The frequency response problem for the unstressed device is solved to obtain the following vibration responses:

$$\begin{bmatrix} K_{UU} - \varpi C_{UU} - \varpi^2 M_{UU} & K_{U\phi} \\ K_{\phi U} & K_{\phi\phi} \end{bmatrix} \begin{Bmatrix} \{U\} \\ \{\phi\} \end{Bmatrix} = \begin{Bmatrix} \{0\} \\ \{Q\} \end{Bmatrix}, \quad (3.13)$$

The displacement of a pre-stressed device corresponding to the applied pressure is determined according to the formula:

$$[K_{UU}]\{U\} = \{F\}, \quad (3.14)$$

Consequently, pre-stressed frequency response analysis is performed by modifying Equation (3.13), i.e., displacement is added:

$$\begin{bmatrix} K_{UU} - \varpi C_{UU} - \varpi^2 M_{UU} & K_{U\phi} \\ K_{\phi U} & K_{\phi\phi} \end{bmatrix} \begin{Bmatrix} \{U\} \\ \{\phi\} \end{Bmatrix} = \begin{Bmatrix} \{F(U_0)\} \\ \{Q\} \end{Bmatrix}, \tag{3.15}$$

The finite element model of the sonotrode device simulated to achieve the deformed shape and the displacement of the sonotrode are presented in Fig. 3.16.

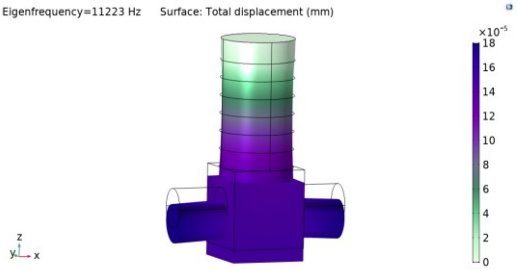

Fig. 3. 16 Result of the numerical simulation of the sonotrode at Frequency 11.223 kHz

The achieved deformed shape and the displacement of the numerical results at a frequency of 11.223 kHz is shown in Fig. 3.16. The displacement of the sonotrode is aligned to *z* axis. This means that the model is in agreement with the required movement for the hot imprinting process. The sonotrode is moved in upward and downward directions at a frequency of 11.223 kHz.

The FE model determined the operating frequency; after that, Z-directional numerical frequency response curves of the bottom edge four points of the sonotrode device (Fig. 3.16) are obtained.

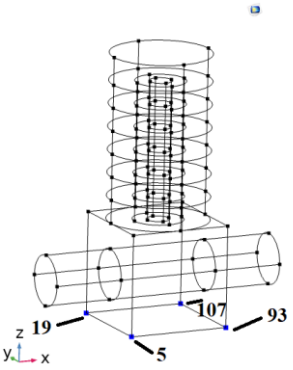

Fig. 3. 17 Points analysed during numerical frequency response analysis of the sonotrode device

The numerically simulated frequency response curves registered at points 5, 19, 93 and 107 and the displacement field of sonotrode are provided in Fig. 3.18. The focus is to detect the frequency, at which, the peaks of the frequency response curves

coincide. Mutual peaks indicate uniform displacement throughout the analyzed points.

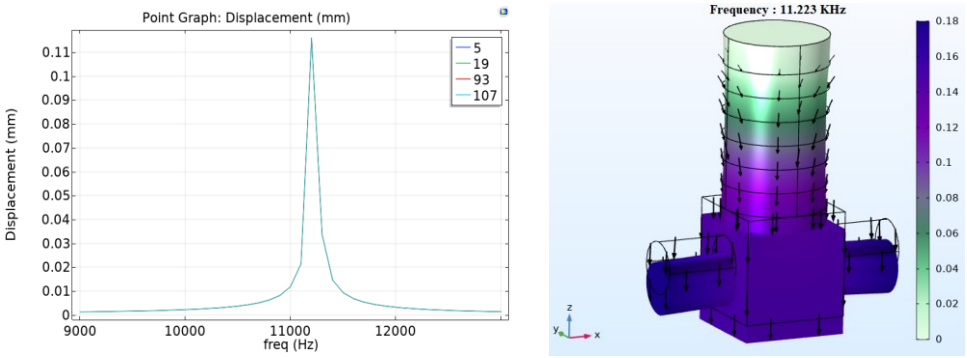

(a) **(b)**

Fig. 3. 18 Numerically simulated frequency response curves (a) and the visualization of the simulated displacement field (b) of the sonotrode device

The frequency response plot in Fig. 3.18 (a) indicates that the sonotrode vibrates with uniform amplitudes throughout the operating surface at the excitation frequency of 11.3 kHz. The displacement values at the analyzed points are 0.18 mm. The visualization of the displacement field (Fig. 3.18. (b)) confirms the uniformity of amplitudes, i.e., the operating surface is of a homogenous color.

From the simulation, the operational frequency of the sonotrode analyzed for the further experiment and the operational frequency for the displacement of the sonotrode in the normal downward direction was detected.

3.5. Experiments of microstructure replication

Experiments of microstructure replication assisted by high-frequency vibratory excitation are presented in this part of the chapter. The aim is to determine the relationship between the process parameters (Temperature, pressure, and the time of the process) and the quality of the replicated microstructure. The establishment of these relationships enables to improve the process results in the form of the quality of the replicas.

3.5.1 UHE of periodic microstructure

The replication of periodic microstructures is performed after determining sets of the appropriate process parameters. The aim of this experiment is to determine how the diffraction efficiency of the embossed DOE depends on the additional heat generation through pre-structured foils.

A nickel master microstructure (Fig. 3.19) is applied in the UHE process. The nominal dimensions of the master microstructure are as follows: a period of 4 μm, and a depth of 603.7 nm. A theoretically ideal microstructure is modeled with *GSolver*

software in order to identify the target value of RDE. The modeling revealed that the theoretically ideal RDE of +1 and –1 maxima is 38.95%.

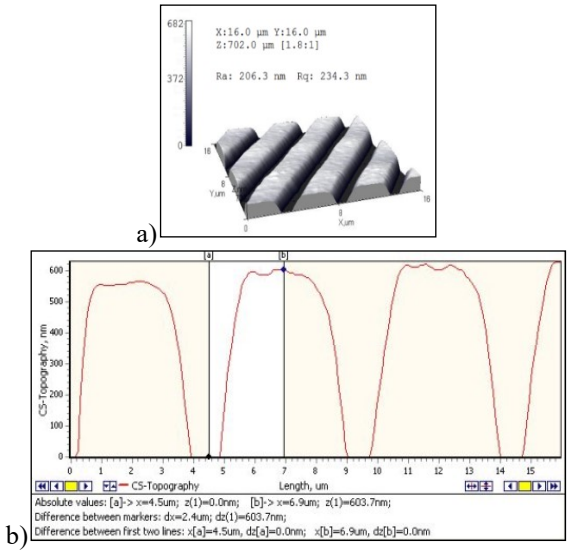

Fig. 3. 19 AFM image of the master microstructure: 3D (a) and profile view (b)

3.5.2 Experiment with thermal imprinting process

The thermal imprinting experimental setup (Fig. 3.20) was used for the printing microstructure on the polycarbonate material. Then, the printed specimens ware analyzed as to how the quality of the replicated microstructures is influenced by the following parameters: the magnitude of lateral vibration amplitudes, the temperature, the imprinting pressure, and the duration of imprinting.

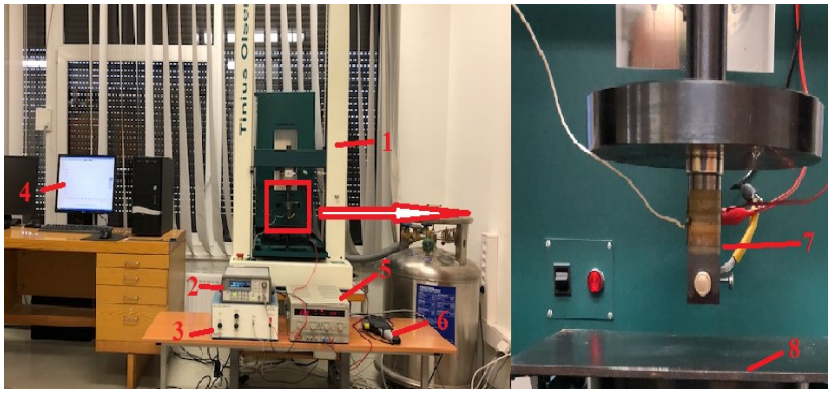

Fig. 3. 20 The experimental setup of mechanical hot imprinting with high excitation frequency consists of : *Tinius Olsen* automatic pressing machine (1), Wave form generator (2), Power Supply (3), Computer system for operating the pressing machine (4), DC voltage generator (5), Temperature measurement instrument (*Testo 845* – Infrared temperature measuring instrument) (6), Vertically fixed sonotrode (7), Fixed base for specimen hot imprinting (8)

The experimental setup of mechanical hot imprinting with high excitation vibration frequency consists of a *Tinius Olsen* pressing machine for the constant and automatic operating system which helps to provide equal distribution of the applied load for hot imprinting. The sonotrode with a stack of *PZT-5H* rings heats up the microstructure at a desired temperature of printing and produces high frequency vibration for the superior quality of the printing process. A wave form generator and power supply are used to generate high frequency vibration in the multi-stack sonotrode. A voltage generator is used to apply direct current to the conical heating element which is fixed at the bottom front mass for the generation of higher temperature for imprinting. A computer software system is used to operate the automatic compression machine to set such parameters as the pressure, auto reverse after a certain period, etc. A non-contact type temperature measuring *Testo 845* – Infrared temperature measuring instrument is used to measure the temperature of the surface of the bottom side of the front mass.

As it was discussed in Chapter 2.1, in order to obtain replicas of top quality, it is not enough to apply the available devices and achieve optimization. High frequency vibrations are among the measures which could be used in order to optimize the mechanical hot imprint process.

The process of hot imprinting consists of the following steps:

In the preheating stage, the temperature of the front mass and the heating element is 20 °C (the ambient temperature). Then, we preheat the front mass in the range of 100–150 °C with the help of the DC power supply and wait until the desired temperature is reached. The temperature is measured with a thermometer which confirms the desired temperature. In order to know the effect of the different temperature effects on the quality of the replica, the selected range was from 100 to 150 ºC. Since 150 °C temperature is the temperature that corresponds to the glass transition temperature of the polycarbonate, the polymer leaves its glassy or brittle state and starts to be reversibly or irreversibly deformed under the action mechanical stress. In other words, it becomes viscoelastic. Imprinting of the microstructure on the polycarbonate material is performed with the help of a computer system which is used to operate the pressing machine and to apply the force of 1000–5000N for the imprint of microstructure on polycarbonate.

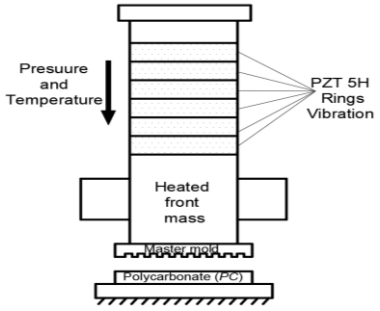

Fig. 3. 21 Structural scheme of the hot imprint process with ultrasonic excitation (pressure, temperature, sinusoidal force (Vibrations))

The microstructure was placed on the bottom side (Fig. 3.21) of the heated front mass. The polycarbonate material was placed on the fixed base of the pressing machine. Then, the hot printing process was initiated. The selected pressure was applied for time period of 2–10 sec to understand the influence of the duration of the process on the quality of the replicas. The polycarbonate material comes in contact with the heated front mass and the microstructure, and plastic deformation of the polycarbonate takes place. When the heated front mass touches the polycarbonate, the time starts to count, and, according to the parameters for the time duration, the vibration frequency of 11.3 kHz is applied for a 2 second-period, and then, the load was taken off from the polycarbonate (as discussed in Chapter 2).

The experiments apply high-frequency vibratory excitations with the sine waveform. The time acceleration function of vibratory excitation with sine waves is expressed as follows:

$$a(t) = -a\omega^2 \sin \omega t \,, \tag{3.16}$$

The experimental matrix of thermal imprint experiments is composed, and the data is outlined in Table. 3.6.

Table 3. 6 Experimental matrix of the process of mechanical hot imprint with usage of high frequency excitation

Sonotrode	Without vibrational excitation	With vibrational excitation
Impressing time *t*, s	2,5,10	2,5,10
Force, N	1000, 2000, 3000, 4000, 5000	1000, 2000, 3000, 4000, 5000
Vibration frequency *f*, kHz	0	11.3
Temperature *T*, ˚C	100, 125, 150	100, 125, 150

3.5.3 Quality Evaluation of the replicas

- **Diffraction efficiency measurement**

The nature of replicas was assessed by using aberrant optical technique estimation of diffraction efficiency. Periodical microstructures are made from optic materials; therefore, optical assessment methods are utilized for quality examination.

The diffraction efficiency of grating created by the hot imprint process on the surface of the polycarbonate is one of the parameters which determines the quality of the microstructure. Gratings are created by using the hot imprint process with and without high frequency excitation, and, during quality investigation, diffraction efficiencies were measured on purpose to find the microstructure of the best possible optical quality, as well as to determine whether high frequency excitation and other process parameters during the process affect this parameter. The process parameters include temperature, excitation frequency, the force of mechanical load and the duration of the hot imprint process as the purpose is to determine the collection of

parameters which influence the diffraction efficiency most positively. The principle of the distributed diffraction efficiencies is presented in Fig. 3.22.

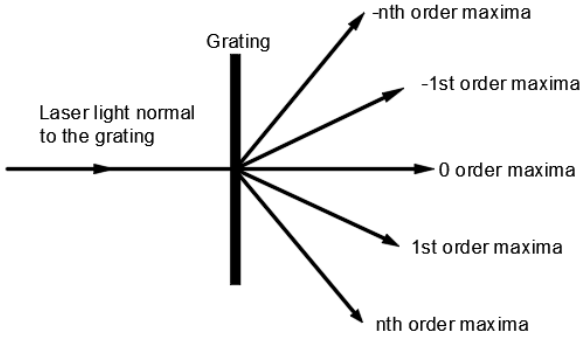

Fig. 3. 22 Principle of the grating distribution of the maxima

Laser diffractometer (Fig. 3.23) is constructed for measuring diffraction efficiency. Analysis of diffraction efficiency is initiated by illuminating the sample with laser light which diffracts as it passes through the sample. The intensity values of the diffracted maxima are registered with a photodiode which is connected to the ammeter. The electric current, which is registered by an ammeter, is directly proportional to the light intensity. RDE is calculated by applying the following equations:

$$RE_{i,j} = \frac{I_{i,j}}{I_j} \quad , \tag{3.17}$$

$$I_j = \sum_i I_{i,j} \quad , \tag{3.18}$$

here: $RE_{i,j}$ – RDE, $I_{i,j}$ – the light intensity of the maxima and I_j – the sum of the light intensities.

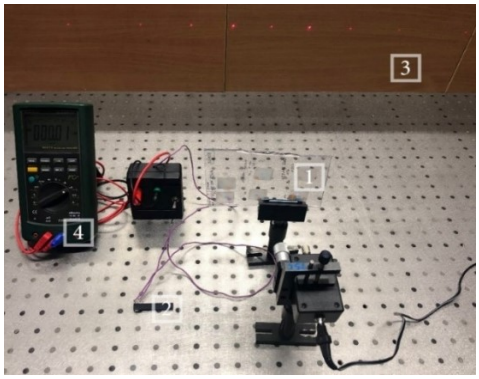

Fig. 3. 23 Measurement of diffraction efficiency: sample (1) photodiode connected to ampermeter (2), distribution of diffraction maxima (3), ammeter (4)

The laser beam is coordinated to the microstructure. As the beam goes through the microstructure, it is being diffracted into a specific measure of the maxima which reaches the photodiode. The electric flow which goes through the photodiode is registered with an ammeter. The electric flow which goes through the photodiode relies upon lighting; in this way, no extra figurines are required to interpret the outcomes. Diffraction maximas are dissipated, thus they are estimated by changing the situation of the photodiode so that the desired maxima would go through the photodiode.

- **Optical microscope image**

An optical microscope *NICON Eclipse LV 150* (Fig. 2.24) with a CCD camera was used for investigations. A microscope can magnify the view by 5x, 10x, 20x. Other parameters are as follows: the distance between the oculars 47 mm – 82 mm, a rotational angle of 360°, mobility in *X* and *Y* axis, an observation field of 20 mm × 20 mm, illumination with a halogen lamp (12 V, 50 W), a resolution of 2 megapixels, color sensor resolution of 1600x1200, a dynamic range of >60dB, power 2.5 W, integration time 84 μs – 3 s.

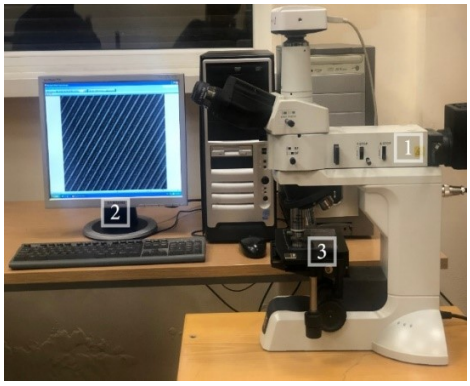

Fig. 3. 24 Optical microscope: Optical microscope connected to PC (1), PC for reading (2), Specimen (3)

3.6. Results

The RDE of the samples is measured, and the quality of the replicated microstructures is investigated in terms of mean RDE in +1 and –1 maxima. Subsequently, the images obtained during the microscope evaluation also represent the quality of the printed microstructure. The results of the relative diffraction efficiency of the replica produced with and without vibrational excitation at an applied load of 1000 – 5000 N, 10 sec duration of the printing and 150 ºC temperature with 11.3 kHz and without vibrational excitation are presented in Fig. 3.25.

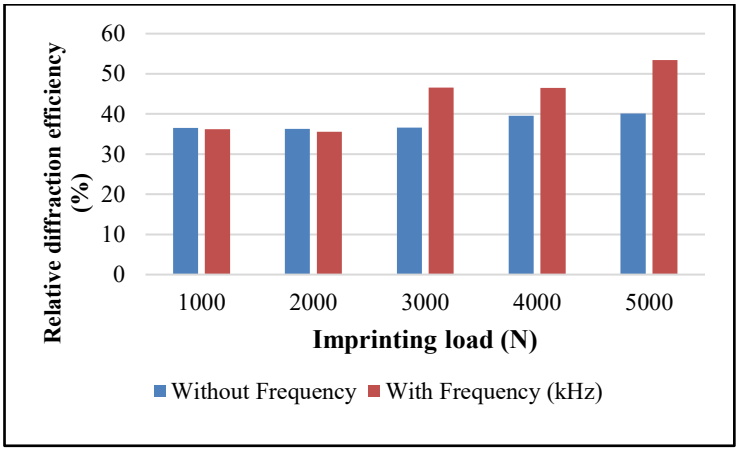

Fig. 3. 25 Relative diffraction efficiencies of replicas produced with and without vibrational excitation at 150 ºC and time duration 10 sec

The measurement of diffraction maxima results (Fig. 3.26) was performed for the time of printing of 10 sec without frequency, and with vibrational excitation when the total time was 12 sec.

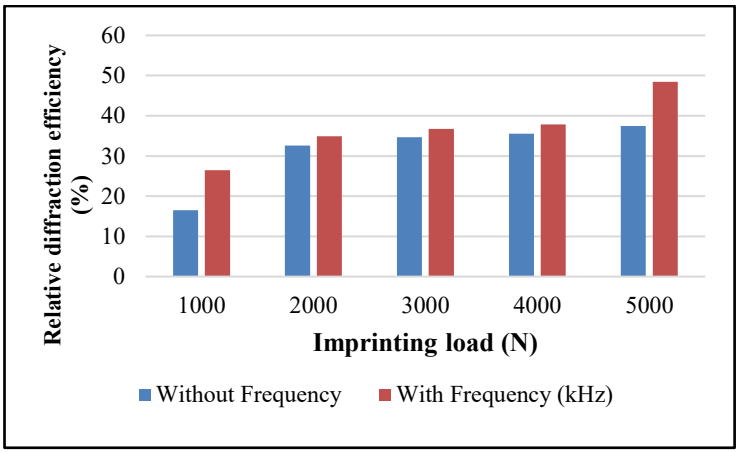

Fig. 3. 26 Relative diffraction efficiencies of replicas produced with and without vibrational excitation at 125 ºC and time duration 10 sec

From the achieved results, it is clearly evident that, at a 5000 N load and the time of the process set at 10 sec without and with frequency, RDE is 40.12% and 53.42%, respectively. When the applied load decreases to 4000 N, the achieved values are 39.52% and 46.52% without and with vibrational excitation, respectively. Simultaneously, when the load decreases, the diffraction efficiency also decreases. It means that the quality of the replica is directly proportional to the applied load, time the duration of the printing, and the applied vibrational excitation. From the achieved results, it is clear that, with higher load, temperature, and imprinting time with vibratory excitation, high quality imprinting is produced. Also, it is clear that the RDE

of printed microstructures is better than the previously used hot imprinting techniques developed by Šakalys (2014) [53] and Narijauskaitė (2013) [131].

When hot imprinting was performed at a temperature of 125 ºC, and the duration of the printing was maintained the same as the previous value of 10 sec, the obtained values of the relative diffraction efficiency were 48.43% and 37.48% with and without vibrational excitation. It means that a 33.65% higher value was obtained by applying vibratory excitation. Meanwhile, 35.54% and 37.83% RDE was observed when the applied load was 4000 N without and with vibrational excitation. A decrement in the RDE of the printed replica was observed when the applied load for the imprinting was being decreased gradually.

Figure 3.27 demonstrates a decrease in the mean RDE when the temperature of the imprinting is 100 ºC. The highest obtained values of the RDE are 6.37% and 13.39% without and with vibratory excitation. Also, non-uniform distribution of the maxima is observed at 100 °C because the temperature is not sufficient for the printing. This correlation is less obvious when the process temperature is 150 °C. The application of the sine waveform increases the mean RDE by 6 times.

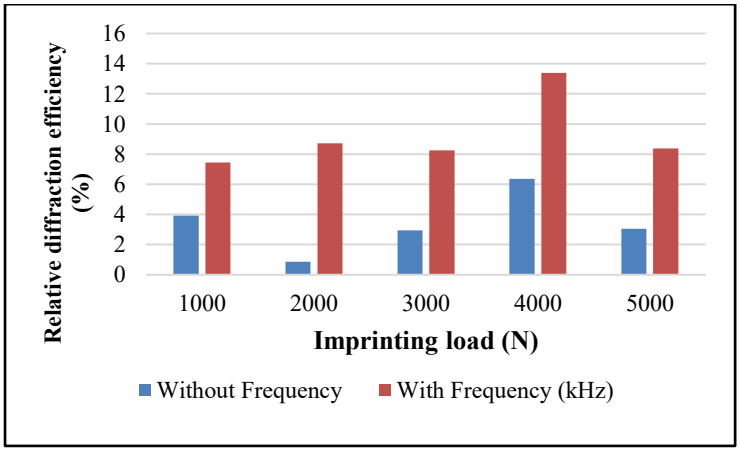

Fig. 3. 27 Relative diffraction efficiencies of replicas produced with and without vibrational excitation at 100 ºC and time duration 10 sec

Figure 3.28 demonstrates the RDE when the imprinting temperature is 150 ºC and the duration of the imprinting is 5 sec with and without vibratory excitation. The obtained result shows 43.12% and 38.41% RDE observed when the applied load was 5000 N. The lowest observed RDE when the applied load was 1000 N reached 28.23% and 33.10% without and with vibratory excitation. On the other hand, an increase in the imprinting load leads to the results being increased in the RDE of the printed replicas.

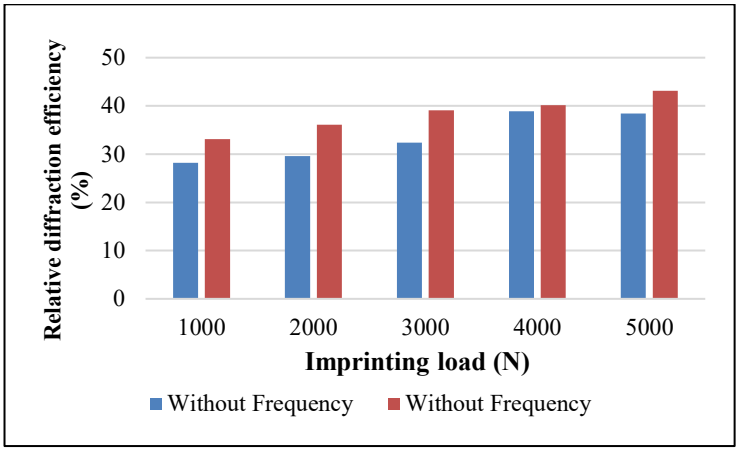

Fig. 3. 28 Relative diffraction efficiencies of replicas produced with and without vibrational excitation at 150 ºC and time duration 5 sec

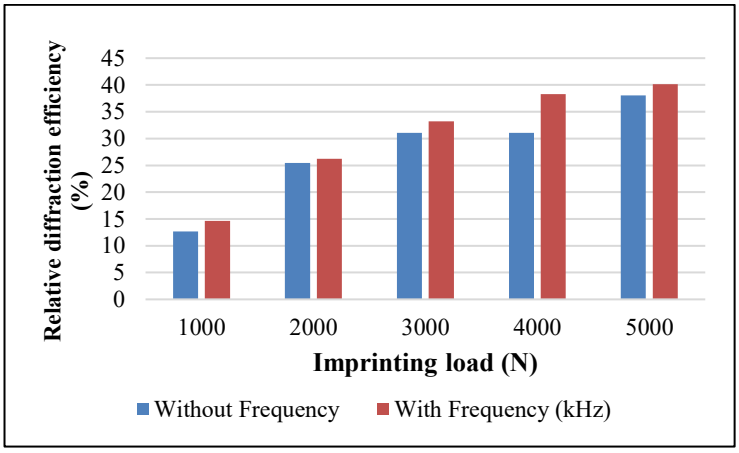

Fig. 3. 29 Relative diffraction efficiencies of replicas produced with and without vibrational excitation at 125 ºC and time duration 5 sec

Figure 3.29 represents the RDE of the replica obtained at 125 °C when the duration of the imprinting was 5 sec. The obtained RDE for a 5000 N load was 40.12% and 38.08% with and without vibratory excitation. It shows that the application of vibratory excitation increases the RDE by about 7% more than without vibratory excitation. The obtained correlations demonstrate that an increase in the applied load and the imprint temperature enhances the mean RDE of the replicated microstructures.

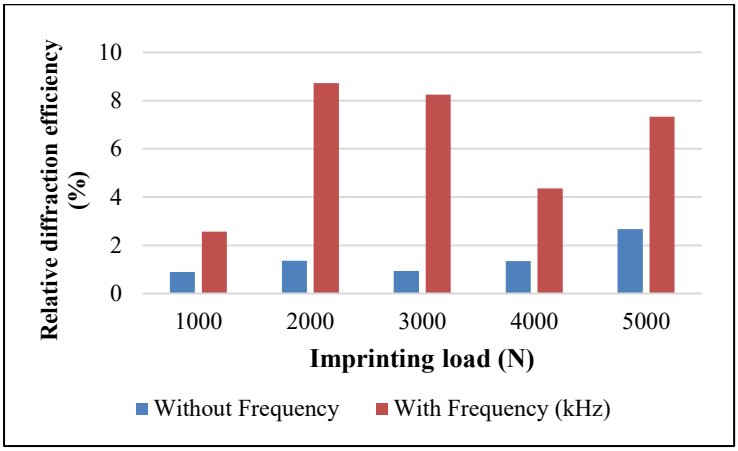

Fig. 3. 30 Relative diffraction efficiencies of the replicas produced with and without vibrational excitation at 100 ºC and time duration 5 sec

The RDE of the replica produced at 100 °C and 5 s duration of imprinting (Fig. 3.30) demonstrates a poor quality of the replica. The RDE at the highest load 5000 N is 7.33% and 2.67% with and without vibratory excitation, respectively. The obtained results at the highest load are 5 times lower than the results obtained at the same time duration and a temperature of printing of 125 °C.

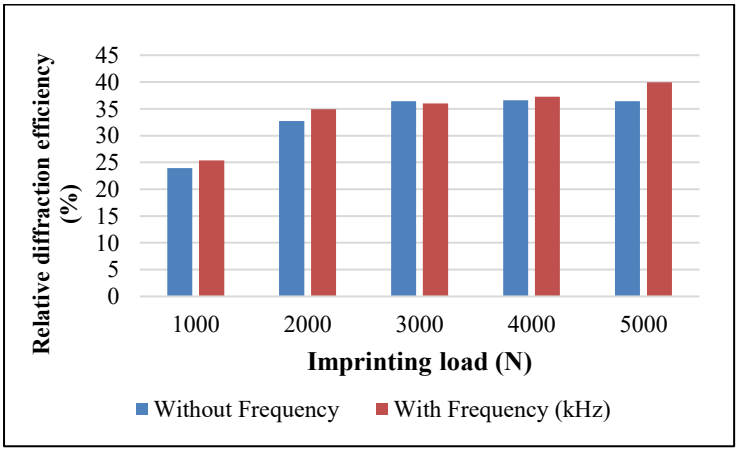

Fig. 3. 31 Relative diffraction efficiencies of replicas produced with and without vibrational excitation at 150 ºC and time duration 2 5ec.

Figure 3.31 demonstrates the RDE of the printed replica at a temperature of 150 °C and 2 sec duration of the imprinting. The obtained results show that a higher load with vibratory excitation secures a higher RDE for the printed replica at 39.93% and 36.40% with and without vibratory excitation, respectively. On the other hand, a gradual load decrement results in the decrement of the RDE of the replicas.

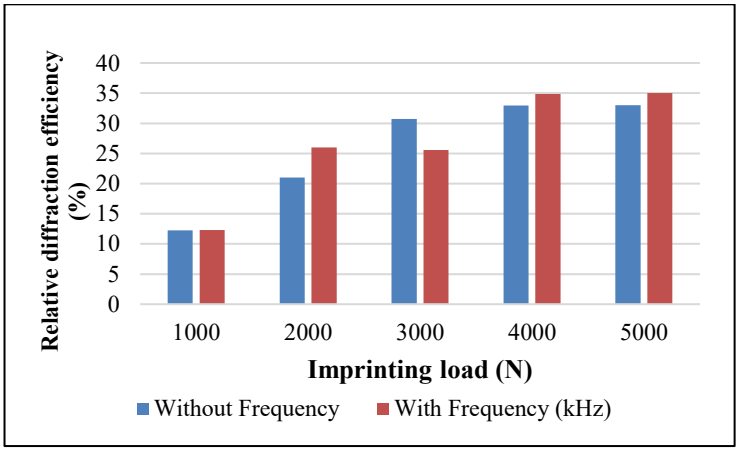

Fig. 3. 32 Relative diffraction efficiencies of replicas produced with and without vibrational excitation at 125 °C and time duration 2 sec

The relative diffraction efficiency measured for the replica produced at 125 °C and 2 sec time duration (Fig. 3.32) demonstrates a higher RDE of 35% at 5000 N and the lowest RDE of 16.30% at 1000 N load with vibratory excitation. On the other hand, while there is no change observed when a 3000 N load with vibratory excitation is applied for the replica. It shows that 25.55% and 30.72% RDE is observed with and without vibratory excitation. It could be possible because of the imprinting duration and the applied load.

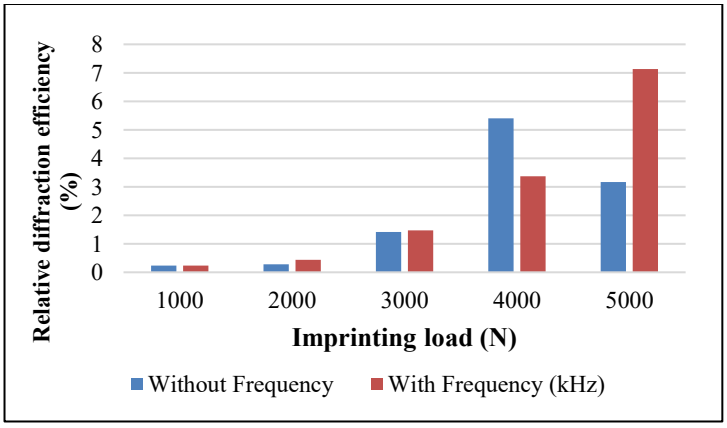

Fig. 3. 33 Relative diffraction efficiencies of replicas produced with and without vibrational excitation at 100 °C and time duration 2 sec.

Figure 3.33 demonstrates the results of the replica produced at 100 °C and 2 sec time of imprinting with and without vibratory excitation. From the obtained results, the highest RDE was observed for the loads of 1000 to 5000 N when the replica was produced with vibratory excitation. The results show that 7.13% was the highest RDE to be observed when a replica was produced with vibratory excitation at 5000 N. On the other hand, a defect appeared when a 4000 N load was applied with vibratory

excitation. The occurrence of the disturbance shows that the time of imprinting and the applied load has direct relationship with the quality of the replicas.

Mechanical hot imprint experiments were performed with a periodical nickel microstructure whose period is 4μm. Images of the original periodical microstructure were obtained with a microscope; they are presented in Fig. 3.34. The experiments were conducted at five different loading conditions with and without vibration excitation (frequency 11.3 kHz) at temperatures of 100, 125, and 150 °C, and a time of imprinting being set at 2, 5, and 10 sec. After many experiments carried out while changing the temperature, time, and the loading of the sonotrode, it was determined that these process parameters exerted the most significant influence. It is obvious that the quality of the replica is better when vibration excitation is turned on.

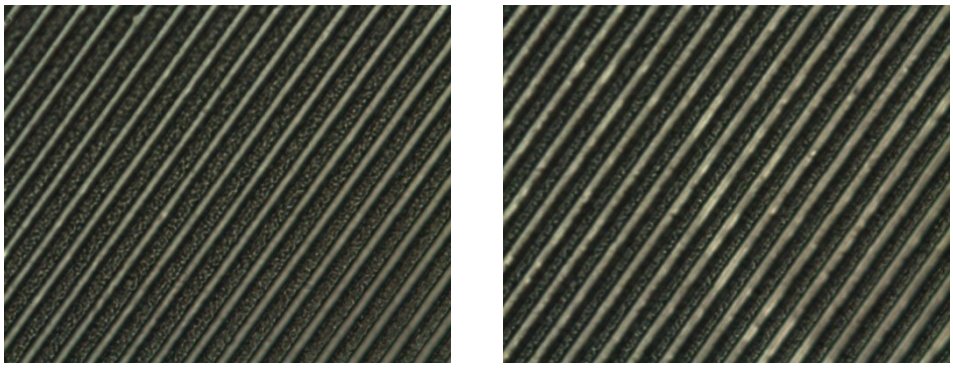

a **b**

Fig. 3. 34 Photos of replicas (T=150 °C, P=5000 N and time 10 sec) without excitation (a) and with vibration excitation (b) at (frequency 11.3 kHz)

The printed microstructure at a temperature of 150 °C under an applied load of 5000 N and 10 sec duration of the printing (Fig. 3.34) achieved the highest quality of the replica. Optical microscope images were obtained for various temperature, force, time durations, and with and without vibratory excitations; they are presented in the Appendix. From the graphs presented in Figs. 3.25–3.33, it is evident that a higher load and temperature with vibratory excitation leads to the achievement of a higher RDE of the replicas. In Fig. 3.34 (a) showing an image captured without vibratory excitation and in Fig 3.34 (b) featuring vibratory excitation, it clearly visible that the entire process assisted with vibratory excitation filling of the cavity is far superior in comparison to the level achieved without vibratory excitation.

3.7. Chapter conclusion

1. A design of the sonotrode was done for vibration-based thermal imprinting device acting in the normal direction of the formed surface. A damping ration of the designed sonotrode of 0.02 was determined from the bump test analysis.
2. The resonant frequency of the designed sonotrode varies from 15.1 kHz to 10.5 kHz depending on the working conditions, whereas the anti-resonance frequency varies from 15.5 kHz to 10.3 kHz. It is possible to state that resonant and anti-resonant frequency has direct dependence on the load, i.e., a higher load induces a

higher frequency. Simultaneously, a higher imprint temperature leads to lower resonant and anti-resonant frequencies. From the thermal camera analysis, it was found that the sonotrode functions well, and it shows equal temperature distribution across the entire contact surface of the sonotrode.

3. Finite element analysis of the sonotrode demonstrates the sonotrode acting in the normal direction of the formed surface at 11.223 kHz, and the highest displacement of the bottom contact surface of 0.18 mm was achieved.
4. The RDE of the printed microstructure was evaluated when the applied load was 5000 N, and 150 °C temperature was used and 10 sec duration of the printing was set; then, with and without vibratory excitation, 53.42% and 40.12% was achieved. It was observed that, when the load decreased by 1000 N (i.e., to 4000 N) at the same printing time duration, a 13% difference was observed in RDE with vibrational excitation. Similarly, when hot imprinting was performed at a temperature of 125 °C and with 10 sec duration of the printing under an applied load of 5000 N, the obtained values of RDE were 48.43% and 37.48% with and without vibrational excitation. When the temperature decreases, the RDE of the replica also decreases for the same applied load and duration of the printing.
5. From the diffraction efficiency measurement, such parameters as the applied load, time duration, as well as the temperature and vibrational excitation exert influence on the quality of the replica. The highest RDE was obtained at 150 °C under 5000 N load and 10 sec of duration when assisted with vibratory excitation.
6. Optical microscope images clearly show that the application of vibratory excitation helps filling the cavity provide superior results than the levels without vibratory excitation.

4. OPTICAL ELEMENT FORMATION FOR VISUAL CRYPTOGRAPHY SYSTEM

This chapter of the dissertation discusses a visual dynamic system. In this chapter, a concept of a novel cantilever-type microsystem platform in the field of biomechanics using an optical technique of image encryption and communication scheme based on computer generated holography is proposed. The methodology of the visual cryptography and optical element results are published in *Nanostructured Materials for the Detection of CBRN", Springer Nature America, Inc.*, 2018, and it was also presented at *MEMSTECH 2019* conference. An image hiding technique based on computer generated holography and dynamic visual cryptography is employed.

Dynamic visual cryptography is a visual cryptography scheme based on time averaging geometric moiré. It is used together with the Gerchberg-Saxton algorithm and 3D microstructure manufacturing techniques intended to design the optical scheme. Stochastic moiré grating is used to embed the secret image into a cover image. The image can visually be decoded with a naked eye – the secret is revealed if the amplitude of harmonic oscillations in the Fourier plane corresponds to an accurately preselected value. The phase information of a computer-generated hologram is then formed on a piezoelectric cantilever-type microsystem platform by using electron beam lithography. It serves as an optical element for the visual inspections of dynamical changes in the investigated biological environment.

4.1. Visual dynamic cryptography system

Replication of periodic microstructures is performed after determining sets of appropriate process parameters. The aim of this experiment is to determine how the diffraction efficiency of the embossed DOE depends on the additional heat generation through pre-structured foils.

The optical image hiding scheme based on computer-based holography and time averaging moiré and its experimental implementation was introduced in [123–125]. During the encryption process of this optical scheme, an image hiding technique based on the optical time-averaging moiré is used to encrypt the secret image. Furthermore, the Gerchberg-Saxton algorithm is used to obtain the phase data from the previously encrypted secret image. Ultimately, various 3D microstructure manufacturing techniques are used to fabricate a computer-based hologram that corresponds to the retrieved phase data. The decryption is performed by illuminating the computer-generated hologram with a coherent laser beam. The light distribution of the encrypted data is obtained in the Fourier plane. Oscillation of obtained image with a predefined amplitude decrypts the encrypted image, and the secret image is retrieved. The methods used for encrypting the image by using dynamic visual cryptography and retrieving the phase distribution of the computer-generated hologram are outlined in the following sections.

In this section, an image hiding technique based on optical time-averaging moiré that is used to encrypt the secret image is given [126]. Let us define a one-dimensional harmonic moiré grating:

$$\overline{F}(x) = \frac{1}{2} + \frac{1}{2}\cos\left(\frac{2\pi}{\lambda}x\right) \tag{4.1}$$

where λ is the pitch of the grating; F (x) is the grayscale level ranging from 0 to 1. Here, 0 represents the black 'color', and 1 represents the white color. This one-dimensional harmonic moiré grating performs non-deformable oscillations around the state of equilibrium. A defection from the state of equilibrium does not depend on variable *x*:

$$\mathrm{u\ (x,\ t)\ =\ u\ (t)\ =\ a\ sin\ (}\omega t\ +\ \varphi) \tag{4.2}$$

where ω is the angular frequency; φ is the phase and a is the amplitude of the oscillation. Thus, the time-averaged image is defined as follows [127]:

$$\begin{aligned}\overline{F}(x) &= \lim_{T\to\infty}\frac{1}{T}\int_0^T F(x - a\sin(\omega t + \phi)\,dt \\ &= \frac{1}{2} + \frac{1}{2}\cos\left(\frac{2\pi}{\lambda}x\right)J_0\left(\frac{2\pi}{\lambda}a\right),\end{aligned} \tag{4.3}$$

where T is the exposure time; J_0 is the zero-th order Bessel function of the first kind. The original moiré grating is mapped into a time-averaged fringe ($\overline{F}$ (x) = 0.5) when J_0 becomes equal to zero. Thus, the relationship between the pitch of the moiré grating λ, the amplitude of harmonic oscillations a, and the consecutive number of the time-averaged moiré fringe k reads as follows:

$$\frac{2\pi}{\lambda}a_k = r_k,\ k = 1, 2, \ldots \tag{4.4}$$

where r_k is the k-th root of J_0; a_k is the discrete value of the amplitude which results in the k-th time-averaged fringe in the time-averaged image. The phase matching algorithm is used to eliminate discontinuities at the boundaries between the background and the secret image, and the stochastic initial phase defection algorithm is used to encrypt the secret.

4.2. Generating a computer-generated hologram

The Gerchberg-Saxton algorithm with FFT is applied in CGH computation. When discrete data is involved, DFT for digital signal processing is employed. The transformation converts space/time-based data into frequency-based data, and the conversion is described with the following formula:

$$F(u,v) = \frac{1}{NM}\sum_{x=0}^{M-1}\sum_{y=0}^{M-1} f(x,y)e^{-i2\pi\left(\frac{xu}{M}+\frac{yn}{N}\right)}, \tag{4.5}$$

where *u* and *v* are discrete spatial frequencies, *M* and *N* represent the quantity of sections in *x* and *y* directions of space and frequency domains, *F(u,v)* – 2D discrete *f(x,y)* spectra.

Initially, an arbitrary number generator creates phase scattering *φ[−π, π]*. The steps of the Gerchberg-Saxton algorithm are the following:
The initial field u_n^H is calculated in the hologram plane:

$$u_n^H = A(I_H)\exp(i\varphi_{n-1}^H), \tag{4.6}$$

The initial field u_n^H is propagated from the image plane to the object plane, and the amplitude information is discarded:

$$\varphi_n^T = P(FFT(u_n^H)), \tag{4.7}$$

The amplitude and the phase of the illumination field are added to the phase information in order to retrieve the object field u_n^T:

$$u_n^T = A(I_T)\exp(i\varphi_n^T), \tag{4.8}$$

The object field u_n^T is propagated from the object plane to the image plane:

$$\varphi_n^H = P(FFT^{-1}(u_n^T)), \tag{4.9}$$

The reconstructed I_n and the expected images are compared, and iterative quality assessment begins. The correlation between the images is calculated in order to determine the necessity of additional iterations. The calculations are finished when the adequate quality of the hologram is achieved, i.e., when further iterations do not improve the quality which is defined by a specific threshold:

$$I_n = \left|u_n^T\right|^2, \tag{4.10}$$

The phase of the reconstructed image is combined with the field amplitude of the expected irradiance, and, should additional iterations be necessary, the process is repeated from the initial step.

The amplitude extracting function *A(z)* of complex numbers is defined as follows:

$$A(z) = \sqrt{x^2 + y^2}, \tag{4.11}$$

The angle extracting function *P(z)* is expressed as:

$$P(z) = \tan^{-1}\left(\frac{y}{x}\right), \tag{4.12}$$

CGH generation is realized with *MATLAB* software. Direct DFT computation of the *N*-point requires N^2 complex multiplications and $N(N-1)$ complex additions. However, FFT reduces the amount of calculation.

4.3. Computational simulation of an optical image hiding scheme

The results of the computational simulation of the optical image hiding scheme based on computer-based holography and time-averaging moiré are shown in Fig. 4.1. The secret image containing a black solid circle on a white background is given in part (a). The original encrypted image using the image hiding technique based on an optical time-averaging moiré is given in part (b). The computational simulations were performed by using 10 × 10 composite pixel size. This results in the reduction of the noise influence that is related to the diffraction and interference of the theoretical limits of computer-generated holography. The phase data of a computer-generated hologram is given in part (c). The reconstructed image of the computer-generated hologram in the observation plane is given in part (d). The decrypted image without Gerchberg–Saxton algorithm is given in part (e). The decrypted image with the applied Gerchberg-Saxton algorithm is shown in part (f). One should note that various

contrast enhancement techniques (such as the one given in [126]) can be used to increase the image quality and readability.

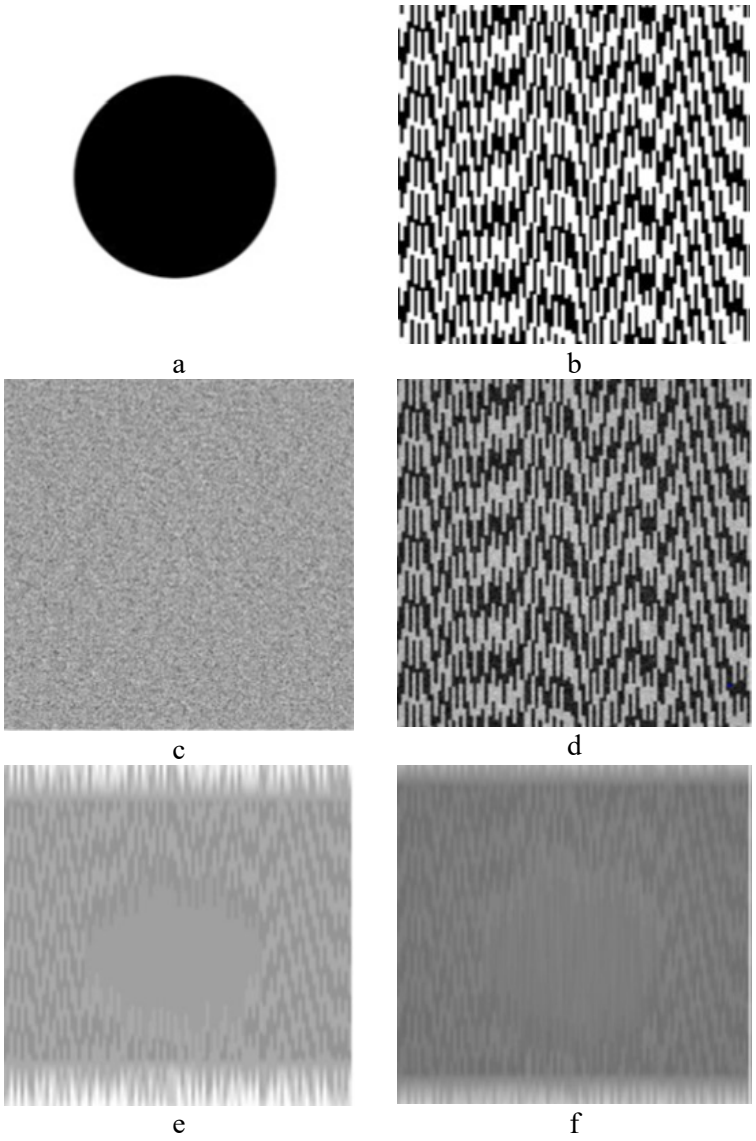

Fig. 4. 1 The secret image is given in part (a); the encrypted image is given in part (b); phase data is given in part (c); intensity distribution in the observation plane is given in part (d); decryption results with and without the Gerchberg-Saxton algorithm are given in parts (e) and (f), respectively

In order to produce a computer-generated hologram, the following procedure and materials were used: the size of the generated computer-generated hologram is 1x1 mm. A 3D microstructure representing a computer generated hologram is designed for the exposition on polymethyl methacrylate and the reconstruction with a He-Ne laser (with a wavelength of $\lambda = 632.8$ nm). The molecular mass of polymethyl methacrylate is 35 K, and the refractive index is 1.49. The pixels of the designed computer-generated hologram have eight grayscale levels ranging from black to white. The black 'color' represents the biggest thickness of polymethyl methacrylate (it is not exposed), whereas the white color represents the smallest thickness of polymethyl methacrylate under maximum exposition (Fig. 4.2).

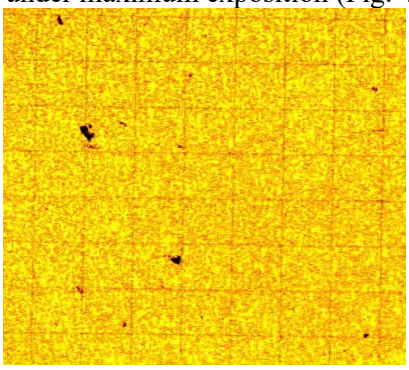

Fig. 4. 2 Computer generated hologram exposed on polymethyl methacrylate

4.4. Manufacturing and investigation of a micro-optical functional element

A Raith e-LiNEplus high resolution system was used for the electron beam lithography process. This system is equipped with a Schottky thermionic field emission gun.

A silicon wafer whose dimensions are 10 x10 mm was exposed to oxygen plasma with the duration of exposition of 5 min. The wafer was then heated for 30 min at 150 °C on a hotplate. Afterwards, polymethyl methacrylate resist whose molecular weight is 35 K was spin-coated at 2000 rpm and dried at a temperature of 200 °C on a hotplate. E-beam 3D writing was done at the nominal exposure dose of 110 μC/cm^2. The polymethyl methacrylate resist was developed by using isopropyl alcohol and 1:3 methyl isobutyl ketone solvent. After the development, the specimens were washed with water and then dried with compressed air blow.

The 3D microstructure created in polymethyl methacrylate was metalized with a 20 nm nickel Film ($T_{melting}$ = 1455 °C) (purity 99.99%, *Sigma Aldrich*, UK) by using electron beam evaporation ($T_{substrate}$ = 20º C, residual gas pressure 1e–4 Pa, deposition rate v = 1–2 nm/s). The image of the computer-generated hologram exposed on polymethyl methacrylate and the intensity distribution of the computer-generated hologram in the projection plane are shown in Fig. 4.2. The photo of the fabricated hologram and the surface profile are presented in Fig. 4.3. Also, photos of the fabricated hologram surafce profile when using SEM are presented in the Appendix with various magnifications.

The proposed technique can be exploited for vibration monitoring of the entire experimental setup when the reconstructed image performs oscillations around the state of equilibrium on the observation plane. Alternatively, the proposed technique can be exploited for visual monitoring of the vibrations of micro-components carrying the computer-generated hologram.

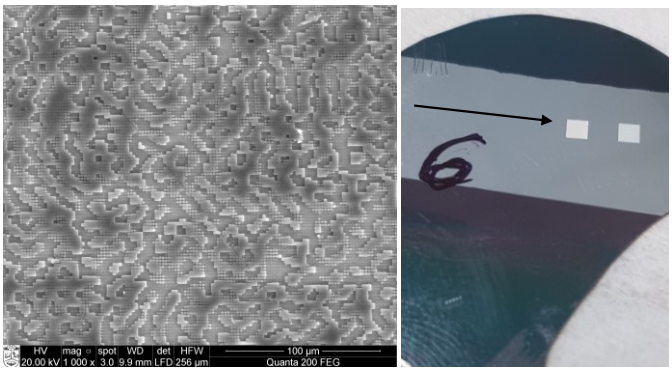

Fig. 4. 3 SEM image (left) and photo (right, the arrow depicts an area of 1x1mm) of the produced hologram

In order to use such an optical element for decryption (decoding), it is necessary to control it according to the harmonic law expressing the prevailing amplitude that was used for encrypting (coding) the initial image (circle) as shown in Fig. 4.1. For this purpose, a platform made of aluminum was used as shown in Fig. 4.4.

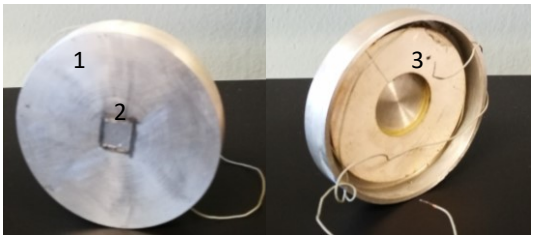

Fig. 4. 4 Disc-shaped control platform (1) with a micro optical element (2) and an active piezoelectric element (3)

A 3D model of the prepared aluminum disc-shaped platform for the experiment is shown in Fig. 4.5.

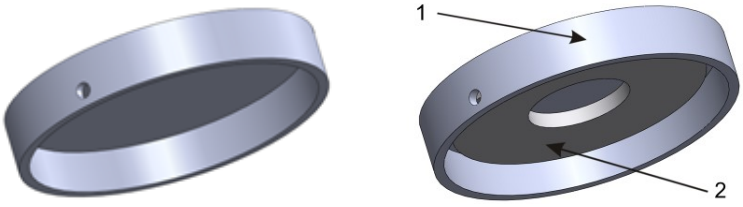

Fig. 4. 5 3D view of the disc-shaped aluminum platform (a) and the vibration platform (1) a the piezoelectric element (2) being attached (b)

The dimensions of the disc-shaped platform (outer diameter 60 mm, wall thickness 3 mm, height 10 mm) with a ring of a piezoelectric material (*PZT-5H*) (external diameter 50 mm, internal diameter 20 mm, thickness 3 mm) was used for surface deformation control. Such a platform is used for the control of a micro optical element mounted in its centre.

After the assembly of the platform, dynamic analysis of the control platform was performed in order to know the modes of vibration and the average speed spectrum with the specific operating modes. The experimental setup is presented in Fig. 4.6.

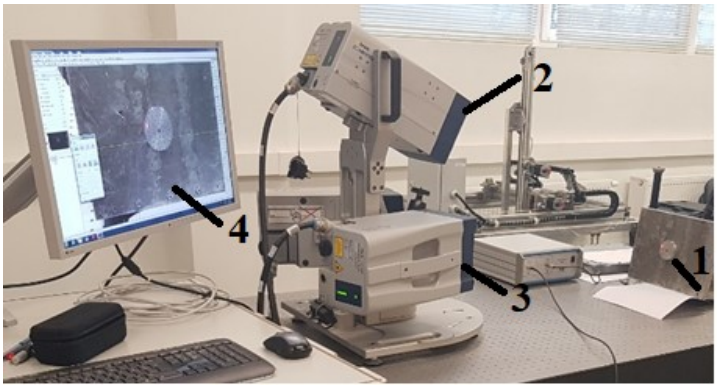

Fig. 4. 6 Aluminum platform (1), 3D vibrometer Polytec PSV-500-3D-HV laser heads (1–2), and computer system (3)

Dynamic analysis of the control platform was accomplished on a 3D vibrometer *Polytec PSV-500-3D-HV* (Fig. 4.6) with laser beam positioning accuracy greater (higher) than 0.0002° when the range of the vibration rate (speed) measurement was from 0.001 to 10 m / s with 13 ranges up to 25 MHz.

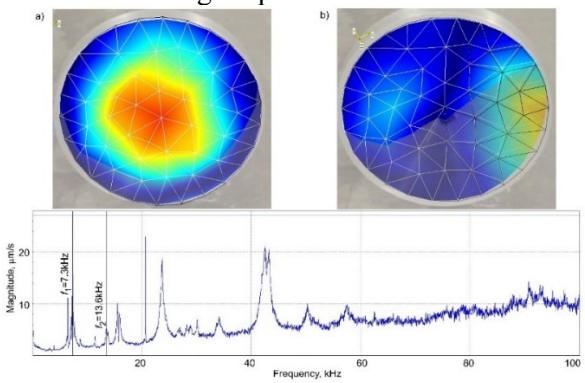

Fig. 4. 7 The first (a) and second (b) vibration modes and the average speed spectrum with the specified operating modes f1 = 7.3 kHz and f2 = 13.6 kHz that were selected for the manipulation of the control platform with an optical element

The results of dynamic analysis are presented in Fig. 4.7. The second form (pattern) of oscillation (f_2 = 13.6 kHz) was selected for the control of the optical element since it ensures cyclic rotation of the optical element in the centre of the

platform at an angle $\alpha = 1.8 \pm 0.09''$ providing an amplitude of 8.6 μm. Only in this case the image coded by dynamic visual cryptography and digital holography methods might be visible.

4.5. Experimental realization of a micro-optical functional element

The practical application of an image coded by dynamic visual cryptography and digital holography (Fig. 4.8) involves a micro-optical element pasted on an aluminum platform, a high frequency vibration generator, a voltage amplifier, a semiconductor laser, a digital camera, lenses, a corrector of the laser beam intensity, and a computer monitor system with a camera image system.

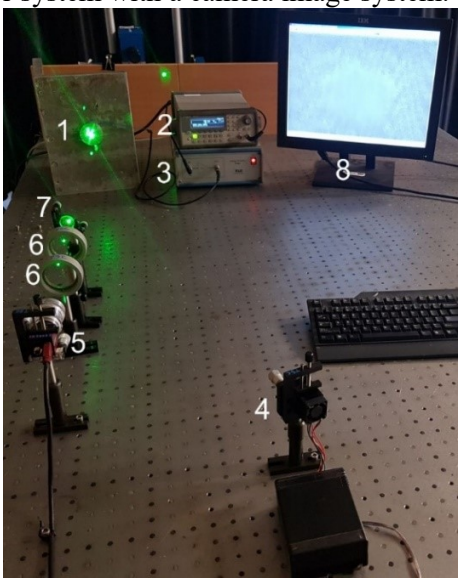

Fig. 4. 8 Stand for the test of a micro-optical element: 1 – micro-optical element, 2 – high frequency vibration generator, 3 – voltage amplifier, 4 – semiconductor laser, 5 – digital camera, 6 – two lens system, 7 – corrector of laser beam intensity, 8 – computer monitor

The explored micro-optical element is attached to the control unit (1) which, during the dynamic process identification, is excited with a high-frequency vibration generator *Agilent 33220a* (2), while the excitation voltage is amplified 10 times by using a single channel high voltage linear amplifier *F10A* developed by *FLC Electronics* (3). The optical element is illuminated with a beam of a semiconductor laser (4) (λ = 532nm), and the image generated by the digital hologram carrying information about the characteristics of the dynamic system is recorded with the aid of an optical system consisting of a *Guppy F-503 B&W CMOS* camera (5), a two-lens system (featuring a focal length of 600mm) (6), and a corrector of the laser beam intensity (7). The camera's recorded image in the real time is monitored on the computer screen (8).

It is clearly seen that whenever the controller of the micro-optical element is activated by the f_2 = 13.6 kHz frequency and 100V voltage electrical signal, the

restored circle can be observed on the monitor. This means that the micro-optical element is cyclically rotated about the horizontal axis at an angle of α=1.8±0.09″.

In order to analyze the phase object of the printed CGH, it is necessary to print the CGH micro optical element on a transparent polycarbonate sheet by using the thermal imprinting technology developed in Chapter 3. Therefore, the developed thermal imprint technology which allows to duplicate the CGH micro optical elements in polycarbonate (Fig. 4.9) is used to analyze phase objects.

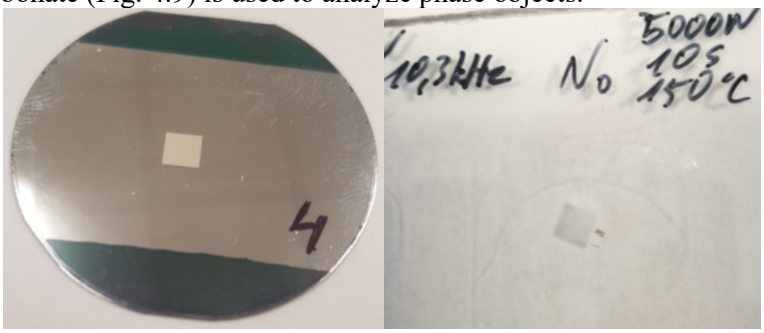

Fig. 4. 9 Micro-optical element (a) and its replica formed in polycarbonate by polycarbonate thermal forming

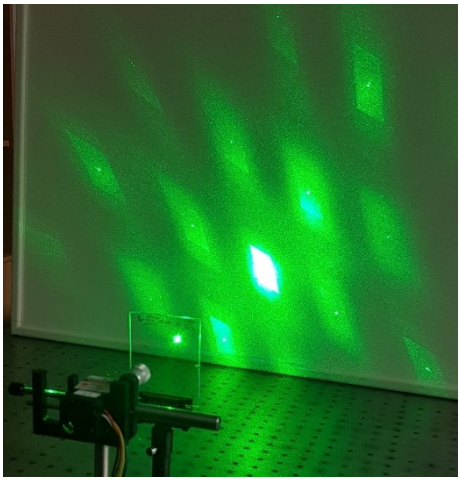

Fig. 4. 10 Diffractive image generated by a laser-lit micro-optical element formed in polycarbonate

The optical element developed by this technology can be integrated into the diffraction efficiency measurement scheme presented in Chapter 3.5.3. The functionality of the printed element is shown in Fig. 4.10. It can be easily transformed into a scheme based on the characteristics of transparent phase objects.

4.6. Cantilever-type microsystem platform

The designed biomechanical system is a piezoelectric-based cantilever. A schematic view of the designed system is given in Fig. 4.11.

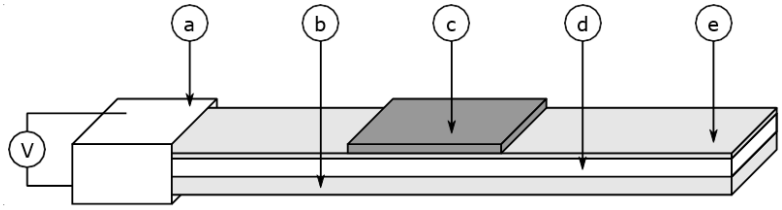

Fig. 4. 11 Principal scheme of a cantilever type piezoelectric microsystem platform composed of clamping block a), copper film b), computer generated hologram c), piezoelectric composite d), and electrode e)

The cantilever is composed of a 50μm thick copper film (Young's modulus E = 117 GPa, and density $\rho = 8940$ kg/m^2), a 20 nm thick aluminum electrode (Young's modulus E = 70 GPa, and density $\rho = 2700$ kg/m^2), and a 50μm thick piezoelectric composite (Young's modulus E = 3.9GPa, and density $\rho = 6298$ kg/m^2) – polyvinyl butyral 20% mixed together with PZT powder. The cantilever is then coated with a thin film (500 nm) of polyethylene (Young's modulus E = 0.8GPa, and density $\rho = 940$ kg/m^2) working as an insulator from the environmental conditions. Finally, a computer-generated hologram is attached to a cantilever.

The procedure and materials to produce a computer-generated hologram are described in detail in Chapter 4.3. A computer generated hologram is designed for exposition on polymethyl methacrylate (the molecular mass of polymethyl methacrylate is 35 K, and the refractive index is 1.49), and the reconstruction with a He-Ne laser (whose wavelength equals $\lambda = 632.8$ nm) is performed. The pixels of the designed computer-generated hologram have eight grayscale levels ranging from black to white. The black 'color' represents the biggest thickness of polymethyl methacrylate (it is not exposed), whereas the white color represents the smallest thickness of polymethyl methacrylate under maximum exposition. A *Raith e-LiNEplus* high resolution system was used for the electron beam lithography process. An image of a computer-generated hologram exposed on polymethyl methacrylate is shown in Fig. 4.2.

The proposed technique can be employed for the monitoring of biomedical systems when the reconstructed image performs oscillations around the state of equilibrium on the observation plane – the changes in the amplitude of oscillations due to the changes in the environmental conditions would result in the changes of the target image on the observation plane. The proposed technique could be employed for the monitoring of glucose levels in diabetes patients. A cantilever could be immersed in the sensing fluid which is made of protein concanavalin-A and polymer dextran. Furthermore, this sensing fluid would be exchanging glucose with the fluid outside this setup via a cellulose acetate semipermeable membrane. Changes in the viscosity of the sensing fluid (the result of the interaction of glucose with concanavalin-A) introduce changes in the amplitude of the oscillations of the cantilever. As mentioned

above, changes in the amplitude of oscillations result in the changes of the target image on the observation plane. This approach can be used to detect changes in any other biological environment.

4.7. Chapter conclusion

1. An image encryption scheme based on time-averaged moiré and computer-generated holography is investigated. The secret message is embedded into a cover image by using a stochastic moiré grating which can be visually decoded with a naked eye – the secret is revealed if the amplitude of harmonic oscillations in the Fourier plane corresponds to an accurately preselected value. One should note that the decryption is completely optical and does not require utilization of a computing device.
2. The process of the production of a computer-generated hologram is presented. Computer-generated holography is used in the design step, and electron beam lithography is employed for physical 3D patterning.
3. By using the synergy of these methods, an optical element, in which information is coded by digital holography, is developed; it allows identifying various micro-liquid processes which are qualified before coding of the optical element. The usage of an optical element enables to recognize micro-liquid processes in real time by their coincidence (in the case of a coincidence of the coded image and the real process, it is possible to determine the dynamic characteristics of the micro-liquid device and the operating modes of the device).
4. A concept of a novel cantilever-type microsystem platform in the field of biomechanics using an optical technique of image encryption and communication based on computer generated holography is proposed. An image hiding technique based on computer generated holography and dynamic visual cryptography is employed to retrieve the phase information of a computer-generated hologram. The proposed sensing platform with the piezoelectric effect employs the active method for measurements in medical or pharmaceutical fields.

5. GENERAL CONCLUSIONS

1. The improvement of complex 3D microstructures dependent on computer created holography and their utilization for biomedical applications so that to create a visual cryptography framework was a new idea of a novel microsystem stage with a small-scale optical component for the field of biomechanics using an optical method of picture encryption and correspondence dependent on computer produced holography; this is the main objective of this dissertation.
2. Investigation of the influence of the forced high vibrational frequency acting in the normal direction to the imprinted surface has been performed. The simulation results show that vibratory excitation may lead to a deeper profile than that obtained without vibratory excitation. An increase of depth by 0.45 or 0.5 μm was observed when the process duration was 10 and 20 s, respectively, with vibration. On the other hand, the FEM model of the sonotrode verified experimentally the profile depth of 1.2 μm and 1.7 μm observed without and with vibratory excitation when the time duration was set at 10 sec. The results of the simulation and experimental research did not differ more than by 9%. The obtained differences between the experimental and the computational profile depth values were within acceptable limits.

   The application of vibration excitation during the thermal imprint process increases the depth of the imprinted profiles and results in uniform distribution of plastic deformations and Von Misses stresses. The results show that the developed process proves that, with assistance of vibratory excitation, the profile depth and the quality of the printed structure are better than without vibratory excitation.
3. The damping ratio of the designed sonotrode (0.02) was found from the bump test analysis. The resonant frequency of the designed sonotrode varies from 15.1 kHz to 10.5 kHz depending on the working conditions, whereas anti-resonance frequency varies from 15.5 kHz to 10.3 kHz. Also, thermal camera analysis determined that the sonotrode functions well, and it shows equal temperature distribution across the entire contact surface of the sonotrode. Finite element analysis of the developed sonotrode demonstrates the sonotrode acting in the normal direction of the formed surface at 11.223 kHz, and the contact points were analyzed; the highest displacement of the bottom contact surface was found to equal 180 μm.
4. Diffraction efficiency measurement was performed in order to analyze the operating regime of the printed microstructure. RDE of 53.42% and 40.12% was achieved with and without vibratory excitation when the replica produced under a load of 5000 N at 150 °C temperature and 10 sec duration of the printing. From the changing parameters, such as the decrement in the applied load, the temperature of printing, the duration of printing, and the application of vibratory excitation, decrement in the diffraction efficiency as well as the quality of the printing is achieved. Also, microscopic images revealed that the quality of the printed microstructure was superior when vibratory excitation was employed.
5. A concept of a novel cantilever-type microsystem platform in the field of biomechanics using an optical technique of image encryption and communication

based on computer generated holography has been proposed. A computer-generated hologram is then formed on a piezoelectric cantilever-type microsystem platform. Electron beam lithography is employed for physical 3D patterning. It serves as an optical element for visual inspections of dynamical changes in the investigated biological environment. A combination of unique properties allows real time and direct observations of affinity interactions. The proposed sensing platform with the piezoelectric effect employs an active method for measurements in medical or pharmaceutical fields.

REFERENCES

1. Yang, F., Murugan, R., Ramakrishna, S., Wang, X., Ma, Y.-X., and Wang, S. 2004. Fabrication of nano-structured porous PLLA scaffold intended for nerve tissue engineering. Biomater. 25: 1891–1900.
2. Smith, L.A., Liu, X., and Ma, P.X. 2008. Tissue engineering with nano-fibrous scaffolds. Soft Matter 4(11): 2144–2149.
3. Weilbaecher, C.R., Hossain, M., Gangopadhyay, S., and Grant, S. 2007. *Development of a novel nanomaterial-based optical platform for a protease biosensor*. Proc. SPIE, Vol. 6759.
4. Naeemi, A. and Meindl, J.D. 2009. Carbon nanotube interconnects. *Ann. Rev. Mater. Res.* 39: 255–275.
5. Nanostructured materials in information storage. *MRS Bull*. 33: 831–834.
6. Zhang, Y., Lu, J., Shimano, S., Zhou, H., and Maeda, R. 2007. Nanoimprint of proton exchange membrane for MEMS-based fuel cell application. Proc. 6th Int. IEEE Conf. on Polymers and Adhesives in Microelectronics and Photonics, pp. 91–95.
7. Zhang, Y., Lu, J., Wang, Q., Takahashi, M., Itoh, T., and Maeda, R. 2009. Nanoimprint of polymer electrolyte membrane for micro direct methanol fuel cell application. *ECS Trans. Micro Power Sources* 16: 11–17.
8. Tawarayama, K., Aoyama, H., Magoshi, S., Tanaka, Y., Shirai, S., and Tanaka, H. 2009. *Recent progress of EUV full field exposure tool in Selete*. Proc. SPIE, Vol. 7271.
9. Smith, H.I., Carter, D.J.D., Ferrera, J., Gil, D., Goodberlet, J., Hastings, J.T. *et al*. 2000. Soft X-rays for deep sub-100 nm lithography, with and without masks. *Proc. Mater. Res. Soc. Symp.* 584: 11–21.
10. Malek, C.K. and Saile, V. 2004. Applications of LIGA technology to precision manufacturing of high-aspect-ratio micro-components and -systems: A review. *Microelectron. J.* 35: 131–143.
11. Lu, B., Xie, S.-Q., Wan, J., Yang, R., Shu, Z., Qu, X.-P. *et al*. 2009. Applications of nanoimprint lithography for biochemical and nanophotonic structures using SU-8. *Int. J. Nanosci.* 8: 151–155.
12. Kawata, S., Sun, H.-B., Tanaka, T., and Takada, K. 2001. Finer features for functional microdevices. *Nature* 412(6848): 697–698.
13. Ito, H, et al. Polymer structure and properties in micro- and nanomolding process. Current Applied Physics, 2009, vol. 9, p. 19–24.
14. Heckele M.; Schomburg, W.K. Review on micro molding of thermoplastic polymers. Journal of Micromechanics and Microengineering, 2004, 14, p. 1-14.
15. Worgull M., et al. Modeling and optimization of the hot embossing process for micro- and nanocomponent fabrication. Microsystem Technologies, 2006, 12, p. 947-952.
16. Krauss, P.R.; Chou, S.Y. Nano-compact disks with 400 Gbit/in^2 storage density fabricated using nanoimprint lithography and read with proximal probe. Applied Physics Letters, 1997, 71, p. 3174–3176.
17. Jaszewski, R.W., et al. Hot embossing in polymers as a direct way to pattern resist. Microelectronic Engineering, 1998, 41–42, p. 575–578.
18. Juang, Y.J. Polymer processing and rheological analysis near the glass transition temperature. Dissertation, 2001, 230 p.

19. Li, J.M.; Liu, C.; Peng, J. Effect of hot embossing process parameters on polymer flow and microchannel accuracy produced without vacuum. Journal of Materials Processing Technology, 2008, 207, p. 163–171.
20. Giboz, J.; Copponex, T.; Mele, P. Microinjection moulding of thermoplastic polymers: a review. Journal of Micromechanics and Microengineering, 2007, 17, p. 96–109.
21. Sahli, M., et al. Quality assessment of polymer replication by hot embossing and micro-injection moulding processes using scanning mechanical microscopy. Journal of Materials Processing Technology, 2009, 209, p. 5851–5861.
22. Lin, C.R.; Chen, R.H.; Chen, C.H. Preventing non-uniform shrinkage in ope-die hot embossing of PMMA microstructures. Journal Material of Processing Technology, 2003, 140, p. 173-178.
23. Yoshihiko, H.; Yoshida, S.; Nobuyuki, T. Defect analysis in thermal nanoimprint lithography. Journal of Vacuum Science Technology B, 2003, 21, p. 2765-2770.
24. Hu, X.F. Research on the Equipment for hot embossing and related experiments. Master thesis, 2005
25. Yao, D.G.; Vinayshankar, L.V.; Byung, K. Study on squeezing Flow during nonisothermal embossing of polymer microstructure. Journal Polymer Engineering and Science, 2005, 45, p. 652-660.
26. Chang, C.Y., et al. Fabrication of plastic microlens array using gas-assisted micro-hot-embossing with a silicon mould. Infrared Physics and Technology, 2006, 48, p. 163–173.
27. Becker, H.; Heim, U. Hot embossing as a method for the fabrication of polymer high aspect ratio structures. Sensors and Actuators, 2000, 83, p. 130–135.
28. Bogdanski, N., et al. 3D-hot embossing of undercut structures—an approach to micro-zippers. Microelectronic Engineering, 2004, 73–74, p. 190–195.
29. Carvalho, B.L., et al. Soft embossing of microfluidic devices. In Proceedings of the 7th international conference on miniaturized chemical and biochemical analysis systems, October 5–9, 2003, Squaw Valley, California, USA, , 2003, p. 959–962.
30. Guo, Y., et al. Analysis of the demolding forces during hot embossing. Microsystem Technologies, 2007, 13, p. 411-415.
31. Datta, P.; Goettert, J. Method for polymer hot embossing process development. Microsystem Technologies, 2007, 13(3-4), p. 265-270.
32. Yao, D.G., et al., A two-station embossing process for rapid fabrication of surface microstructures on thermoplastic polymers. Polymer Engineering and Science, 2007, 47(4), p. 530-539.
33. Chang, J.H.; Yang, S.Y. Development of rapid heating and uniformly pressing system for micro hot embossing. SPE ANTEC, 2004, 1, p. 942-945
34. Liu, W., et al. Rapid Thermal Response (RTR) Hot Embossing of Micro-Structures. SPE ANTEC Tech Paper, 2004, vol. 1, p. 933-936.
35. Lu, C., et al. Analysis of Laser/IR-Assisted Micro-embossing. Polymer Engineering and Science, 2005, 45, p. 661-668.
36. Grewell, D., et al. Feasibility of selected methods for embossing micro-features in thermoplastics, SPE ANTEC Proceedings, 2003, p. 1094-1097.
37. Liu, J.S.; Dung, Y.T. Hot Embossing Precise Structure Onto Plastic Plates by Ultrasonic Vibration. Polymer Engineering and Science, 2005, 45, p. 915-925.
38. Liu, C. et al. Deformation behavior of solid polymer during hot embossing process. Microelectronic Engineering, 2010, 87, p. 200–207.

39. Mekaru, H.; Goto, H.; Takahashi, M. Development of ultrasonic micro hot embossing technology. Microelectronic Engineering, 2007, 84, p. 1282-1287.
40. Hirai, Y.; Yoshida, S.; Takagi, N. Defect analysis in thermal nanoimprint lithography. Journal of Vacuum Science and Technology B, 2003, vol. 21 no. 6, p. 2765-2770.
41. Narijauskaitė, B., et al. High-frequency excitation for thermal imprint of microstructures into a polymer. Experimental Techniques, 2011. (published online: 11 APR 2011)
42. Seunarine, K., et al. Optical heating for short hot embossing cycle times. Microelectronic Engineering, 2006, 83, p 859-863.
43. Yule, A.J.; Al-Suleimani, Y. On droplet formation from capillary waves on a vibrating surface. Mathematical physics and Engineering sciences, 2000, 456, p. 1069-1085.
44. Zhang, A., et al. Rapid concentration of particle and bioparticle suspension based on surface acoustic wave. Applied Acoustics, 2009, vol. 70, 8, p. 1137-1142.
45. Kondoh, J., et al. Development of temperature-control system for liquid droplet using surface Acoustic wave devices. Sensors and Actuators A: Physical, 2009, vol. 149, 2, p. 292-297.
46. Lomonosov, A.M.; Hess, P. Nonlinear surface acoustic waves: Realization of solitary pulses and fracture. Ultrasonics, 2008, vol. 48, 6-7, p. 482-487.
47. Alvarez, M.; Friend, J.R.; Yeo, L.Y. Surface Vibration induced spatial ordering of periodic polymer patterns on a substrate. Langmuir, 2008, 24, p. 10629-10632.
48. Changliang, X.; Mengli, W. Stability analysis of the rotor of ultrasonic motor driving fluid directly. Ultrasonics, 2005, vol. 43, 7, p. 596-601.
49. Ming, Y., et al. Design and evaluation of linear ultrasonic motors for a cardiac compression assist device. Sensors and Actuators A: Physical, 2005, vol. 119, 1, p. 214-220.
50. Nakamura, K.; Maruyama, M.; Ueha, S. A new ultrasonic motor using electro-rheological fluid and torsional vibration. Ultrasonics, 1996, vol. 34, 2-5, p. 261-264.
51. Fairbanks, H.V. Applying ultrasonics to the moulding of plastic powders. Ultrasonics, 1974, 12, p. 22-24.
52. Paul, D.W.; Crawford, R.J. Ultrasonic moulding of plastic powders. Ultrasonics, 1981, 19, p. 23-27.
53. Šakalys, R.; Janušas, G.; Palevičius, A.; Čekas, E.; Jūrėnas, V. (2014) Microstructures replication using high frequency excitation // Microsystem technologies. Berlin: Springer. ISSN 0946-7076. 2016, vol. 00, p. [1-13].
54. Benatar, A.; Gutowski, T.G. Ultrasonic Welding of PEEK Graphite APC-2 Composites. Polymer Engineering and Science, 1989, vol. 29, no. 23, p. 1705-1721.
55. Nonhof, C.J.; Luiten, G.A. Estimates for process conditions during the ultrasonic welding of thermoplastics. Polymer Engineering and Science, 1996, 36, p. 1177-1183.
56. Liu S.J and Dung Y.T (2005) Hot embossing precise structure onto plastic plates by ultrasonic vibration. Polymer Engineering & Science., 45(7): 915-925.
57. Seo Y.S and Park K (2012) Direct patterning of micro-features on a polymer substrate using ultrasonic vibration. Microsystem Technologies., 18(12): 2053-2061.

58. Chien-Hung L and Rongshun C (2007) Effects of mold geometries and imprinted polymer resist thickness on ultrasonic nanoimprint lithography. Journal of Micromechanics and Microengineering., 17(7): 1220.
59. Mekaru H, Nakamura O, Maruyama O, Maeda R and Hattori T (2006) Development of precision transfer technology of atmospheric hot embossing by ultrasonic vibration. Microsystem Technologies., 13(3): 385-391.
60. Linfa P, Yujun D, Peiyun Y and Xinmin L (2014) Micro hot embossing of thermoplastic polymers: a review. Journal of Micromechanics and Microengineering., 24(1): 013001.
61. Šakalys, R. (2017). A study of the influence of high-frequency excitation on the quality of microstructures replicated by thermal imprint technologies: Doctoral dissertation: Technological sciences, mechanical engineering (09T). Kaunas.
62. Narijauskaitė B, Palevičius A, Gaidys R, Janušas G, Šakalys R (2013) Polycarbonate as an Elasto-Plastic Material Model for Simulation of the Microstructure Hot Imprint Process. Sensors (Basel, Switzerland).;13(9):11229-11242. doi:10.3390/s130911229.
63. Lin C.R, Chen R.H, Hung, (2002) The characterisation and finite element Analysis of a Polymer under Hot Pressing. The International Journal of Advanced Manufacturing Technology., 20, p. 230-235.
64. Lan S, Lee H. J, Lee S. H, NI J, Lai X, Lee H.W, Lee M. G (2009) Experimental and numerical study on the viscoelastic property of polycarbonate near glass transition temperature for micro thermal imprint process. Materials and Design., 30(9), 3879-3884.
65. Xing H.L, Makinouchi A (2002) FE modeling of thermo-elasto-plastic finite deformation and its application in sheet warm forming. Engineering Computations., Vol. 19 Issue: 4, pp.392-410
66. Solimeno, S.; Crosignani, B.; DiPorto, P. Guiding, diffraction and confinement of optical radiation, 1986, p. 450-452.
67. Loewen, E.G.; Popov, E. Diffraction Gratings and Applications, Optical Engineering Series, Marcel Dekker, New York - Basel, 1997, 601 p.
68. Titus, C.M., Bos, P.J. Efficient, polarization-independent, reflective liquid crystal phase grating, Appl. Phys. Lett., 1997, vol. 71.
69. Xie, H.; Shang, H.; Dai, F.; Li, B.; Xing, Y. Phase shifting SEM moiré method. Optics & Laser Technology, June 2004, vol. 36, iss. 4, p. 291-297.
70. Du, H.; Xie, H.; Guo, Z.; Pan, B.; Luo, Q.; Gu, C.; Jiang, H.; Rong, L. Large-deformation analysis in microscopic area using micro-moiré methods with a focused ion beam milling grating. Optics and Lasers in Engineering, December 2007, vol. 45, iss. 12, p. 1157-1169.
71. Vass, Cs.; Osvay, K.; Csete, M.; Hopp, B. Fabrication of 550 nm gratings in fused silica by laser induced backside wet etching technique. Applied Surface Science, 31 July 2007, vol. 253, iss. 19, p. 8059-8063.
72. Soppa, E.; Doumalin, P.; Binkele, P.; Wiesendanger, T.; Bornert, M.; Schmauder, S. Experimental and numerical characterisation of in-plane deformation in two-phase materials. Computational Materials Science, July 2001, vol. 21, iss. 3, p. 261-275.
73. Trinker, M.; Jericha, E.; Loidl, R.; Rauch, H. Microfabricated silicon gratings as neutron-optical components. Nuclear Instruments and Methods in Physics Research Section A: Accelerators, Spectrometers, Detectors and Associated Equipment, 11 February 2008, vol. 586, iss. 1, p. 124-128.

74. Content, D. Diffraction grating groove analysis used to predict efficiency and scatter performance. SPIE Proceedings, in Conference on Gradient Index, Miniature, and Diffractive Optical Systems, vol. 3778, 1999, p. 19-30.
75. Lee, S.; Nikumb, S. Characteristics of filament induced Dammann gratings fabricated using femtosecond laser. Optics & Laser Technology, October 2007, vol. 39, Issue 7, p. 1328-1333.
76. Gao, H.; Ouyang, M.; Wang, Y.; Shen, Y.; Zhou, J.; Liu, D. Analysis on diffraction properties of the transmission phase grating. Optik - International Journal for Light and Electron Optics, 6 September 2007, vol. 118, iss. 9, p. 452-456.
77. Elfström, H.; Kuittinen, M.; Vallius, T.; Kleemann, B.H.; Ruoff, J.; Arnold, R. Fabrication of blazed gratings by area-coded effective medium structures. Optics Communications, 15 October 2006, vol. 266, iss. 2, p. 697-703.
78. Giannattasio, A.; Hooper, I.R.; Barnes, W.L. Dependence on surface profile in grating-assisted coupling of light to surface plasmon-polaritons. Optics Communications, 15 May 2006, vol. 261, iss. 2, p. 291-295.
79. Antos, R.; Ohlidal, I.; Mistrik, J.; Murakami, K.; Yamaguchi, T.; Pistora, J.; Horie, M.; Visnovsky, S. Spectroscopic ellipsometry on lamellar gratings. Applied Surface Science, 2005, vol. 244, p. 225-229.
80. Huang, H.T.; Terry, F.L. Spectroscopic ellipsometry and reflectometry from gratings (Scatterometry) for critical dimension measurement and in situ, real-time process monitoring. Thin Solid Films, 2004, vol. 468, p. 339 – 346.
81. Goldenberg, L.; Sakhno, O.; Stumpe, J. Application of Norland adhesive for holographic recording. Optical Materials, 2005, vol. 27, p. 1379-1385.
82. Orbons, S.M.; Dijk, L.; Bozkurt, M.; Johnston, P.N.; Reichart, P.; Jamieson, D.N. Focused ion beam machined nanostructures depth profiled by macrochannelling ion beam analysis. Nuclear Instruments and Methods in Physics Research B, 2006, vol. 249, p. 747 – 751.
83. Ostasevicius, V; Janusas, G; Palevicius, A; Gaidys, R; Jurenas, V. Biomechanical microsystems: design, processing and applications : [monograph]. Cham: Springer International Publishing AG, 2017. 282 p. (Lecture notes in computational vision and biomechanics, ISSN 2212-9391, eISSN 2212-9413 ; vol. 24). ISBN 9783319548487. eISBN 9783319548494. DOI: 10.1007/978-3-319-54849-4. [SpringerLink]
84. Wang, W.; Xie, X.; He, S. Optimal Design of a Polyaniline-Coated Surface Acoustic Wave Based Humidity Sensor. *Sensors* 2013, *13*, 16816–16828.
85. Deng, F.; He, Y.; Zhang, C.; Feng, W. A CMOS Humidity Sensor for Passive RFID Sensing Applications. *Sensors* 2014, *14*, 8728–8739.
86. Ponelyte, S.; Palevicius, A. Novel Piezoelectric Effect and Surface Plasmon Resonance-Based Elements for MEMS Applications. *Sensors* 2014, *14*, 6910–6921.
87. Kanoun, O.; Müller, C.; Benchirouf, A.; Sanli, A.; Dinh, T.N.; Al-Hamry, A.; Bu, L.; Gerlach, C.; Bouhamed, A. Flexible Carbon Nanotube Films for High Performance Strain Sensors. *Sensors* 2014, *14*, 10042–10071.
88. Li, B.; Xu, C.; Zheng, J.; Xu, C. Sensitivity of Pressure Sensors Enhanced by Doping Silver Nanowires. *Sensors* 2014, *14*, 9889–9899.
89. Jung, Y.; Kwak, J.-H.; Lee, Y.H.; Kim, W.D.; Hur, S. Development of a Multi-Channel Piezoelectric Acoustic Sensor Based on an Artificial Basilar Membrane. *Sensors* 2014, *14*, 117–128.

90. Islam, M.R.; Ahiabu, A.; Li, X.; Serpe, M.J. Poly (N-isopropylacrylamide) Microgel-Based Optical Devices for Sensing and Biosensing. *Sensors* 2014, *14*, 8984–8995.
91. Feng, G.-H.; Liu, K.-M. Fabrication and Characterization of a Micromachined Swirl-Shaped Ionic Polymer Metal Composite Actuator with Electrodes Exhibiting Asymmetric Resistance. *Sensors* 2014, *14*, 8380–8397.
92. Hara, Y.; Takenaka, Y. Autonomous Oscillation of Polymer Chains Induced by the Belousov–Zhabotinsky Reaction. *Sensors* 2014, *14*, 1497–1510.
93. Urbaitė, S. (2013). Nanokompozicinių plonų plėvelių su periodine mikrostruktūra kūrimas, tyrimas ir taikymas: Daktaro disertacijos santrauka. Kaunas: Kauno technologijos universitetas. Prieiga per eLABa – nacionalinė Lietuvos akademinė elektroninė biblioteka.
94. Petrauskienė, V. (2015). Dynamic visual cryptography based on non-linear oscillations, The Doctoral Dissertation.
95. Yeknami AF (2016) A 300-mV modulator using a gain-enhanced, inverter-based amplifier for medical implant devices. J Low Power Electron Appl 6(1):1
96. Koenig O, Zengerle D, Perle N, Hossfeld S, Neumann B, Behring A, Avci-Adali M, Walker T, Schlensak C, Wendel HP, Nolte A (2017) RNA-eluting surfaces for the modulation of gene expression as a novel stent concept. Pharmaceuticals 10(1):23
97. Su J, Xu H, Sun J, Gong X, Zhao H (2013) Dual delivery of BMP-2 and bFGF from a new nanocomposite scaffold, loaded with vascular stents for large-size mandibular defect regeneration. Int J Mol Sci 14(6):12714
98. Xu H, Su J, Sun J, Ren T (2012) Preparation and characterization of new nano composite scaffolds loaded with vascular stents. Int J Mol Sci 13(3):3366
99. An P, Yuan W, Ren S (2009) MEMS biomimetic acoustic pressure gradient sensitive structure for sound source localization. Sensors 9(7):5637
100. Ilik B, Koyuncuoglu A, Ulusan H, Chamanian S, Isik D, Sardan-Sukas O, Kulah H (2017) Thin film PZT acoustic sensor for fully implantable cochlear implants. Proceedings 1(4):366
101. Bonanno A, Sanginario A, Marasso SL, Miccoli B, Bejtka K, Benetto S, Demarchi D (2016) A multipurpose CMOS platform for nanosensing. Sensors 16(12):2034
102. Risi MD, Makhlouf H, Rouse AR, Tanbakuchi AA, Gmitro AF (2014) Design and performance of a multi-point scan confocal microendoscope. Photonics 1(4):421
103. Lu Q, Yadid-Pecht O, Sadowski DC, Mintchev MP (2014) A catheter-based acoustic interrogation device for monitoring motility dynamics of the lower esophageal sphincter. Sensors 14(8):14700
104. Pasinszki T, Krebsz M, Tung TT, Losic D (2017) Carbon nanomaterial based biosensors for non-invasive detection of cancer and disease biomarkers for clinical diagnosis. Sensors 17(8):1–32
105. Yamanaka K, Vestergaard MC, Tamiya E (2016) Printable electrochemical biosensors: a focus on screen-printed electrodes and their application. Sensors 16(10):1761
106. Prabhakaran PN, Renugai M (2012) Design and analysis of capacitive MEMS viscometric sensor for CGM. Int J Emerg Technol 2(11):135
107. Ermakov V, Kruchinin S, Fujiwara A (2008) Electronic nanosensors based on nanotransistor with bistability behaviour. In: Bonca J, Kruchinin S (eds)

Proceeding of NATO ARW“Electron transport in nanosystems”. Springer, pp 341–349
108. Ermakov V, Kruchinin S, Hori H, Fujiwara A (2007) Phenomena of strong electron correlastion in the resonant tunneling. Int J Mod Phys B 11:827–835
109. Yang Z, Wang M, Bai Y, Chen X (2014) A differential capacitive viscometric sensor for continuous glucose monitoring. Springer International Publishing
110. Naor M, Shamir A (1995) Visual cryptography. Springer, Berlin, pp 1–12
111. Ragulskis M, Aleksa A (2009) Image hiding based on time-averaging moire. Opt Commun 282(14):2752
112. Turunen J (1997) Diffrctive optics for industrial and commercial applications. Akademie Verlag, Berlin
113. Suleski TJ, Baggett B, DelaneyWF, Koehler C (1999) Johnson EG, Fabrication of high-spatialfrequency gratings through computer-generated near-field holography. Opt Lett 24(9):602
114. Schilling A, Herzig HP, Stauffer L, Vokinger U, Rossi M (2001) Efficient beam shaping of linear, high-power diode lasers by use of micro-optics. Appl Opt 40(32):5852
115. Kley EB,Wittig LC, Cumme M, Zeitner UD, Dannberg P (1999) Fabrication and properties of refractive micro-optical beam-shaping elements. SPIE 3879:20–31
116. Dufresne ER, Spalding GC, Dearing MT, Sheets SA, Grier DG (2001) Computer-generated holographic optical tweezer arrays. Rev Scient Instrum 72(3):1810
117. Gerchberg RW, Saxton WO, Owen W (1972) A practical algorithm for the determination of the phase from image and diffraction plane pictures. Optik 35:237
118. Wang YY,Wang YR,Wang Y, Li HJ, Sun WJ (2007) Optical image encryption based on binary Fourier transform computer-generated hologram and pixel scrambling technology. Opt Lasers Eng 45(7):761
119. Xi S, Sun X, Liu B, Tian W (2013) Spread spectrum characteristics of {CGH} for double random phase encrypted image. Optik 124(12):1260
120. Kong D, Shen X, Cao L, Zhang H, Zong S, Jin G (2016) Three-dimensional information hierarchical encryption based on computer-generated holograms. Opt Commun 380:387
121. Ma L, Jin W (2018) Symmetric and asymmetric hybrid cryptosystem based on compressive sensing and computer generated holography. Opt Commun 407(Suppl C):51
122. Palevičius, A; Grigaliūnas, V; Janušas, G; Palevičius, P; Šakalys, R. Development of complex 3D microstructures based on computer generated holography and their usage for biomedical applications // Proceedings of SPIE: Nanosensors, biosensors, and info-tech sensors and systems : March 20, 2016, Las Vegas, Nevada, United States / Edited by Vijay K. Varadan. Bellingham, WA: SPIE. ISSN 0277-786X. 2016, vol. 9802, Article 980210, p. [1-8].
123. P. Palevicius, M. Ragulskis, Image communication scheme based on dynamic visual cryptography and computer-generated holography, Optics Communications 335, 161 (2015)
124. P. Palevicius, M. Ragulskis, G. Janusas, A. Palevicius, Image encryption scheme based on computer generated holography and time average moire. Proc.SPIE 10453, 10453 (2017)
125. M. Ragulskis, A. Aleksa, Image hiding based on circular geometric moiré. Optics Communications 282(14), 2752 (2009)

126. M. Ragulskis, Z. Navickas, Evolutionary algorithms for the selection of time lags for time series Experimental Mechanics 49(4), 439 (2009).
127. Rees, D.W.A. Basic Engineering Plasticity. Elsevier, Oxford, 2006, 511 p.
128. De Souza Neto, E. A.; Peric, D.; Owen, D.R.J. *Computational Methods for Plasticity: Theory and Applications*. John Wiley and Sohs, 2008, 791 p.
129. Pérez, J. M., Vilas, J. L., Laza, J. M., Arnáiz, S., Mijangos, F., Bilbao, E., & León, L. M. (2010). Effect of reprocessing and accelerated weathering on ABS properties. Journal of Polymers and the Environment, 18(1), 71–78. https://doi.org/10.1007/s10924-009-0154-7.
130. Šakalys, R. (2017). A study of the influence of high-frequency excitation on the quality of microstructures replicated by thermal imprint technologies: Doctoral dissertation: Technological sciences, mechanical engineering (09T). Kaunas.
131. Narijauskaitė, B. (2013). Mikroreljefo formavimo metodo sukūrimas ir tyrimas: Daktaro disertacijos santrauka. Kaunas: Kauno technologijos universitetas. Prieiga per eLABa – nacionalinė Lietuvos akademinė elektroninė biblioteka.
132. https://lidinco.com/danh-muc-san-pham/ (accessed on July 2017)
133. http://www.testo.com.my/index.php/products-mainmenu-32/by-brands-mainmenu-75/testo-germany-mainmenu-90. (accessed on August 2017)
134. Goel, A.K. Thermodynamically Consistent Large Deformation Constitutive Model for Glassy Polymers. Ph.D. Thesis, University of Nebraska, Lincoln, USA, December 2009; p. 201.

LIST OF AUTHOR'S PUBLICATIONS

Publications in journals listed in the ISI *Web of Science* database with citation index

1. [S1; DE] Sodah, Amer; Gaidys, Rimvydas; Narijauskaitė, Birutė; Šakalys, Rokas; Janušas, Giedrius; Palevičius, Arvydas; Palevičius, Paulius. Analysis of microstructure replication using vibratory assisted thermal imprint process // Microsystem technologies. Berlin: Springer. ISSN 0946-7076. eISSN 1432-1858. 2019, vol. 25, iss. 2, p. 477-486. DOI: 10.1007/s00542-018-3976-1. [Science Citation Index Expanded (Web of Science); Scopus][IF: 1.513; AIF: 4.793; IF/AIF: 0.315; Q3 (2018, InCites JCR SCIE)] [M.kr.: T009] [Contribution: 0.148]
2. [S1; DE] Šakalys, Rokas; Janušas, Giedrius; Palevičius, Arvydas; Čekas, Elingas; Jūrėnas, Vytautas; Sodah, Amer. Microstructures replication using high frequency excitation // Microsystem technologies. Berlin: Springer. ISSN 0946-7076. eISSN 1432-1858. 2016, vol. 22, iss. 7, p. 1831-1843. DOI: 10.1007/s00542-016-2858-7. [Science Citation Index Expanded (Web of Science); SpringerLink] [IF: 1.195; AIF: 4.100; IF/AIF:0.291; Q3 (2016, InCites JCR SCIE)] [M.kr.: T001] [Contribution: 0.166]
3. Sodah, Amer; Palevicius, Arvydas; Janusas, Giedrius; Palevicius, Paulius; Patel, Yatinkumar. Numerical and experimental investigation of sonotrode for formation of piezocomposite functional elements // Mechanika. Kaunas: KTU. ISSN 1392-1207. eISSN 2029-6983. 2019, vol. 25, iss. 6, p. 463-472. DOI: 10.5755/j01.mech.25.6.24793. [Science Citation Index Expanded (Web of Science); Scopus; Academic Search Complete] [IF: 0.500; AIF: 2.950; IF/AIF: 0.169; Q4 (2018, InCites JCR SCIE)] [CiteScore: 0.53; SNIP: 0.419; SJR: 0.202; Q4 (2018, Scopus Sources)] [M.kr.: T 009] [Contribution: 0.200]

In conference proceedings

1. [P1d; US] Sodah, Amer; Palevicius, Arvydas; Janusas, Giedrius. Design and analysis of computer generated optical element for visual cryptographic system // 2019 IEEE XV international conference on the perspective technologies and methods in MEMS design (MEMSTECH), POlyana, May 22-26, 2019: proceedings. Piscataway, NJ: IEEE, 2019. ISBN 9781728140285. p. 28-31. [M.kr.: T009] [Contribution: 0.334]
2. [P1e; LT] Sodah, Amer; Palevicius, Arvydas; Janusas, Giedrius; Jurenas, Vytautas; Patel, Yatinkumar Rajeshbhai. Sonotrode for formation of piezocomposite functional elements // Mechanika 2018: proceedings of the 23rd international scientific conference, 18 May 2018, Kaunas University of Technology, Lithuania / Kaunas University of Technology, Lithuanian Academy of Science, IFTOMM National Committee of Lithuania, Baltic

Association of Mechanical Engineering. Kaunas: Kaunas University of Technology. ISSN 1822-2951. 2018, p. 150-153. [Code: T009] [Contribution: 0.200]

PUBLICATION OF RESULTS OF RESEARCH AT CONFERENCES

(Conference abstracts and articles in non-refereed conference proceedings)

1. [T1e; TR] Palevičius, Arvydas; Šakalys, Rokas; Janušas, Giedrius; Sodah, Amer. Investigation of diffractive optical element of biosensor for human health monitoring // International conference on advanced technology & sciences : 4th international conference, ICAT'Rome, Rome, Italy, November 23-25, 2016 : abstracts / editors: Ismail Saritas, ... [*et al*.]. Konya : Aybil, 2016. eISBN 9786059119771. p. 64. [Code: T009]

APPENDIXES

- PHOTOS OF COMPUTER-GENERATED HOLOGRAM

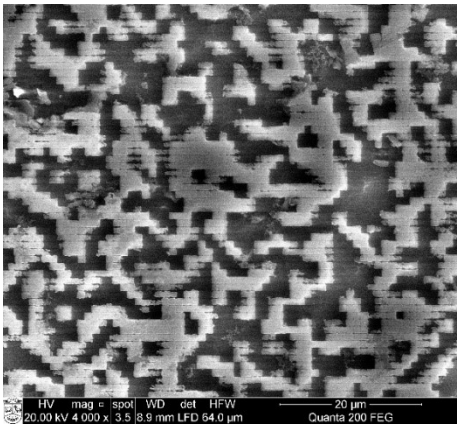

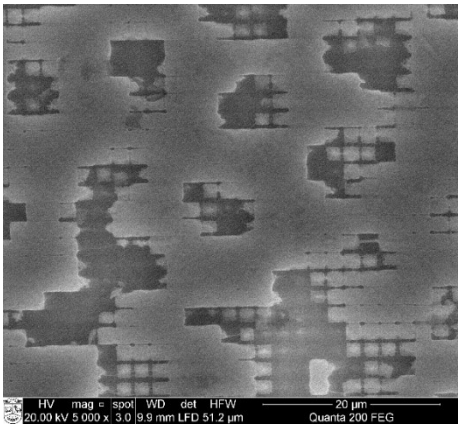

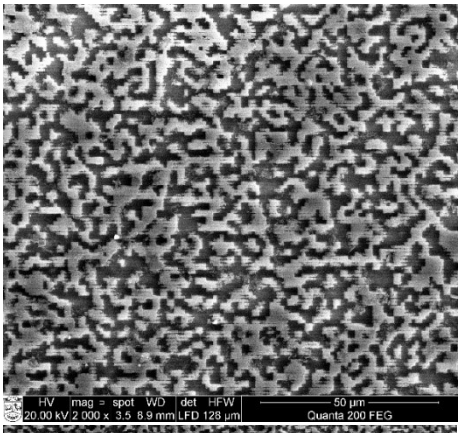

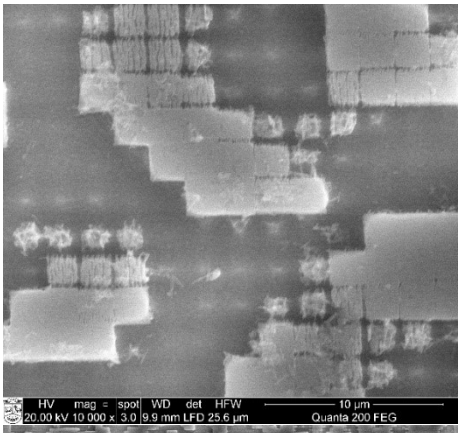

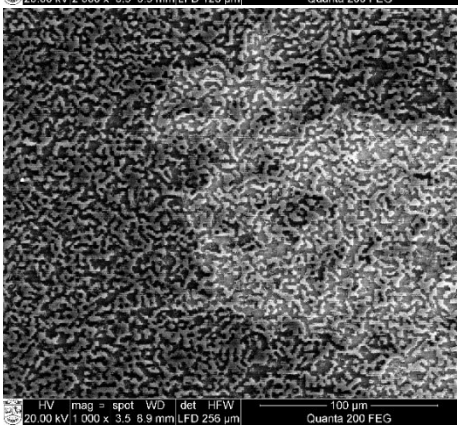

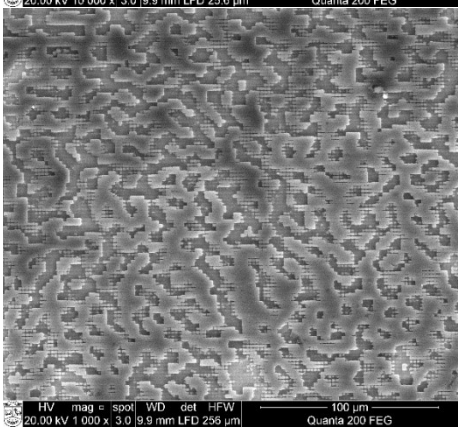

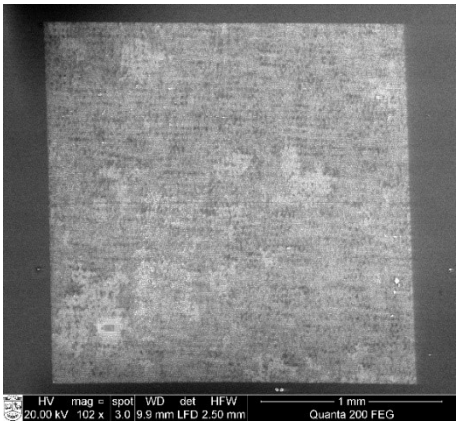

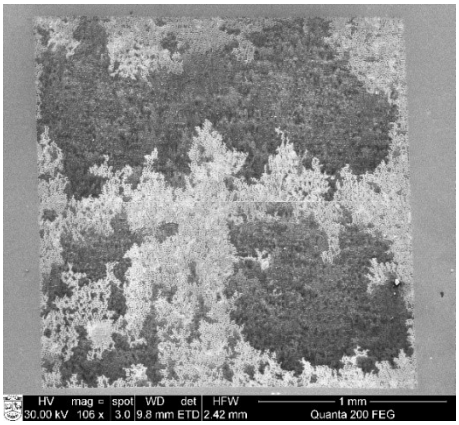

- PHOTOS OF EXPERIMENTAL SPECIMENS WITH REPLICAS

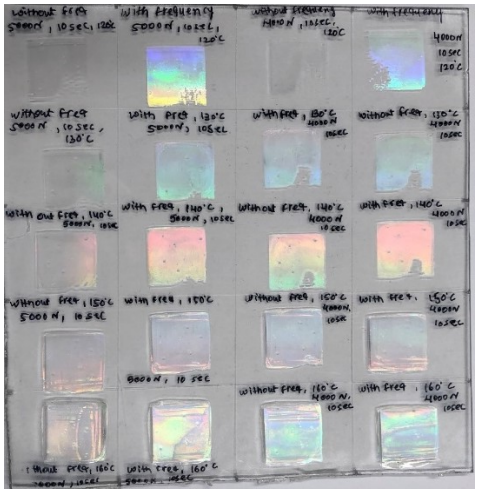

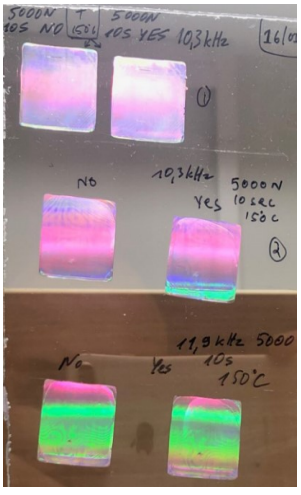

- PHOTOS OF REPLICAS FROM OPTICAL MICROSCOPE

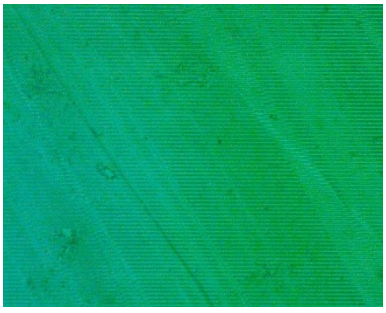

a

b

Photos of replicas (T=150 ºC, P=5000 N and time 10 sec) without excitation (a) and with vibration excitation (b) at frequency 11.9 kHz

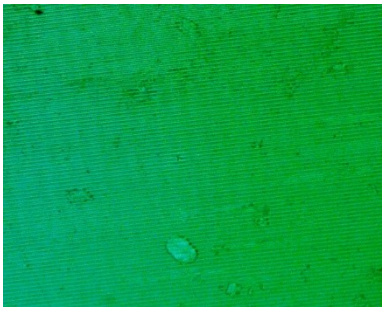

a

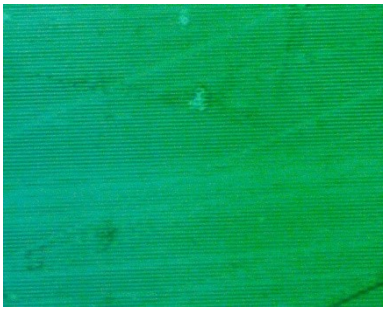

b

Photos of replicas (T=150 ºC, P=5000 N and time 2 sec) without excitation (a) and with vibration excitation (b) at frequency 11.9 kHz

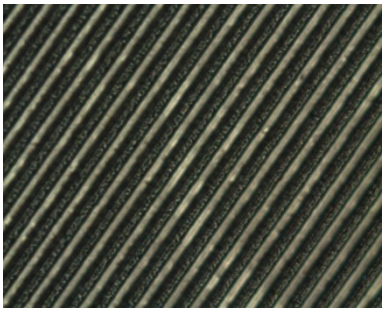

a

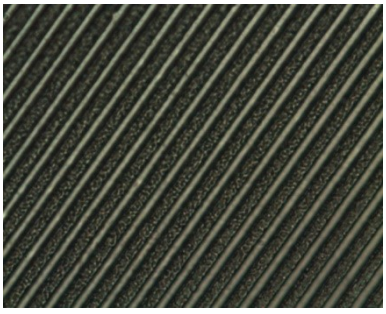

b

Photos of replicas (T=150 ºC, P=5000 N and time 10 sec) without excitation (a) and with vibration excitation (b) at frequency 10.3 kHz

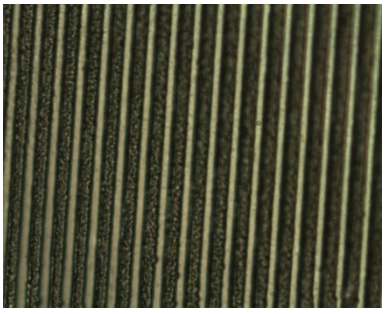

a

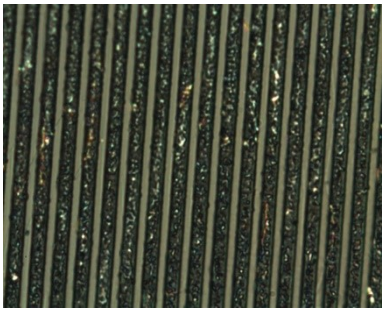

b

Photos of replicas (T=125 ºC, P=5000 N and time 10 sec) without excitation (a) and with vibration excitation (b) at frequency 10.3 kHz

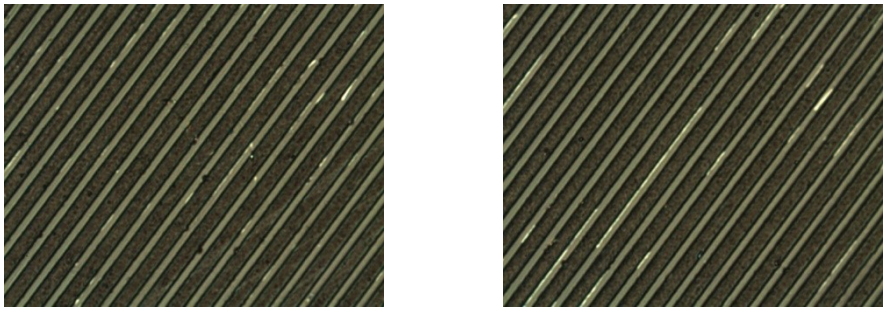

a **b**

Photos of replicas (T=100 ºC, P=4000 N and time 10 sec) without excitation (a) and with vibration excitation (b) at frequency 10.3 kHz

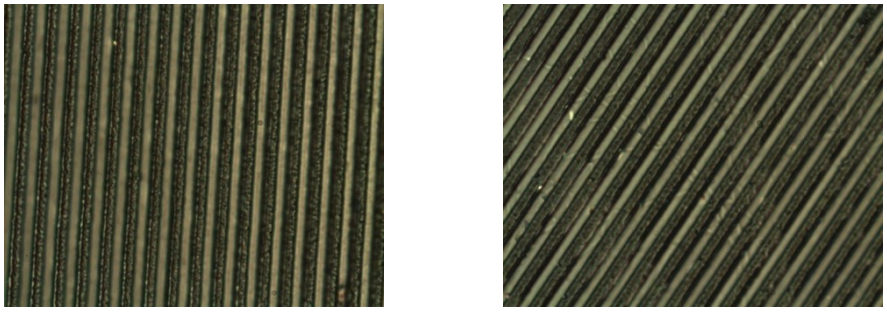

a **b**

Photos of replicas (T=100 ºC, P=3000 N and time 5 sec) without excitation (a) and with vibration excitation (b) at frequency 10.3 kHz

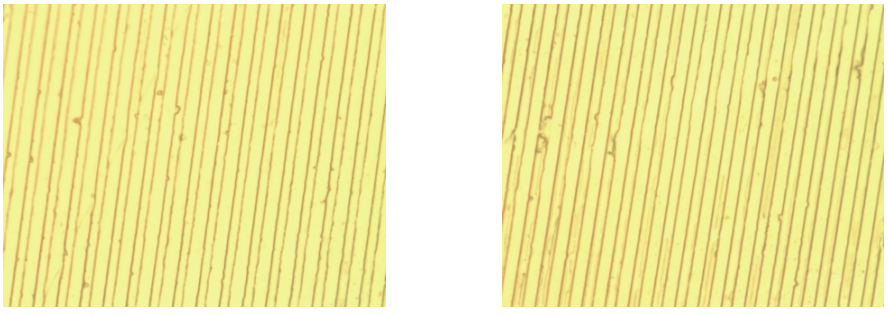

a **b**

Photos of replicas (T=125 ºC, P=3000 N and time 5 sec) without excitation (a) and with vibration excitation (b) at frequency 10.3 kHz

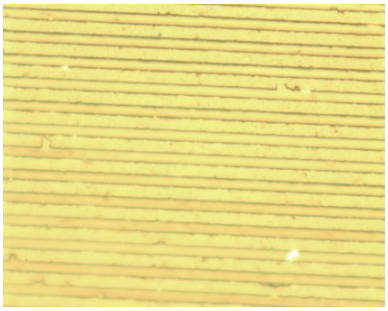

a

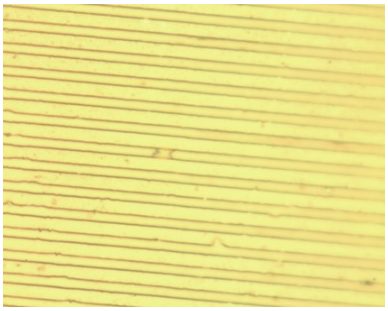

b

Photos of replicas (T=125 ºC, P=3000 N and time 5 sec) without excitation (a) and with vibration excitation (b) at frequency 10.3 kHz

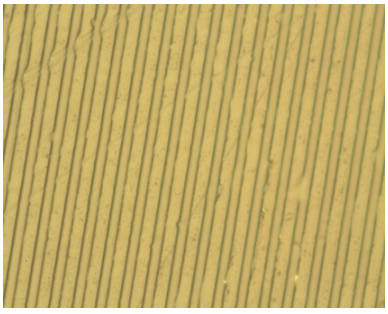

a

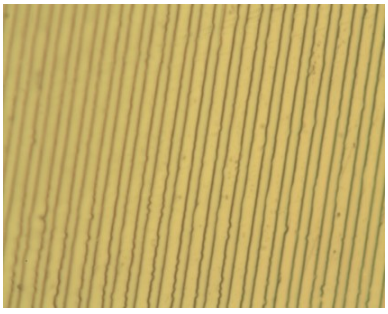

b

Photos of replicas (T=100 ºC, P=3000 N and time 10 sec) without excitation (a) and with vibration excitation (b) at frequency 10.3 kHz

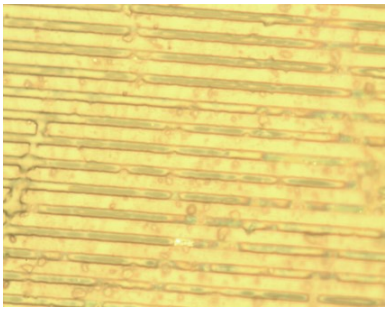

a

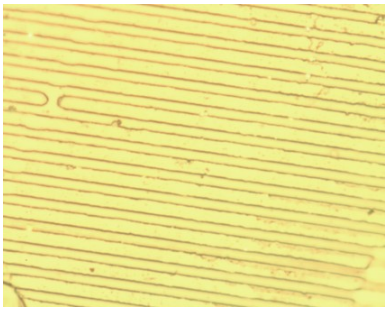

b

Photos of replicas (T=100 ºC, P=2000 N and time 10 sec) without excitation (a) and with vibration excitation (b) at frequency 10.3 kHz

UDK 678.02+534.232+004.932](043.3)

SL344. 2017-*-*, * leidyb. apsk. l. Tiražas * egz.
Išleido Kauno technologijos universitetas, K. Donelaičio g. 73, 44249 Kaunas
Spausdino leidyklos „Technologija“ spaustuvė, Studentų g. 54, 51424 Kaunas